Neutrino emission from Active Galaxies in the context of the measured diffuse astrophysical neutrino signal

Dissertation

zur Erlangung des Grades eines
Doktors der Naturwissenschaften
in der Fakultät für Physik und Astronomie
der Ruhr-Universität Bochum

vorgelegt von

Isaak Modaser Saba

geboren in
Kabul

Bochum, Mai 2015

1. Gutachter:	Prof. Dr. Julia Becker Tjus
2. Gutachter:	Prof. Dr. Wolfgang Rhode
mündlichen Prüfung:	17.06.2015

"Erst wenn der Verstand König und das Herz Priester ist, wird diese Welt gesunden."

Khalil Gibran

Acknowledgements

Die hier vorliegende Arbeit stellt eine Zusammenfassung meiner dreijährigen Promotionszeit an der Ruhr-Universität dar. Ohne die, sowohl wissenschaftliche, als auch private Unterstüztung vieler Menschen wäre die Arbeit in ihrer jetztigen Form nicht fertig geworden.
Ich möchte mich bei Prof. Dr. Julia Becker Tjus für Ihre Unterstüztung und die vielen Reisemöglichkeiten, die Sie mir gegeben hat, um meinen wissenschaftlichen Horizont zu erweitern bedanken. Vielen Dank für die tolle und konstruktive Zeit, angefangen mit dem Bachelor bis zum Doktor.
Weiterhin möchte ich mich bei Prof. Dr. Wolfgang Rhode dafür bedanken, dass er sich bereit erklärt hat meine Arbeit als Zweitgutachter zu lesen.
Ich möchte mich auch bei Prof. Dr. Reinhard Schlickeiser dafür bedanken, dass ich stets mit meinen mathematischen Problemen eine kompetente Ansprechperson hatte.
Ich bedanke mich bei all den Lehrstuhlmitarbeitern, besonders bei Anja Krause, die manchmal viele Mühe mit mir hatte :).
Eine gute Arbeit kann nur erfolgreich fertig gestellt werden, wenn auch das private Umfeld immer unterstützend zur Seite steht. Daher möchte ich mich ganz besonders bei meiner Familie bedanken, bei meiner Mutter Mahlia und bei meinem Vater Sayed Norullhaq, die mich wirklich in jeder Sekunde aus tiefsten Herzen unterstüzt haben. Ohne Sie wäre diese Arbeit überhaupt nicht möglich.
Meinen beiden (manchmal nervigen, aber im Grunde sehr guten Jungs :)) Brüdern, Mobascher und Mowahed danke ich für ihre konstruktive Kritik, und dafür, dass sie wirklich immer für mich da waren und da sind.
Meiner lieben Schwester Leyli danke ich für ihre Art und Weise und für die sehr große Unterstüztung.
Meinen engen Freunden Roshan und Amani danke ich für die sehr schöne und lustige Zeit, die wir gemeinsam hatten und weiter haben werden.
Die Abwechslung neben der Arbeit tat sehr gut.
Obwohl ich meine beiden Bürokumpanen, Mike und Fabian, erst im letzten Jahr kennenlernen durfte, haben wir sehr viel lustiges miteinander erlebt. Danke für das letzte wunderbare Jahr.
Natürlich gibt es noch sehr viele Menschen, die mich während dieser Zeit unterstüzt und geprägt haben. All diesen Menschen danke ich für die tolle Zeit.

Contents

List of Figures

List of Tables

Dedicated To my parents
Mahlia & Sayed Norullhaq, and to my niece Acila

Chapter 1

Introduction

It took thousands of years and the work of many pioneers, to gain the knowledge we have about the Universe today.
Until recently, compared to the age of a human being, mankind looked into the starry sky without knowing the processes going on. The ancient Babylonians started to observe the sky and noticed that some stars form constellations, which again can be used for navigation. Excited by curiosity, further observations showed that not all the stars are fixed. Some star-like objects move along the sky. These movements are not random but rather follow predictable patterns. These were first observations of planets. Egyptians used observations to predict the flooding of the nil. Thus, they were the first ones who used astronomical observations to improve social life.
Observations by Greeks indicated that Earth is not a disk but a sphere. Therefore, they used observations of the lunar eclipse and observed that the Earth shadow is round, and consequently the Earth must be a sphere. Eratosthenes calculated with simple geometrical assumptions the radius of the Earth, to be 6645 km, which deviates only 4% from current value 6370 km.
During the darks ages further observations helped to find more information about the Universe. Detailed observations by Tycho Brahe about the movements of planets were used by Johannes Kepler to show that planets move on elliptical orbits. Galileo Galilei, Kopernikus and Kepler negated the idea that Earth is the center of the Universe and showed that the Earth is a planet orbiting the Sun. More sophisticated instruments like telescopes were used. Messier published 1784 a catalogue with 103 *foggy* objects. These were the first detailed observations of galaxies. Herschel discovered Uranus in 1781 and Fraunhofer 1884 dark lines in

the solar spectrum. Later it was noticed that these lines are absorption lines of elements like sodium and helium.
Bessel, Struve and Henderson calculated distances to close stars by using the method of parallax. In 1913 Hertzsprung and Russell showed that the luminosity and spectral type of stars are correlated.
The detection of the neutrino, first postulated by Pauli to guarantee energy and momentum conservation in $\beta-$decay opened a new window in astrophysics. Neutrinos are produced in hadronic interactions and leave their point of origin without any considerable interaction with matter or radiation, to their way to Earth. The detection of solar neutrinos was the first clear proof for nuclear fusion as the energy source for stars.
Hubble showed that the Universe is expanding, while Jansky showed few years later 1932 that a strong radio source is located in the center of the Milky Way. Now, we know that this radio source is a massive black hole. Ewen, Purcell and Westerhout detected the 21 cm spectral line of neutral hydrogen. This method can be used to observe large amount of hydrogen in our and other galaxies.
The discovery of the cosmic microwave background by Penzias and Wilson was the first hint for the big bang theory.
More detailed observations and more sophisticated instruments rise more questions, which have to be answered: What is dark matter? What is dark energy? Is the Universe going to collapse? Which astrophysical sources can accelerate cosmic rays to the highest energies, and where do the recent IceCube detected high-energy neutrinos originate from?

The goal of this work is to calculate neutrino fluxes and column densities for active galactic nuclei and to compare with recent IceCube observations of high-energy neutrinos. This thesis is structured in the following manner:
For a better understanding of the calculation the reader is introduced step by step in the subject matter. Chapter 2 gives a brief introduction into the physics of Cosmic Rays (CRs), their possible origin and how they are accelerated to the observed energies. Chapter 2 ends with current IceCube observations, which are used in this work to calculate neutrino fluxes and column densities.
Chapter 3 deals with AGN in general. Since the calculations base on radio luminosities section 3.4 and section 3.7 give a brief introduction into synchrotron radiation of high energy electrons and radio luminosity function of FR-I, FR-II and Blazars.

To fix the proton spectrum, the transport equation is solved in chapter 4. Therefore, energy loss processes, see section 4.1 and energy gain processes, see section 4.2 have to be considered.

After having introduced into the physics of AGN and into the transport equation, chapter 5 deals with analytical and semi analytical methods to calculate fluxes and column densities for radio galaxies and Blazars. The electron-to-proton ratio g_e and electron luminosity L_{e} to radio luminosity L_{radio} ratio $\chi(s, B)$ will be fixed by measurable quantities, see section 5.1.1 and section 5.1.2. In section 5.2 semi analytical and full analytical results will be compared and constraints for the considered AGN groups will be given.

Chapter 6 deals with Fermi *LAT* observations of seven close radio galaxies, with Centaurus A (Cen A) and Messier 87 (M 87) of special interest.
Assuming that $\gamma-$rays are produced through the decay of neutral pions, $\gamma-$ray and neutrino flux are linked. Thus, computed column densities will be used to fix neutrino fluxes. These fluxes are compared with sensitivities of current neutrino telescopes, IceCube and Antares and with the sensitivity of the future telescope KM3NeT.
Chapter 7 gives the Conclusion and Outlook.

Einleitung

Es benötigte Jahrtausende sowie die Arbeit von vielen Pionieren, um das Wissen über das Universum zu sammeln, das wir heute haben.
Noch vor im Vergleich zum Alter der Menschheit kurzer Zeit blickte der Mensch in den Sternenhimmel, ohne sich über die physikalischen Vorgänge im Klaren zu sein. So waren es die Babylonier, die um 3000 vor Christus Sterne zu Konstellationen zusammenfügten und dem Himmel so erste Strukturen gaben. Die Idee der Sternbilder und Tierkreiszeichen wurde geboren. Angeregt von diesen Beobachtungen und durch die Neugierde führten weitere Beobachtungen zur Feststellung, dass einige Objekte am Himmel nicht statisch sind, sondern sich bewegen. Die Bewegung dieser Objekte erfolgte nicht zufällig, sondern nach bestimmten Mustern. So kam es, dass die ersten Planeten beobachtet wurden. Erste systematische Himmelsbeobachtungen wurden durch die Ägypter durchgeführt, die nicht nur den Bau der Pyramiden an bestimmten Sternenkonstellationen ausrichteten, sondern auch die Nilüberflutungen vorhersagen und somit Vorgänge in der Natur teilweise exzellent beschreiben konnten. Weiterhin führten sie das Sonnenjahr mit der 365-Tage-Periode ein.
Durch die Griechen kamen dann die ersten Rückschlüsse auf die Gestalt der Erde. So konnten durch Beobachtungen des Erdschattens bei Mondfinsternissen darauf zurückgeschlossen werden, dass die Erde eine Kugelgestalt haben muss. Eratosthenes konnte mit Hilfe einfacher geometrischer Überlegungen den Erdradius auf 6645 km (heute 6371 km) berechnen, was einer Abweichung von ca. 4% zum heutigen Wert entspricht.
Im Mittelalter konnten die Erkenntnisse über den Aufbau des Universums unter anderem durch Tycho Brahe, der detaillierte Beobachtungen der Planetenbewegungen anfertigte, weiter vertieft werden. Diese Beobachtungen wurden widerrum vom jungen Johannes Kepler verwendet, der unter Anwendung mathematischer Modelle zeigen konnte, dass sich die Planeten auf Ellipsenbahnen um die Sonne bewegen.
Es waren Galileo Galilei und Johannes Kepler, die die Idee der Erde als Zentrum des Universums negierten und ihr die Rolle gaben, die sie wirklich erfüllte, ein Planet von vielen, der die Sonne auf einer Ellipsenbahn umkreist.
Nachdem Kepler als Erster die Mathematik als Werkzeug in der Astronomie etablierte und somit als der Gründer der modernen Astrophysik gelten darf, ging Isaac Newton einen Schritt weiter, indem er Keplers Beobachtungen auf beliebige Körper

verallgemeinern konnte. Das Gravitationsgesetz war geboren.
Ausgerüstet mit neuen Beobachtungsmethoden wie moderne Teleskope, sowie mit einem sich rasant entwickelnden mathematischen Rüstzeug erfolgten neue Entdeckungen. Messier veröffentlichte 1784 einen Katalog mit 103 *nebligen* Objekten. Dabei handelt es sich um Galaxien, wie wir mittlerweile wissen. Herschel entdeckt 1781 den Uranus und Fraunhofer beobachtet 1814 dunkle Linien im Sonnenspektrum. Dabei handelt es sich um charakteristische Absorptionslinien von Elementen wie Natrium oder Helium. Bessel, Struve und Henderson gelang es im Jahre 1838 mittels Parallaxen, die Entfernungen der näheren Fixsterne zu messen. Hertzsprung und Russell zeigten 1913, dass die Leuchtkraft und der Spektraltyp eines Sterns miteinander korellieren.
Durch die Entdeckung des postulierten Neutrinos, das zur Rettung der Energieerhaltung beim $\beta-$Zerfall diente, eröffnete sich ein neues Fenster in der Astrophysik. Durch ihre Ladungsneutralität und der extrem geringen Wirkungsquerschnitte sind Neutrinos hervorragende Botenteilchen, die Informationen aus weitentfernten Quellen liefern können. Während die kosmische Strahlung durch Magnetfelder abgelenkt wird oder mit der Hintergrundstrahlung wechselwirkt und Gammastrahlung auch auf ihrem Weg zur Erde Wechselwirkungen mit Materie und Strahlung erleidet, können Neutrinos nahezu ohne nennenswerte Wechselwirkungen zu uns gelangen und wichtige Informationen über die Quellen liefern.
Im letzten Jahrhundert konnten durch detaillierte Beobachtungen neue Erkenntnisse gewonnen werden. Hubble konnte zeigen, dass sich das Universum ausdehnt. Ein Maß für die Expansionsgeschwindigkeit gibt die Hubble-Konstante H_0 Unmittelbar danach, im Jahr 1932, konnte Jansky zeigen, dass sich im Zentrum unserer Milchstraße eine Radioquelle befindet, von der wir heute mit Sicherheit ausgehen, dass es sich um ein massives schwarzes Loch handelt. Ewen, Purcell und Westerhout gelang durch die Beobachtung der 21cm-Spektrallinie des neutralen Wasserstoffs eine Möglichkeit, um Wasserstoffwolken in Galaxien zu entdecken. Die Entdeckung der kosmischen Hintergrundstrahlung durch Penzias und Wilson gilt als erster Beleg für die Urknalltheorie.
Durch die immer weiter verfeinerteren Beobachtungen können mehr Fragen beantwortet werden. Allerdings kommen ständig neue Fragen hinzu, sodass die Astrophysik vor neuen herausfordernden Fragestellungen steht:
Was genau ist die dunkle Materie? Was genau ist die dunkle Energie? Wie entwickelt sich unsere Galaxie? Wird sie am Ende ihrer Existenz kollabieren? Welche astrophysikalischen Quellen sind für die Beschleunigung der kosmischen Strahlung

verantwortlich?

Das Ziel der Arbeit ist es, unter Annahme geringer optischer Tiefen Neutrinoflüsse und Säulendichten für aktive Galaxien zu berechnen. Es wird angenommen, dass hochenergetische Teilchen ($E \geq 10^{18}\,\mathrm{eV}$) unter anderem in aktiven Galaxien produziert werden. Protonen, die beschleunigt werden, können unter anderem mit Photonen oder mit anderen Protonen wechselwirken. Wir konzentrieren uns auf die inelastische Proton-Proton-Wechselwirkung. In diesen Wechselwirkungen werden unter anderem geladene Pionen produziert, die anschließend in Neutrinos zerfallen. Diese Neutrinos können aufgrund ihrer Ladungsneutralität und der geringen Wechselwirkungsquerschnitte ihren Entstehungsort verlassen, um auf der Erde detektiert zu werden.
Hierfür werden IceCube-Messungen hochenergetischer Neutrinos verwendet. Anschließend werden Einschränkungen für die Produktionsorte innerhalb von aktiven Galaxien. Der Fokus liegt auf Fanaroff-Riley I, II und Blazare.
Die Arbeit ist wie folgt aufgebaut: Der Leser wird in Kapitel 2 in die Physik der kosmischen Strahlung eingeführt. Es wird erklärt, welche galaktischen bzw. extragalaktischen Quellen für die Erzeugung energetischer bzw. hochenergetischer Teilchen in Fragen kommen. In Abschnitt 2.4 wird verdeutlicht, wieso Neutrinos geeignete Kandidaten sind, um wichtige Informationen über die Beschleunigung hochenergetischer Teilchen, aber auch über den Entstehungsort dieser Teilchen zu liefern. In Abschnitt 2.5.2 wird die Beobachtung hochenergetischer Neutrinos mit dem IceCube-Detektor erläutert. Diese Beobachtungen werden verwendet, um in dieser Arbeit Neutrinoflüsse und Säulendichten zu berechnen.

Kapitel 3 gibt eine Einführung in die Physik der AGN mit besonderem Augenmerk auf Synchrotronstrahlung (Abschnitt 3.4) und hier verwendeten Radioleuchtkraftfunktionen für FR-I, FR-II und für Blazare (Abschnitt 3.7).

Um Neutrinoflüsse berechnen zu können, wird das Protonenspektrum benötigt. In Kapitel 4 wird unter Berücksichtigung von Energieverlusten (Abschnitt 4.1) und Beschleunigung (Abschnitt 4.2) die Transportgleichung gelöst.

In Kapitel 5 werden Neutrinoflüsse und Säulendichten sowohl analytisch als auch semianalytisch berechnet und miteinander verglichen. Durch Hinzunahme von

Beobachtungen und anderen theoretischen Überlegungen können für FR-I-und FR-II Galaxien Einschränkungen für die Entstehungsorte der Neutrinos innerhalb des Jets gegeben. Für Blazare können Einschränkungen für Boostfaktoren Γ_{B} und Inklinationswinkeln i gegegeben werden.

In Kapitel 6 werden unter Zuhilfenahme von Fermi-*LAT* Daten für sieben nahe FR-I Galaxien die Säulendichten und Neutrinoflüsse berechnet. Die errechneten Flüsse werden anschließend mit den Sensitivitäten von IceCube, Antares sowie KM3NeT verglichen, um Informationen darüber zu erhalten, ob die potentielle Galaxien Neutrinoquellen sind.

Die Arbeit schließt mit Kapitel 7, *Conclusion & Outlook*. Hier werden alle Ergbenisse zusammengefasst und diskutiert.

Chapter 2

Cosmic rays

Shortly after the discovery of radioactivity by Antoine Henri Bequerel, it was noticed that charged particles were produced in a cubic centimeter of air every second [1]. To answer the question of whether these ionized particles are generated by the surface of the Earth or whether they originate from the space, Victor Hess and Werner Kohlhörster started measuring ionization profiles within the atmosphere in balloons, and showed: With increasing altitude, ionization also increases, which can be explained by the assumption that high-energy particles or radiation enters the atmosphere. Even in its lower layers, these particles ionize neutral atoms within the atmosphere. Since there is no decrease at night or during a solar eclipse, the Sun can be ruled out. In 1929 Clay observed a "latitude effect", meaning that the cosmic ray intensity depends on the geomagnetic latitude [2]. Bothe and Kohlhörster found the correct interpretation, as an anisotropy induced by the Earth's magnetic field. Consequently, cosmic rays must be charged particles. The term *cosmic ray* (hereafter CR) was proposed by Milikan and Compton who favored gamma rays to be the source of the ionization. However, the "latitude effect" and experiments in cloud chambers proved that CRs are charged particles that reach Earth from outer space.

These are mainly protons, helium and some heavier nuclei. Electrons and antimatter are also constituents but are outnumbered, in comparison to the main components.

The CR-flux can be approximated by an broken power-law function with in the

following characteristic features[3]:

$$\frac{\mathrm{d}N_{\mathrm{CR}}}{\mathrm{d}E_{\mathrm{CR}}} \propto E^{-\alpha_{\mathrm{CR}}} \tag{2.1}$$

$$\alpha_{CR} = \begin{cases} 2.67 & \text{for } \log(E_{\mathrm{CR}}/\mathrm{eV}) < 15.4 \\ 3.10 & \text{for } 15.4 < \log(E_{\mathrm{CR}}/\mathrm{eV}) < 18.4 \\ 2.75 & \text{for } 18.5 < \log(E_{\mathrm{CR}}/\mathrm{eV}). \end{cases} \tag{2.2}$$

It is generally accepted that for energies below the knee ($E_{\mathrm{CR}} \leq 10^{15}$ eV) CRs originate from the Milky Way, with supernova remnants as main candidates. However, it should be noted that this picture is built on phenomenological arguments with no full experimental proof yet. The origin of the knee ($E_{\mathrm{CR}} \approx 10^{15}\,\mathrm{eV}$) is still under debate [4], [5], [6].

Low energy CRs are deflected by the solar magnetic field. If CR particles enter the solar system, they must overcome the solar wind to reach Earth. The winds slow down particles and prevent the lowest energetic ones from reaching the Earth [2]. This effect is called solar modulation and is anti-correlated with the level of solar activity. If the solar activity is high, and, thus, the magnetic field is high, the CR flux is low, and vice versa.

CRs beyond the knee and ankle ($E_{\mathrm{CR}} \geq 10^{18}$ eV) are mainly believed to be extragalactic. They are believed to be produced and accelerated in active galactic nuclei, Gamma-ray Bursts or other sources as yet unknown. Extreme high energies ($E \geq 10^{19}\,\mathrm{eV}$) CRs will lose energy due to interactions with intergalactic radiation fields. Greisen, Zatsepin and Kuz'min predicted a cut-off in the CR-flux at around $6 \cdot 10^{19}$ eV due to photo-pion production on the microwave background [7]. If a high-energy CR proton interacts with a microwave background photon the following particles can be created

$$p + \gamma_{\mathrm{CMB}} \rightarrow n + \pi^{+} \tag{2.3}$$

$$\rightarrow p + \pi^{0} \tag{2.4}$$

$$\rightarrow p + e^{+} + e^{-}. \tag{2.5}$$

However, pair production is less significant than photo-pion production. Protons with energies ($E \geq 10^{19.6}\,\mathrm{eV}$) originate from sources with a distance of approximately 6 Mpc. Consequently, the GZK cutoff gives a constraint on the distance of objects, being sources of CRs with energies $E \geq 10^{19}$ eV.

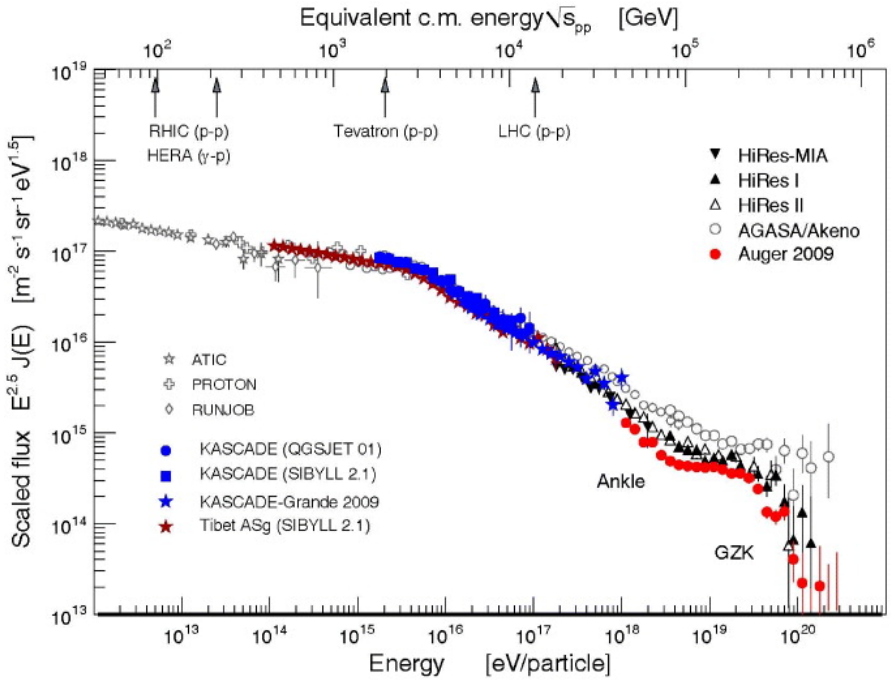

FIGURE 2.1: Cosmic ray flux. To emphasize the spectral shape the function is multiplied by $E^{2.5}$ [8].

2.1 Hillas criterion

The question of how and in which environments particles are accelerated to energies much higher than man made accelerators like the LHC has been much discussed since the first observations of CRs. Many theories have been proposed and verified by experiments.

One of the prominent and most accepted theories is proposed by Hillas, who gives constraints on astrophysical sources to be the origin of energetic CRs [9]. According to this theory, accelerated particles should be confined inside the acceleration region, while they are accelerated. The Larmor radius R_{L} may not exceed the acceleration size $R_{\mathrm{acc.}}$. Furthermore, the accelerator should possess sufficient energy to transfer it to the accelerated particles. Energy loss processes due to radiation and interactions with photons and particles should not exceed energy gain processes.

Considering these constraints, the Hillas argumentation gives a simplified condition for sources to accelerate particles to the observed energies (Figure 2.2). Thus, the Larmor radius $R_{\mathrm{L}} = E/(Z\,e\,B)$ must be smaller than the size of the acceleration region, $R_{\mathrm{acc.}}$, which gives a strong constraints on the maximum particle

energy [10]:

$$E_{\max} = \beta_{\mathrm{s}} \cdot Z \cdot B \cdot R_{\mathrm{acc.}}, \tag{2.6}$$

with $\beta_{\mathrm{s}} = \frac{V_{\mathrm{s}}}{c}$ giving the velocity of the shock region in which particles are accelerated, and Z the charge of the particle in units of e. Sources above the blue line can accelerate protons to energies $E > 10^{20}$ eV and sources above the red line can accelerate iron nuclei to energies $E > 10^{20}$ eV.
Equation (2.6) gives a first condition that sources must fulfill in order to accelerate particles to the observed energies. More strict limitations can be found by considering energy loss effects. Thus, the maximum particle energy is fixed by

$$\frac{\mathrm{d}E^{\max}}{\mathrm{d}t} = -\frac{\mathrm{d}E^{\mathrm{loss}}}{\mathrm{d}t}. \tag{2.7}$$

Energy loss due to radiation for a charged particle, moving with mass m and velocity v in an arbitrary electric $\vec{E}$ and magnetic field $\vec{B}$ is given by

$$-\frac{\mathrm{d}E^{\mathrm{loss}}}{\mathrm{d}t} \propto F_{\perp} + \left(1 - \frac{v^2}{c^2}\right) F_{||}, \tag{2.8}$$

where $F_{\perp}$ gives the perpendicular component of the force with respect to v, which acts on the particle and $F_{||}$ the parallel component [11]. The first term in equation (2.8) considers loss processes due to synchrotron radiation and the second term considers curvature radiation, which is suppressed with respect to the first term by the factor $(1 - \frac{v^2}{c^2})$. For ultra relativistic particles ($v \approx c$) the second term vanishes and only the first term contributes to energy loss.
Depending on the magnetic field configuration either synchrotron or curvature radiation dominates. For inhomogeneous magnetic fields synchrotron radiation loss dominates. Thus the energy loss is given by

$$-\frac{\mathrm{d}E^{\mathrm{loss}}}{\mathrm{d}t} = \frac{2}{3}\left(\frac{Z \cdot e}{A\, mc^2}\right)^4 c\, E^2\, B^2. \tag{2.9}$$

Here, A gives the atomic mass number. For ordered magnetic fields within the acceleration regime, the first term vanishes and curvature radiation is the main process:

$$-\frac{\mathrm{d}E^{\mathrm{loss}}}{\mathrm{d}t} = \frac{2}{3}\left(\frac{Z \cdot e\sqrt{c}}{R_{\mathrm{acc.}}}\right)^2 \left(\frac{E}{A\, mc^2}\right)^4 \tag{2.10}$$

Thus, considering Equation (2.7) the maximum energy is given by [11]

$$E_{\max} = \begin{cases} 1.64 \cdot 10^{20}\,\mathrm{eV}\,\frac{A^2}{Z^{3/2}}\left(\frac{B}{\mathrm{Gauss}}\right)^{-1/2} & \text{for synchrotron radiation} \\ 1.23 \cdot 10^{22}\,\mathrm{eV}\,\frac{A}{Z^{1/4}}\left(\frac{R_{\mathrm{acc.}}}{\mathrm{kpc}}\right)^{1/2} & \text{for curvature radiation.} \end{cases} \tag{2.11}$$

Protons can be accelerated in regions with ordered magnetic fields to higher energies, compared to protons which are accelerated in environments with inhomogeneous magnetic fields.

However, pure ordered magnetic fields are very unlikely on large scales because in sources like Gamma Ray Bursts or active galactic nuclei particles are influenced by interactions or other mechanisms, leading to a large contribution from inhomogeneous magnetic fields.

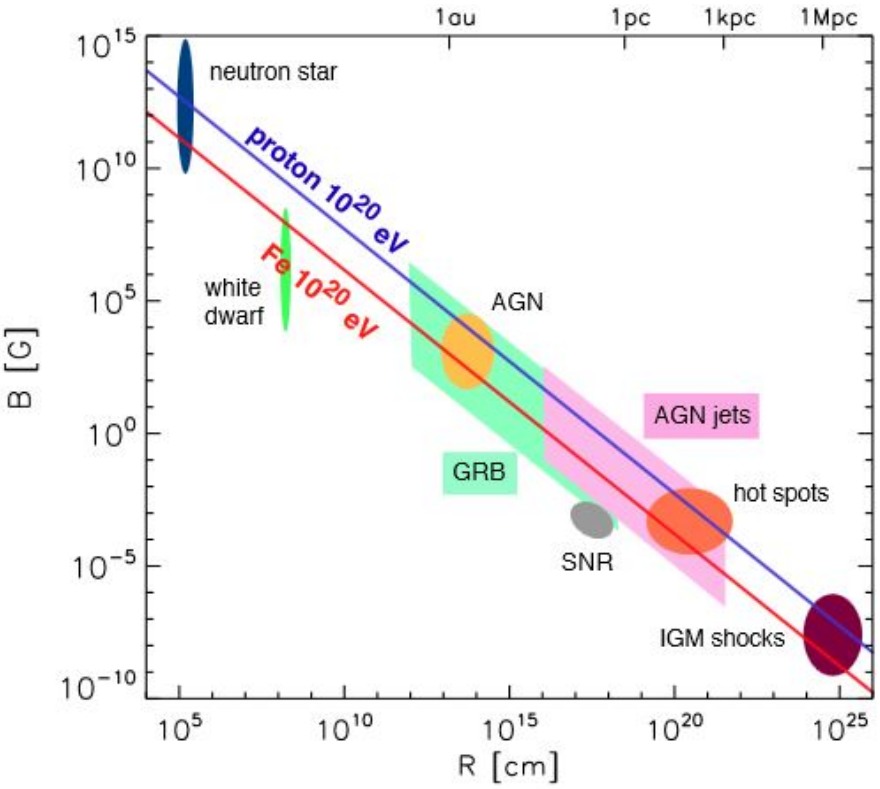

FIGURE 2.2: The Hillas plot. Above the red line sources can accelerate iron nuclei up to 10^{20} eV. Above the blue line sources can accelerate protons to 10^{20} eV [12].

2.2 Fermi II and Fermi I mechanisms

The question of how particles are accelerated is explained in this section. Two commonly accepted mechanisms are Fermi I and Fermi II. The first section deals with Fermi II, and section 2.2.1 with Fermi I. Consider a particle with energy E_1 moving with velocity $\vec{v}$, encountering a magnetic cloud, which moves with a velocity $\vec{v}_{\text{cloud}}$. Within the cloud, the particle is scattered by magnetic irregularities, increasing its energy and leaving the cloud with energy E_2. The energy gain is given by $\kappa = (E_2 - E_1)/E_1$. In the cloud frame the particle penetrates the cloud with the energy[1]:

$$E_1' = \gamma E_1 \left(1 - \beta \cos(\vartheta_1)\right) \tag{2.12}$$

$$\beta = \frac{v_{\text{cloud}}}{c} \tag{2.13}$$

$$\gamma = \frac{1}{\sqrt{1-\beta^2}}. \tag{2.14}$$

After the particle is scattered and leaves the cloud the energy is:

$$E_2 = \gamma E_2' \left(1 + \beta \cos(\vartheta_2')\right) \tag{2.15}$$

$$= \gamma^2 E_1 \left(1 + \beta \cos(\vartheta_2')\right) \left(1 - \beta \cos(\vartheta_1)\right). \tag{2.16}$$

Due to isotropic scattering the exit direction is randomized, $\langle \cos(\vartheta_2') \rangle = 0$. In equation (2.13) $E_2' = E_1'$ is assumed, which is justified since particles are not suffering inelastic collisions. However the "penetration angle" ϑ_1 is proportional to the relative velocity of the particle and cloud. Thus, averaging $\langle \cos(\vartheta_1') \rangle$ gives $\langle \cos(\vartheta_1') \rangle = -\beta/3$, see [2]. Consequently, the energy gain is:

$$\langle \kappa \rangle = \frac{\langle E_2 \rangle - \langle E_1 \rangle}{\langle E_1 \rangle} \tag{2.17}$$

$$\gamma^2 \left(1 - \beta \underbrace{\langle \cos(\vartheta_1) \rangle}_{-\beta/3}\right) \left(1 + \beta \underbrace{\langle \cos(\vartheta_2') \rangle}_{0}\right) - 1 \tag{2.18}$$

$$\gamma^2 \left(1 + \frac{\beta^2}{3}\right) - 1 \tag{2.19}$$

$$\overset{\text{Taylor}}{=} 1 + \frac{7}{2}\beta^2 + O(\beta^4). \tag{2.20}$$

[1] The primed parameters gives the values in the cloud frame

Since $\beta = \frac{V_{\text{cloud}}}{c} \ll 1$, κ is relatively small. Consequently, the Fermi II mechanism (first non-vanishing value proportional to β^2) cannot explain observations of the highest energies. For this purpose the theory must be modified, which leads to the result that the increase of the energy depends on the first order of β.

2.2.1 Fermi I mechanism

Consider an infinitesimal thin and long shock wave, moving with velocity v_{shock}. A particle with energy E_1 encounters the wave and is scattered by magnetic irregularities behind the shock. Due to the preferential direction of the shock it is $\langle\cos(\vartheta_2)\rangle \neq 0$, [2]. After leaving the shock region, the energy is:

$$E_2 = \gamma E_2' \left(1 + \beta\cos(\vartheta_2')\right) \tag{2.21}$$

$$= \gamma^2 E_1 \left(1 + \beta\cos(\vartheta_2')\right)\left(1 - \beta\cos(\vartheta_1)\right) \tag{2.22}$$

$$\beta = \frac{v_{\text{shock}}}{c} \tag{2.23}$$

Averaging E_2 gives

$$\langle E_2\rangle = \gamma^2 E_1 \left(1 + \beta \underbrace{\langle\cos(\vartheta_2')\rangle}_{1/2}\right)\left(1 - \beta \underbrace{\langle\cos(\vartheta_1)\rangle}_{-1/2}\right). \tag{2.24}$$

Consequently, the averaged energy gain is:

$$\langle\kappa\rangle = \frac{\langle E_2\rangle - \langle E_1\rangle}{\langle E_1\rangle} \tag{2.25}$$

$$= \gamma^2\left(1 + \frac{\beta}{2}\right)^2 - 1 \tag{2.26}$$

$$\overset{\text{Taylor}}{\propto} \beta + O(\beta^2). \tag{2.27}$$

The increase in energy is linear in β (First order Fermi). To accelerate particles to high energies, the source must fulfill among others two conditions:

- Particles should be scattered many times. Thus the magnetic field within the shock region must be high to keep the particle inside.
- Large shock regions should exist, which allow the particle to penetrate the shock frontally.

These conditions can be found among others in supernova remnants within the Milky Way, where large shock regions in combination with high magnetic fields exist.

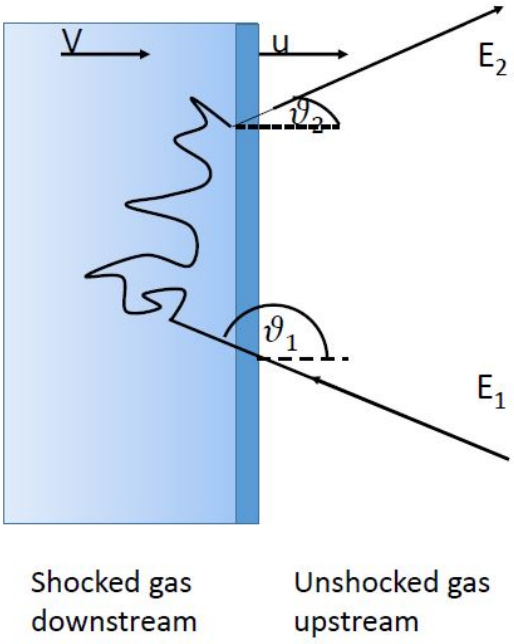

(A) Schematic illustration of Fermi I mechanism. A particle penetrates a shock wave with energy E_1 under ϑ_1. It is scattered at magnetic field irregularities increases its energy and leaves under ϑ_2 with energy E_2. Since the shock wave has a preferred direction it is $\langle\cos(\vartheta_2)\rangle \neq 0$.

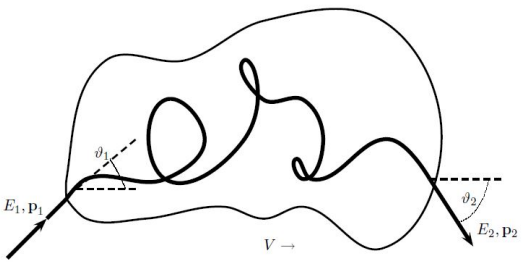

(B) Particles penetrates a cloud with E_1. Within the cloud it will be scattered and leaves the cloud with an higher energy E_2. Since clouds are randomly located and scattering of particles are isotopic it is $\langle\cos(\vartheta_2)\rangle = 0$.

FIGURE 2.3: Schematic illustration of Fermi I and Fermi II. In Fermi I processes the energy gain is proportional to β, while in Fermi II it is proportional to β^2. High energetic phenomena can be explained with Fermi I mechanism.

2.3 Galactic & extragalactic CR sources

CRs with energies up to the knee ($E_{\mathrm{CR}} \leq 10^{15}\,\mathrm{eV}$) are believed to originate from supernova remnants (SNRs) within our Galaxy. SNRs are leftovers of extremely energetic stellar explosions, which outshines their host galaxies. Most of the stellar

material is ejected and forms an approximately spherical shock wave, propagating through space. While propagating the shock collects matter and accelerates them via the Fermi I process to highest energies.

In the following calculations, a typical rate for supernovae in the Milky Way, $\mathrm{d}N/\mathrm{d}t \approx 3/100$ years and a shock activity for about $t_{\mathrm{shock}} \approx 1000$ years is assumed. Furthermore, results from [3] by assuming a luminosity for a single SNR of $L_{\mathrm{SNR}} \approx 10^{41}$ erg/s are adopted. With these conditions, the total SNR luminosity is given by

$$L_{\mathrm{SNR}}^{\mathrm{tot}} = \frac{\mathrm{d}N}{\mathrm{d}t} \cdot t_{\mathrm{shock}} \cdot L_{\mathrm{SNR}} \tag{2.28}$$

$$\approx 3 \cdot 10^{42}\,\mathrm{erg/s}. \tag{2.29}$$

Comparing this result with the CR luminosity for the range $10^9\,\mathrm{eV} \leq E_{\mathrm{CR}} \leq 10^{15}\,\mathrm{eV}$, [3]

$$L_{\mathrm{CR}} \approx 10^{41}\,\mathrm{erg/s} \tag{2.30}$$

indicates, that SNRs are efficient enough to accelerate particles up to $E_{\mathrm{CR}} \leq 10^{15}\,\mathrm{eV}$.

For higher energies two scenarios exist, trying to explain the origin of CRs with energies $E \geq 10^{18}\,\mathrm{eV}$. In the *top-down* model high-energy particles are created through the decay of super heavy particles with masses up to $m = 10^{24}\,\mathrm{eV}/c^2$. The decay of such heavy particles, leads to protons with energies up to $E_{\mathrm{CR}} \approx 10^{21}$ eV, which are accompanied by a large flux of high-energy $\gamma-$rays and neutrinos. In this model the GZK cut-off can be avoided, when protons are produced in the vicinity of the Earth [3]. However, the confirmation of the GZK cut-off and the absence of a neutrino and $\gamma-$ray signature disfavor this scenario.

In the *bottom-up* model high-energy CRs above the ankle are assumed to be produced in acceleration processes in extragalactic sources. To assess which extragalactic objects may be sources of CRs with energies $E_{\mathrm{p}} \geq 10^{18}$ eV the energy density rate of CRs above the ankle will be calculated and compared with the luminosity of Gamma Ray Bursts and active galactic nuclei.

The spectrum of the CR spectrum above the "ankle" (Figure 2.4) is approximated by [13]:

$$\phi_{\mathrm{p}} = \phi_0\, E_{\mathrm{p}}^{-s} \left[1 + \exp\left(\frac{\log(E_{\mathrm{p}}) - \log(E_{\mathrm{B}})}{\log(W)}\right)\right]^{-1}. \tag{2.31}$$

Here, E_B gives the energy, at which the flux has fallen to one half of the value of the power-law extrapolation, and W gives the width of the transition region.

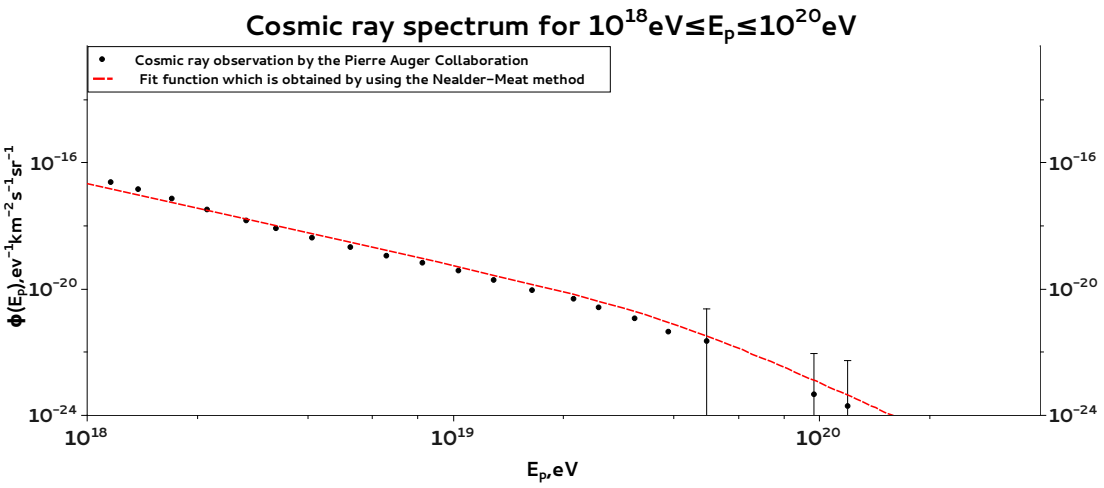

FIGURE 2.4: Cosmic ray spectrum for the high-energy regime. Data are taken from the Auger Collaboration [13]. The red (dashed) line gives the fit function obtained by using the Nealder-Meat method.

The energy density rate $\dot{\rho}_\mathrm{CR}$, which will be important in section 5.1.1, is given by

$$\dot{\rho}_\mathrm{CR} = \frac{H_0}{c}\left(\int_{10^{18}\mathrm{eV}}^{10^{20}\mathrm{eV}} \phi_\mathrm{p}(E_\mathrm{p})\, E_\mathrm{p}\, \mathrm{d}E_\mathrm{p}\right) \tag{2.32}$$

$$\approx 1.3 \cdot 10^{44}\, \frac{\mathrm{TeV}}{\mathrm{Mpc}^3\,\mathrm{yr}}. \tag{2.33}$$

The power required for a source population to produce such energy density rates over the Hubble time H_0 is $\sim 5 \cdot 10^{44}\, \frac{\mathrm{TeV}}{\mathrm{Mpc}^3\,\mathrm{yr}}$, which works among others for Gamma Ray Bursts and active galactic nuclei [14].

Gamma Ray Bursts (GRBs) were discovered in the 1960s by American and Russian satellites, as they where monitoring space for nuclear explosions. However, their rate and distribution indicate that these objects are not man made. Soon it was realized that they are strong gamma ray eruptions, with luminosities

higher than observed for AGN

$$L_{\mathrm{GRB}} \approx 10^{51}\,\mathrm{erg/s} \tag{2.34}$$

$$L_{\mathrm{AGN}} \approx 10^{44-47}\,\mathrm{erg/s}. \tag{2.35}$$

More detailed observations with more sophisticated instruments like the BATSE detector furthered our understanding of GRBs, [15]. Observations show that they are distributed isotropically. Furthermore, absorption lines with $z = 0.835$ were observed, which was the first clear proof that these objects are extragalactic [16]. According to their duration, GRBs are divided into two groups, long GRBs (duration $> 2\,s$), which are associated with the death of massive stars and short GRBs (duration $< 2\,s$), which are believed to be the mergers of binary neutron stars.

The burst is followed by a longer-lived afterglow which is observed at longer wavelengths. The favored model which explains the observed phenomena is the fireball model. According to the fireball model a central engine-the massive star or neutron stars-eject large amount of matter outwards. A shock front is built up, where electrons and protons can be accelerated to high energies. Electrons lose energy due to synchrotron radiation, which can leave the shock region as soon as the region becomes optically thin. Protons can be accelerated to energies up to 10^{21} eV [3].

2.4 Neutrinos as messenger particles

The aim to answer the question of in which astrophysical environments and under which conditions high-energy CRs are produced face scientists with great challenges. CRs with energies $E_{\mathrm{CR}} \leq 10^{17}$ eV are deflected by interstellar magnetic fields, and thus do not point back to their origin [3].

At higher energies deflections caused by magnetic fields become small, so that directions can be at sufficient small distances correlated with the origin of high-energy particles. For a CR proton traveling a distance d through a constant magnetic field with perpendicular component $B_{\perp}$, the deflection from its origin trajectory is [17]

$$\phi(E, B) = 0.5^{\circ} \left(\frac{d}{\mathrm{Mpc}}\right) \left(\frac{B_{\perp}}{10^{-9}\,\mathrm{G}}\right) \left(\frac{E}{10^{20}\mathrm{eV}}\right)^{-1}. \tag{2.36}$$

However, CRs with $E \geq 10^{19}$ eV likely interact with the cosmic microwave background (CMB) and lose energy. According to this, $p\gamma$ interactions give a limit on the distance d to the sources can be given, see section 2.
Thus, low energy CRs are deflected by magnetic field, while high-energy CRs likely interact with the CMB. To avoid these difficulties, $\gamma-$rays and neutrinos which are assumed to be produced in the sources are observed.
$\gamma-$rays may undergo interactions with particles or photons on their way to the observer, see Figure 2.5 . Consequently, they may lose information about intrinsic conditions within the source. Additionally, detection of $\gamma-$rays do not necessarily give strong constraints on hadronic models, since they can be produced in leptonic and hadronic interactions.
Due to their charge neutrality and small cross-sections neutrinos can travel long distances without any considerable interactions with matter on their way to Earth. Within astrophysical sources, neutrinos are produced in $p\gamma$ interactions,

$$p + \gamma \rightarrow \Delta^+ \rightarrow \begin{cases} p + \pi^0 & \text{fraction } \frac{2}{3} \\ n + \pi^+ & \text{fraction } \frac{1}{3}, \end{cases} \tag{2.37}$$

or in inelastic proton-proton interactions

$$p + p \rightarrow \begin{cases} p + p + \pi^0 & \text{fraction } \frac{2}{3} \\ p + n + \pi^+ & \text{fraction } \frac{1}{3}. \end{cases} \tag{2.38}$$

where among others charged pions are produced which decay subsequently in neutrinos of different flavor. However, these advantages can turn into disadvantages. Large telescopes have to be built to have enough events.

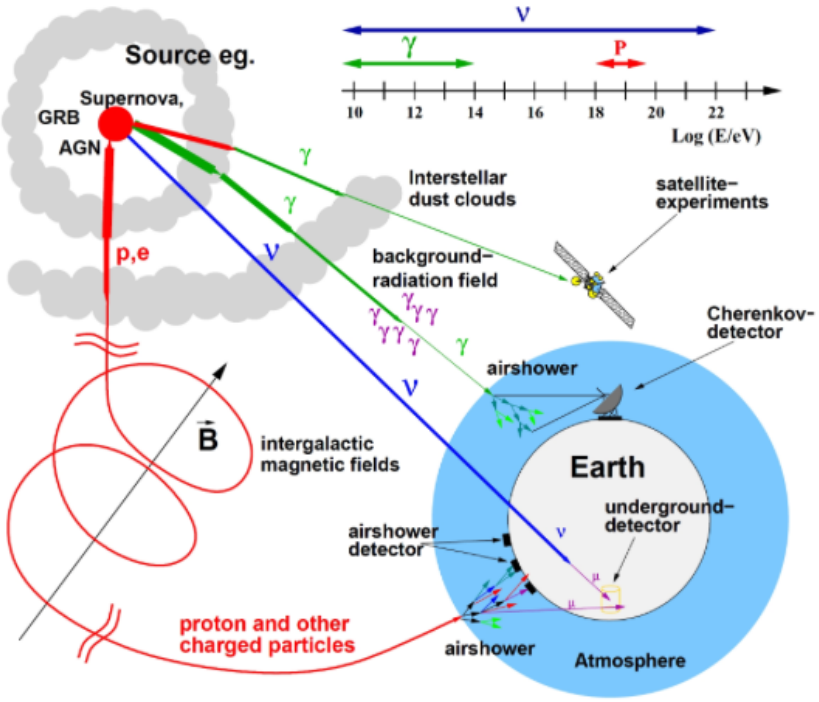

FIGURE 2.5: Low energy CRs are deflected by magnetic fields, while high energy CRs interacts with photon fields. High energy $\gamma-$rays interact with particles or photon fields, while neutrinos can travel long distances without any considerable interactions [18].

2.5 Neutrino telescopes

More than 100 years after the detection of high-energy CRs the question of where they are generated and how they are accelerated is still under great debate.
Neutrinos are expected to be produced along with $\gamma-$rays in astrophysical sources in processes involving pure hadronic or photo-hadronic interactions.
The small cross-sections and charge neutrality make a detection challenging, as described in section 2.4. Already in the late 1970s it was proposed to build large neutrino detectors, by using target material found in nature to have enough events

[19]. The detector material will be equipped with light sensors which detect emitted Cherenkov light of generated leptons. These leptons are produced in charge-current interactions when a neutrino interacts with a particle:

$$\nu_\mu(\overline{\nu}_\nu) + N \rightarrow \mu^\mp + X \tag{2.39}$$

$$\nu_\tau(\overline{\nu}_\tau) + N \rightarrow \tau^\mp + X \tag{2.40}$$

$$\tau^\mp \rightarrow \mu^\mp + \overline{\nu}_\mu(\nu_\mu) + \nu_\tau(\overline{\nu}_\tau) \tag{2.41}$$

$$\nu_e(\overline{\nu}_e) + N \rightarrow e^\mp + X \tag{2.42}$$

Generated muons travel faster than light in the medium and therefore emit Cherenkov radiation, Figure 2.6 (left). This radiation can be detected by Optical Modules consisting of **P**hoto **M**ultiplier **T**ubes (PMTs) which are in pressure resistant glass shells.

To distinguish between between atmospheric muons and muons generated within the detector, a telescope located at the Southern Hemisphere focus on the Northern Hemisphere and vice versa. This can be explained in the following: A telescope located in the Southern Hemisphere will mainly detect muons reaching the detector through Earth, as these must be generated by a neutrino interaction close to the detector. Atmospheric muons are absorbed in the upper layers. Thus, the Earth can be used as a filter.

At higher energies ($E_\nu \sim EeV$) [20] neutrinos are absorbed by the Earth as well. However, in this energy region the atmospheric background is negligible and events from above the horizon can be included in the analysis.

Electron and tau neutrinos can also be observed. However, a generated electron scatters many times before losing enough energy to fall below the threshold energy for Cherenkov radiation. Thus, that electron neutrino events cannot be used to point back to sources. Such events are more spherical, or cascade-like, than track like, see Figure 2.6 (right).

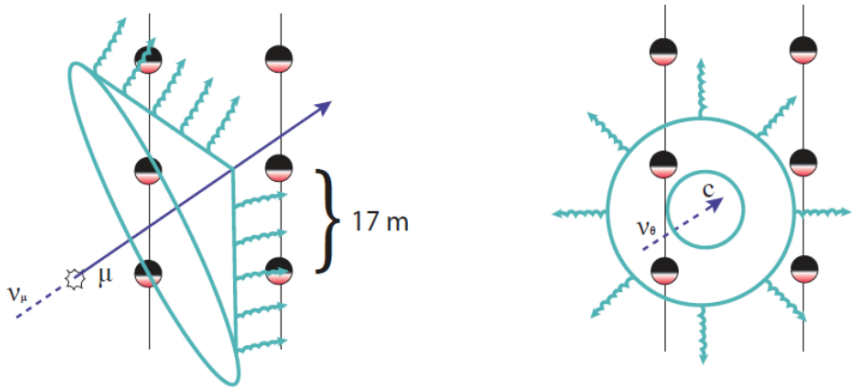

FIGURE 2.6: Schematic illustration of a neutrino detector. When a muon neutrino interacts with an ice molecule a muon is produced, which travels faster than light in the medium (left). It emits Cherenkov radiation, which can be detected by optical modules. Leptons which are produced in electron and tau neutrino interactions with ice molecules have cascade like events (right) [19].

Track like and cascade like events have advantages and disadvantages. Muon tracks can be used to reconstruct the neutrino direction. Furthermore, skymaps can be produced, which is the key to find neutrino sources. The disadvantage: It is difficult to determine the neutrino energy since events are not contained.
As opposed to this cascades are contained and provide a good energy reconstruction for each event. Furthermore, the background of atmospheric ν_e is significantly lower, and there is almost no atmospheric ν_τ. On the other hand the directional information for cascade events is $\geq 10°$.

ANTARES is currently the largest underwater neutrino telescope in the Northern Hemisphere [21],[22]. Its instrumented detector volume is about 0.02 km^3 and consists of twelve vertical strings equipped with 885 PMTs, installed at a depth of about 2.5 km.
The main goal is the detection of high-energy cosmic neutrinos through measurement of Cherenkov radiation. A further field of research is the measurement of atmospheric muon neutrino oscillation and magnetic monopoles [22].

Km3NeT is a future neutrino telescope which will be located at the bottom of the Mediterranean Sea. Its instrumented detector volume is planned to be more than five km^3, [23]. It will contain about 12000 glas spheres, which are attached to about 600 strings. Each glas sphere will contain 31 PMTs. The scientific goal of KM3NeT is the observation of neutrino sources in particular in a region of the sky complementary to the field of view of IceCube. The sensitivity will be better

than the sensitivity of the IceCube detector, [23]. For the southern sky KM3NeT will have a sensitivity of approximately two orders better than ANTARES.

IceCube is currently the largest operating neutrino detector, located at the south pole. Its instrumented detector volume is about one km^3, consists of spherical optical sensors, called **D**igital **O**ptical **M**oduls (DOMs). Each DOM contains a PMT. The DOMs are arranged on 86 strings frozen into the antarctic ice at depths from 1450 m to 2450 m. The installation started 2005 and ended in December 2010. IceCube recently reported the detection of high-energy neutrino events, breakthrough of the year 2013 [24].

2.5.1 IceCube Gen2

As mentioned in section 2.4 neutrino interactions are rare due to their small cross-sections. Consequently, the larger a neutrino telescope, the more events can be detected within the detector. The recent observations of high-energy neutrinos with the current $1\,km^3$ detector opens a new window in the field of astrophysics. To detect EeV energy neutrinos and to have a larger number of neutrino events, it is planned to extend the current detector to a second generation telescope, IceCube-*Gen2*. Its instrumented volume will be approximately 10 km^3. Details of the design, such as the inter-string separations and deployment geometries are still under debate [25].

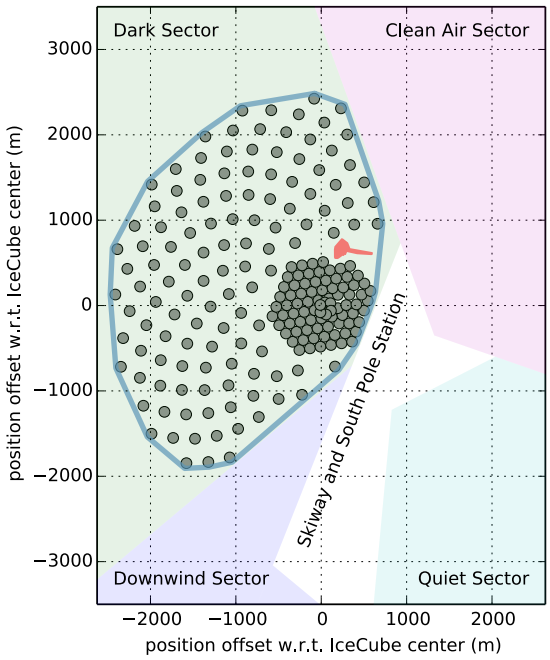

FIGURE 2.7: Construction of the IceCube-*Gen2* telescope [25]. The gray hexagon area represents the current 1 km^3 IceCube detector. The final geometry of IceCube-*Gen2* is still under debate.

With its unprecedented sensitivity and improved angular resolution IceCube-*Gen2* will have the potential to detect EeV-energy GZK neutrinos, which are produced in $p\gamma$ interactions. High energy protons interact on their through the Universe with CMB photons:

$$p + \gamma \rightarrow \Delta^+ \rightarrow n + \pi^+. \tag{2.43}$$

The charged pions decay subsequently into EeV-energy neutrinos, which can be detected with the *Gen2* telescope. A detailed introduction of IceCube-*Gen2* can be found in [25].

Table 2.1 gives an overview of some important parameters for current and future installed neutrino telescopes.

-	Location	I. V. in km^3	Strings	PMTs
ANTARES	N. H.	0.02	12	885
IceCube	S. H.	1	86	5160
KM3NeT	N. H.	5	600	$3.72 \cdot 10^5$
IceCube Gen2	S. H.	10	not yet known	not yet known

TABLE 2.1: Some important parameters for current and future neutrino telescopes, with N. H.= Northern Hemisphere, S. H.= Southern Hemisphere, I. V.= instrumented volume.

2.5.2 Detection of high-energy neutrinos with the IceCube detector

The IceCube collaboration reported the detection of high-energy neutrinos with energies in the range of $30\,\text{TeV} \leq E_\nu \leq 1200\,\text{TeV}$ [24], which can be explained by extragalactic sources like galaxy clusters, GRBs or AGN. Galactic sources can be ruled out in all likelihood, since only up to two sub-PeV neutrinos might be produced in galactic sources [26]. Furthermore, in [27] it is shown that the predicted diffuse neutrino flux from SNRs is at least a factor of 20 below the detected diffuse neutrino signal.

The hard spectrum, the isotopic distribution, the energy spectrum and shower to muon track ratio of the observed events indicate that these high-energy neutrinos are likely originating from extragalactic sources.

Seven of the events have muon like events, the rest are either electromagnetic or hadronic showers.

The excess is well fitted by a power-law function [24]

$$\phi_{\text{IceCube}}(E_\nu) = \phi_0 \cdot E_\nu^{-\alpha} \tag{2.44}$$

$$= (1.2 \pm 0.4) \cdot 10^{-8}\, E_\nu^{-2} \qquad \frac{1}{\text{GeV}\,\text{s}\,\text{cm}^{-2}\,\text{sr}}. \tag{2.45}$$

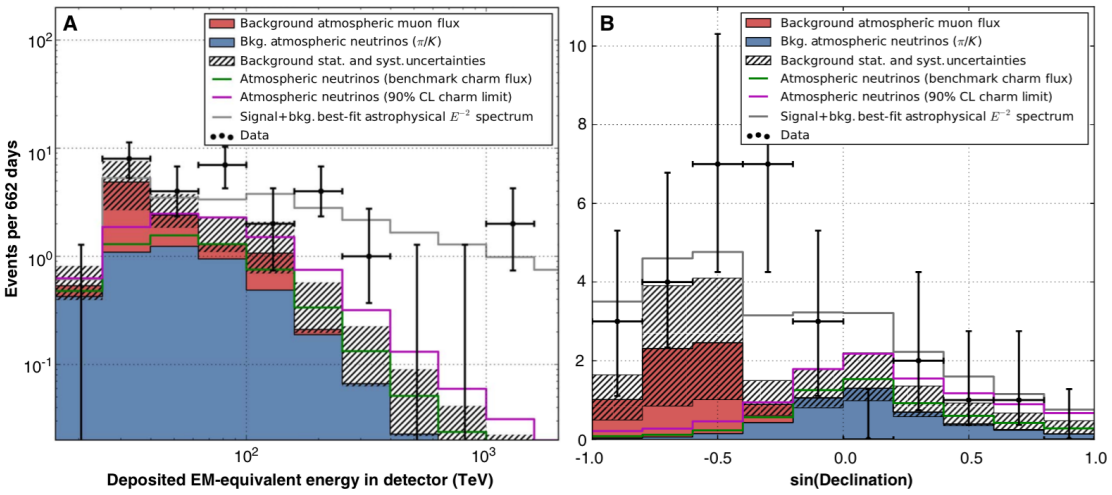

FIGURE 2.8: Energy distribution (left), and declination angle distribution (right) of the observed neutrino events. The black dots give the observed neutrinos. The blue area gives the expected atmospheric neutrinos, while the green line shows the IceCube benchmark atmospheric neutrinos. The red area gives the background of atmospheric muons. The gray line shows the best fit E_ν^{-2} astrophysical spectrum with a flavor ratio (1:1:1) of $\phi_\nu(E_\nu) = \phi_0\, E_\nu^{-2}$ [24].

Despite of all difficulties and due to low statistics it is expected that the diffuse flux which is described by E_ν^{-2} shape generates three to six additional events in the energy range $2\,\mathrm{PeV} \leq E_\nu \leq 10\,\mathrm{PeV}$ [24]. The lack of these events can be explained by a softer spectrum or the presence of a break or a cut-off.

Indeed, the use of more statistics confirms that the flux is softer, with a spectral index α in the range $2.3 \leq \alpha \leq 2.46$ [28]:

$$\phi_{\mathrm{IceCube}}(E_\nu) = \phi_0\, E_\nu^{-\alpha} \tag{2.46}$$

$$= 2.06^{+0.4}_{-0.3}\, 10^{-6.5}\, E_\nu^{-2.3} \qquad \frac{1}{\mathrm{GeV\,cm^2\,s\,sr}} \tag{2.47}$$

$$= 2.06^{+0.4}_{-0.3}\, 10^{-5.7}\, E_\nu^{-2.46} \qquad \frac{1}{\mathrm{GeV\,cm^2\,s\,sr}}. \tag{2.48}$$

Chapter 3

Active galactic nuclei

Most galaxies we observe are "normal" galaxies, meaning that the observed radiation is coming from stars, with small parts from excited dust and gas. The spectrum of a star is well approximated by the spectrum of a black body radiator. Consequently, spectra of "normal" galaxies are a superposition of stellar spectra. However, there is a group of galaxies which have strong and broad emission lines, indicating that the line emitting regions have velocities up to several thousand of $\mathrm{km\,s^{-1}}$. The very high excitation energies required to have such emission lines cannot be produced by stars, and thus have to be produced by other mechanism. Emission from these galaxies is spread widely across the electromagnetic spectrum, often peaking in the ultra-violet, with significant luminosity in the X-ray and infrared bands. In comparison to normal galaxies where no flux variations occurs, variations for these special group of galaxies are observed. Their fluxes vary on time scales of years, days or minutes. The fact that the energy output varies on extreme short time scales, indicates that the emission size is a compact region, with a size of approximately our solar system. This region which is responsible for the extreme high energy output and which outshines its host galaxy is called Active Galactic Nucleus (AGN). Very Long Baseline Interferometry (VLBI) observations give upper limits for the emission size, $r \leq 1$ pc [29].
The prevalent picture of an AGN is a super-massive black hole with a mass of

$$M \geq 10^{10} \left(\frac{r}{100\,\mathrm{pc}} \right) \mathrm{M}_{\odot}, \tag{3.1}$$

which is surrounded by a disk [29]. Here r denotes the size of the emitting region and $\mathrm{M}_{\odot}$ the solar mass. Matter within the disk orbits the black hole and will be

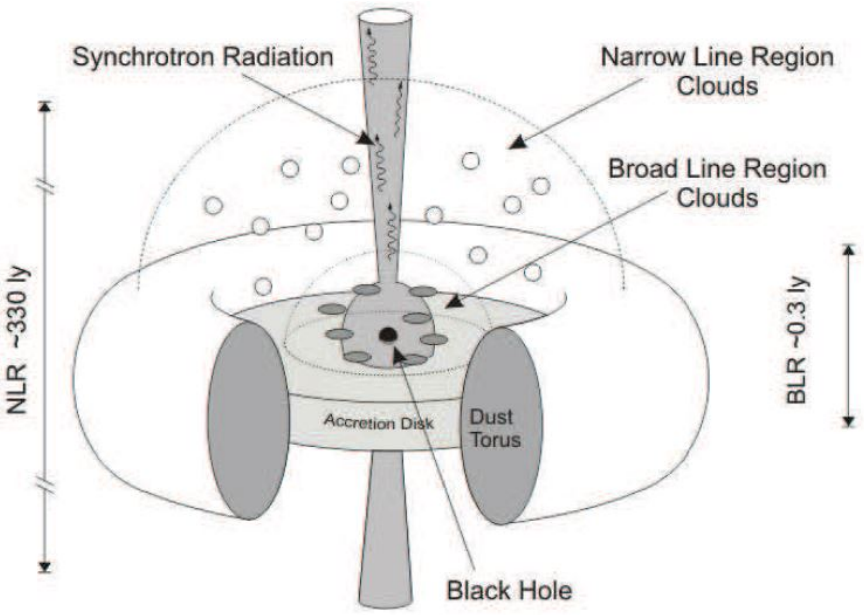

FIGURE 3.1: Schematic view of an AGN. The super massive black hole, the engine of the AGN is surrounded by a disk. Depending on the inclination angle i the AGN is classified as Blazar ($i = 0°$) or a radio galaxy ($i \approx 20°$) [30].

swallowed. Only a fraction of the falling matter can reach the black hole. The rest is ejected, escapes and forms two twin collimated plasma jets, strong radio sources if the host galaxy of the AGN is elliptical and weak radio sources if its a gas rich spiral. The observed optical and ultra-violet lines are produced by fast moving broad line clouds, while narrow emission lines are produced by slowly moving clouds, see Figure 3.1.

AGN are promising candidates to accelerate particles to the highest energies, and thus are believed to be sources of the CRs with energies $E_{\mathrm{p}} \geq 10^{18}$eV.

Adopting the unification scheme [31], observational differences between various AGN types can be explained among others as a result of different inclination angle i. For inclination angle $i = 0°$, the AGN is of type Blazar and for $i \approx 90°$ it is a Seyfert galaxy.

It will be assumed that in AGN protons are accelerated to highest energies. Furthermore, it will be assumed that neutrinos are produced in inelastic proton-proton interactions.

Chapter 3 is structured as follows:

In section 3.1 the current picture of an AGN, the transport of angular momentum is explained.

In section 3.2 mass accretion into the black hole is explained. In some AGN superluminal motions are observed, which will be explained in section 3.3. Section

3.4 deals with radio emission from relativistic electrons within the jet.
As mentioned AGN are classified according to their inclination angle i. Section 3.5 and section 3.6 deal with Fanaroff-Riley galaxies and Blazars. Section 3.7 gives a brief introduction into the radio luminosity functions for FR galaxies and Blazars, needed to calculate neutrino fluxes.
Since AGN are distant objects cosmological effects will be considered in section 3.8.
The last section 3.9 deals with the unification scheme of AGN.

3.1 Transport of angular momentum

Assuming a geometrically thin and cylindrical disk, with a given surface mass density ρ. Particles within the disk fulfill keplerian motions.
We follow the theory, explained in [32] by assuming angular momentum transfer due to random motion of matter within the disk.
Consider two particles A and B located on two annuli which fulfill keplerian motion, Figure 3.2

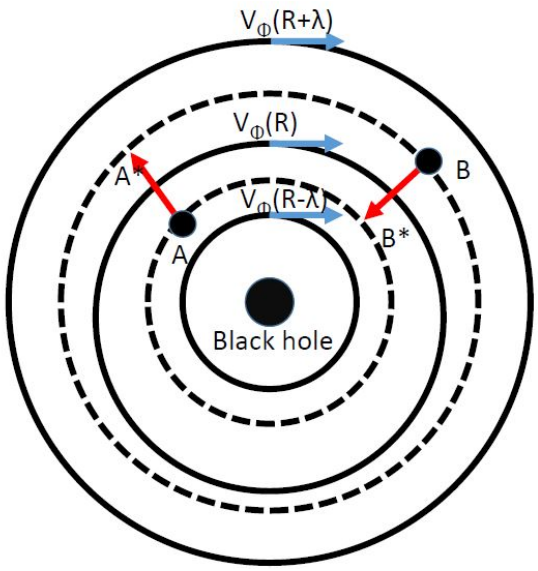

FIGURE 3.2: Schematics of particle transport across a boundary. Particle one moves from A to A^* and particle two from B to B^*.

Particle A is located at $R - \frac{\lambda}{2}$ and has a azimuthal velocity $v_\phi^{\mathrm{A}}(r)$ which is higher than the azimuthal velocity of particle B at $R + \frac{\lambda}{2}$:

$$v_\phi(r) = \Omega(r) v(r) \tag{3.2}$$

$$v_\phi\left(r - \frac{\lambda}{2}\right) = \Omega\left(r - \frac{\lambda}{2}\right) v\left(r - \frac{\lambda}{2}\right) \tag{3.3}$$

$$> v_\phi\left(r + \frac{\lambda}{2}\right) \tag{3.4}$$

The net transfer of angular momentum ($L = m v_\phi r$) due to viscous transport is given by:

$$\frac{\Delta L}{\Delta t} = -G(r) \tag{3.5}$$

$$= \frac{1}{\Delta t}\left(L_{B\to B'} - L_{A\to A'}\right) = \dot{m}_A\left(r + \frac{\lambda}{2}\right) v_\phi\left(r - \frac{\lambda}{2}\right) - \dot{m}_B\left(r - \frac{\lambda}{2}\right) v_\phi\left(r + \frac{\lambda}{2}\right) \tag{3.6}$$

$$\approx \dot{m}_A r^2 \Omega\left(r - \frac{\lambda}{2}\right) - \dot{m}_B r^2 \Omega\left(r + \frac{\lambda}{2}\right). \tag{3.7}$$

Since we deal with random motions of particles with velocity $\overline{v}$, there is no net transfer of matter, resulting in $\dot{m}_A = \dot{m}_B = \overline{v}\rho 2\pi r$:

$$G(r) = \overline{v} 2\pi r \rho r^2 \left(\Omega\left(r - \frac{\lambda}{2}\right) - \Omega\left(r + \frac{\lambda}{2}\right)\right)\frac{\lambda}{\lambda} \tag{3.8}$$

$$= \overline{v}\rho 2\pi r \lambda r^2 \frac{\mathrm{d}\Omega(r)}{\mathrm{d}r} \tag{3.9}$$

$$= 2\pi r \xi \rho r^2 \frac{\mathrm{d}\Omega(r)}{\mathrm{d}r}. \tag{3.10}$$

The parameter $\xi = \overline{v}\lambda$ is the kinetic viscosity. Equation (3.10) gives the transport of angular momentum across any r. The total change in angular momentum is due to viscous transport, equation (3.10) and by the transport linked with a flow of matter.

$$\frac{\mathrm{d}L}{\mathrm{d}t} = \frac{\mathrm{d}}{\mathrm{d}r}\left(\dot{m} r^2 \Omega(r)\right)\Delta r. \tag{3.11}$$

Consequently, it is

$$\frac{\mathrm{d}L^{\mathrm{tot}}}{\mathrm{d}t} = \frac{\mathrm{d}}{\mathrm{d}r}\left(\dot{m} r^2 \Omega(r)\right)\Delta r + \left[G\left(r + \frac{\lambda}{2}\right) - G\left(r - \frac{\lambda}{2}\right)\right]. \tag{3.12}$$

Beside angular momentum transport, shear forces play an important role[1]. Assuming a cylindrical disk, the disk luminosity and shear forces are linked via:

$$L(r) = 2\int_r^\infty \mathrm{d}r\, F(r) 2\pi r \tag{3.13}$$

$$= \int_r^\infty \mathrm{d}r \left(\underbrace{\frac{3\Gamma M\dot{m}}{8\pi r^3}\left(1-\left(\frac{r}{r_s}\right)^{0.5}\right)}_{F(r)} \right) 2\pi r \tag{3.14}$$

$$= \frac{\Gamma M\dot{m}}{2r}. \tag{3.15}$$

If the disk is optically thick, the disk temperature can be calculated by applying the Stefan-Boltzmann law:

$$L = \sigma_{\mathrm{SB}} A_{\mathrm{disk}} T^4 \tag{3.16}$$

$$T(r) = \left(\frac{3\,\Gamma\, M_\bullet \dot{m}}{8\pi\sigma_{\mathrm{SB}} r_{\mathrm{S}}^3}\right)^{1/4} \left(\frac{r}{r_{\mathrm{S}}}\right)^{-3/4} \tag{3.17}$$

$$= \left(\frac{3\,\dot{m}c^6}{64\pi\sigma_{\mathrm{SB}}\Gamma M_\bullet^2}\right)^{1/4} \left(\frac{r}{r_{\mathrm{S}}}\right)^{-3/4}, \tag{3.18}$$

with σ_{SB} giving the Stefan-Boltzmann constant. The disk temperature increases for lower radii, $T(r) \propto r^{-3/4}$. The total emission of the disk is a superposition of many black body radiators, consisting of different rings with different temperatures. For this reason, the resulting disk spectrum deviates from a Planck spectrum.

For a fixed ratio r/r_{s} the disk temperature increases, for increasing $\dot{m}$, since it is $T \propto \dot{m}^{1/4}$. This behavior is expected since higher mass accretion results in higher shear forces, and thus in higher luminosities, equation (3.15).

For increasing black hole mass $M_\bullet$, the temperature decreases, which is unexpected, but can be explained in the following. For higher $M_\bullet$ and fixed r/r_{s} tidal forces decrease which results in lower temperatures. Consequently, the maximum disk temperature of an AGN is much lower than the disk temperature of stellar objects. For neutron stars and black holes hard $\gamma-$rays and X-rays are observed, while for AGN disks radiations only up to UV-range are observed.

[1] A detailed derivation of shear forces can be found in [32]

3.2 AGN mass

To have an estimate for the lower bound of the AGN mass it is assumed that the falling matter is completely ionized. By spiraling into the black hole particles lose their gravitational energy. Half of the gravitational energy is transferred into heat which will be radiated and interacts with particles which spiral down into the black hole. Particle photon interaction is more likely for electrons, since they are much lighter than protons. To guarantee that the falling matter is not blown away, the radiation force $F_{\text{rad.}}$ must be smaller than the gravitational force $F_{\text{grav.}}$. Since electrons are much lighter than protons their contribution to the gravitational force is negligible, and only protons will have a significant contribution:

$$F_{\text{rad.}} < F_{\text{grav.}} \tag{3.19}$$

$$\sigma_{\text{T}} \frac{L}{4\pi r^2 c} < \Gamma \frac{M_\bullet m_{\text{p}}}{r^2} \tag{3.20}$$

$$M_\bullet < \sigma_{\text{T}} \frac{L}{4\pi\, c\, \Gamma\, m_{\text{p}}} \tag{3.21}$$

$$< 8 \cdot 10^7 \left(\frac{L}{10^{46}\,\text{erg/s}} \right) \text{M}_\odot \tag{3.22}$$

Thus, the luminosity of an AGN limits the black hole mass. For high luminous AGN masses up to $10^{10}\,\text{M}_\odot$ and for low luminous ones masses up to $10^6\,\text{M}_\odot$ can be set as a lower bound. These results base on the assumption of isotropic emission within AGN. Due to the jets which emit a large amount of the luminosity, see Figure 3.1, the intrinsic emission is anisotropic, and thus the measured luminosity may deviate from the assumption of isotropic emission. Thus, equation (3.22) is not sufficient enough to give the lower bound for the black hole mass. Nevertheless it gives a first approximation and a plausible range for the lower bound.
One of the questions concerning AGN is how, much matter the black hole accretes. Observations can be used to have a better understanding.
Assuming that the fraction $\epsilon < 1$ of the falling matter is transferred into energy, the accretion rate is given by

$$\frac{\text{d}E}{\text{d}t} = L \tag{3.23}$$

$$\epsilon \dot{m}\, c^2 = 8 \cdot 10^7 \left(\frac{L}{10^{46}\,\text{erg/s}} \right) \text{M}_\odot \tag{3.24}$$

$$\dot{m} \approx 0.18 \frac{1}{\epsilon} \left(\frac{L}{10^{46}\,\text{erg/s}} \right) \left(\frac{\text{M}_\odot}{1\,\text{year}} \right). \tag{3.25}$$

Assuming $\epsilon \approx 0.1$, maximal efficiency, and a maximal luminosity, given by the Eddington luminosity L_{edd}, the maximum accretion rate is

$$\dot{m}_{\text{Edd}} \approx 2\,10^{-8}\,M_{\bullet}\,\frac{1}{\text{yr}}, \tag{3.26}$$

and the growth rate of an AGN

$$t_{\text{growth}} = \frac{M_{\bullet}}{\dot{m}} = \left(\frac{L}{L_{\text{Edd}}}\right)^{-1} 5\,10^{7}\,\text{years}. \tag{3.27}$$

It gives the time until the black hole reaches a mass of $M_{\bullet}$. Mass accretion is not the only mechanism which helps the black hole to increase its mass. Fusion of two smaller black holes, or collision of two galaxies is another possibility.

3.3 Superluminal motion

Beside the question concerning the origin of the observed high energy outputs in AGN, which can be answered by the presence of a super massive black hole, there is another hint for a black hole as the engine of an AGN, superluminal motion.
Observations show that there are components in AGN, moving faster than the speed of light, $v_{\text{app.}} > c$. Consider two components, the AGN core and a blob within the jet, which are observed with an angular distance $\theta(t)$. Thus, the apparent velocity is given by

$$v_{\text{app.}} = \frac{\mathrm{d}r}{\mathrm{d}t} = D\frac{\mathrm{d}\theta(t)}{\mathrm{d}t}, \tag{3.28}$$

with $r = D \cdot \theta(t)$, giving the transversal distance to the observer. VLBI observations show for compact radio sources $v_{\text{app.}}$ up to $5c$, which is not allowed concerning special relativity [29]. A first attempt to explain these observations was that the cosmological interpretation of the observed redshifts must be wrong and AGN should be close objects. Thus, the distance to the observer D would be small and $v_{\text{app.}}$ smaller than c. However, observations of more than 40 years confirm that redshift measurements for AGN are excellent methods to calculate distances. Consequently, a different mechanism is the reason for the observed velocities. The explanation combines fast movements of AGN components with the finite speed of light:
A component within the AGN jet moves with velocity v, and with an angle α with

respect to the observer, see Figure 3.3. It emits a photon at $t = 0$, moves a time t_A and emits another photon. The observed transversal distance is

$$\Delta r = v\, t_\mathrm{A} \sin(\alpha). \tag{3.29}$$

The object has a smaller distance at the time t_A and thus the photon needs less time to reach us. The photon emitted at the time $t = 0$ and $t = t_\mathrm{A}$ are observed with a time difference of

$$\Delta t = t_\mathrm{A} - \frac{v\, t_\mathrm{A} \cos(\alpha)}{c} = t_\mathrm{A}\,[1 - \beta \cos(\alpha)] \tag{3.30}$$

$$\beta = \frac{v}{c} \tag{3.31}$$

Considering equation (3.29) and (3.30) gives the apparent velocity

$$v_\mathrm{app} = \frac{\Delta r}{\Delta t} = \frac{v \sin(\alpha)}{(1 - \beta \cos(\alpha))}. \tag{3.32}$$

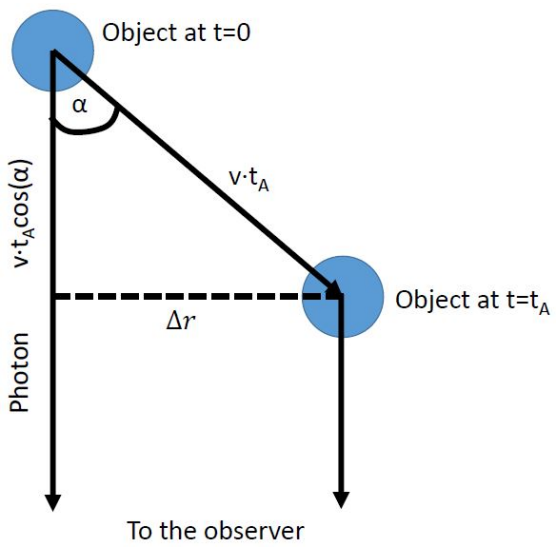

FIGURE 3.3: An objects moves with velocity v and angle α towards the observer. It emits a photon at a time $t = 0$ moves with v a distance $v\, t_\mathrm{A}$ and emits another photon at $t = t_\mathrm{A}$. The apparent distance is Δr and the apparent velocity $\frac{v \sin(\alpha)}{(1-\beta \cos(\alpha))}$.

For high velocities v and small angles i, $v_\mathrm{app.}$ increases, $v_\mathrm{app.} > c$, although the object moves with $v < c$. From equation (3.30) two interesting conclusions can be found. For an object with a fixed velocity v the maximum apparent velocity is

fixed by:

$$\frac{\mathrm{d}v_{\mathrm{app}}}{\mathrm{d}\alpha} = \frac{v\cos(\alpha)(1-\beta\cos(\alpha)) + \beta\, v\sin(\alpha)^2}{((1-\beta\cos(\alpha))^2)} = 0 \tag{3.33}$$

$$= \frac{v\cos(\alpha}{(1-\beta\cos(\alpha))} = \frac{\beta\, v\sin(\alpha)^2}{(1-\beta\cos(\alpha))^2} \tag{3.34}$$

$$= v\cos(\alpha)(1-\beta\cos(\alpha)) = \beta\, v\sin(\alpha)^2 \tag{3.35}$$

$$\Rightarrow \cos(\alpha)_{\mathrm{max}} = \beta \tag{3.36}$$

$$\Rightarrow \sin(\alpha)_{\mathrm{max}} = \sqrt{1-\cos(\alpha)^2_{\mathrm{max}}} = \sqrt{1-\beta^2} = \frac{1}{\gamma}. \tag{3.37}$$

To observe apparent velocities higher than c, the following inequation has to be fulfilled

$$c > \frac{v\sin(\alpha)}{(1-\beta\cos(\alpha))} \tag{3.38}$$

$$\beta > \frac{1}{\sin(\alpha)+\cos(\alpha)} \geq \frac{1}{\sqrt{2}} \approx 0.707 \tag{3.39}$$

Superluminal motion is a consequence of the finite speed of light c and a consequence of high velocity objects within the AGN. This means, objects exist which can accelerate components within the AGN to these velocities. Promising candidates are super-massive black holes.
Consequently, superluminal motion and high energetic outflows from AGN are linked and well described by the presence of a super-massive black hole.

3.4 Radio emission from AGN jets

AGN are excellent radio sources. Their radio jets can reach sizes up to several Mpc. In the following section a brief introduction in synchrotron emission of electrons is given. Electrons moving through a magnetized medium with a magnetic field B follow a spiral trajectory and radiate since it is an acceleration motion. The energy output covers the entire energy range, from radio to $\gamma-$ray. Radiation of non-relativistic electrons is called *cyclotron* and from high energetic electrons *synchrotron* radiation. We focus on AGN, and thus deal with high energetic phenomena.
A relativistic electron moving at a pitch angle θ (i.e. $\vec{B}\cdot\vec{\beta_e} = B\,\beta_e\cos(\theta)$) within

a magnetized medium radiates energy:

$$\frac{\mathrm{d}\gamma}{\mathrm{d}t} = -\frac{16\pi c}{9}\left(\frac{e^2}{m_e c^2}\right)^2 u_B\,\beta_e^2\,\gamma_e^2\,\sin(\theta), \tag{3.40}$$

with $u_B = B^2/(8\pi)$ the energy density of the magnetic field, β_e the normalized electron velocity $\beta_e = v_e/c$ and $\gamma_e = E_e/m_e c^2$. For our calculation we assume that electrons are scattered by magnetic fields, and thus get isotropized on time scales much shorter than the synchrotron energy loss time. Consequently, averaging equation (3.40) over the pitch angle is:

$$\frac{\mathrm{d}\gamma}{\mathrm{d}t} = -\frac{4}{3}c\,\sigma_\mathrm{T}\frac{u_B}{m_e c^2}\beta_e^2\gamma_e^2, \tag{3.41}$$

with $\sigma_\mathrm{T} = \frac{8\pi}{3}\left(\frac{e^2}{m_e c^2}\right)^2$ for the Thompson cross-section.
Generalizing equation (3.41) for any charged particle with mass m and charge Z in units of the elementary charge e gives:

$$\frac{\mathrm{d}\gamma}{\mathrm{d}t} = -\frac{4}{3}\,c\,\sigma_\mathrm{T}\,\frac{u_B}{m_e c^2}Z^4\left(\frac{m_e}{m}\right)^3\beta^2\,\gamma^2. \tag{3.42}$$

As can be seen it is $\frac{\mathrm{d}\gamma}{\mathrm{d}t} \propto m^{-3}$. To undergo the same energy loss, a proton would have to have a Lorentz factor of $\gamma_p \approx 2000^2\gamma_e$ and its energy would have to be 2000^3 times higher. Consequently, electrons are the most efficient radiators.
The cooling time is defined as

$$t_\mathrm{cool} = \frac{E}{P} \approx 2.4\,10^5\,\frac{10^4}{\gamma}\left(\frac{B}{10^{-4}}\right)^{-2}\,\mathrm{yr} \tag{3.43}$$

$$P = \frac{\mathrm{d}E}{\mathrm{d}t}. \tag{3.44}$$

For relatively low energetic radio emission t_cool is high, and thus comparable with the lifetime of the radio sources.
However, high-energy electrons have much higher γ_e and cannot explain the extended radio jets. That means, local acceleration regions within the jet exist, where electrons can be re-accelerated to the highest energies [33].
To calculate the synchrotron spectrum for a relativistic electron population, the emitted power of a single electron will be convolved with the electron population $n(\gamma)\mathrm{d}\gamma = n_0\,\gamma^{-s}\,\mathrm{d}\gamma$.

Furthermore, we assume that all radiators peaks around the characteristic frequency $\gamma^2\,\nu_{\mathrm{L}}$:

$$F_\nu = \frac{1}{4\pi}\int_1^\infty \mathrm{d}\gamma\, n(\gamma)\, P_{\mathrm{sync}}(\gamma) \tag{3.45}$$

$$\propto \left(\frac{\nu}{\nu_{\mathrm{L}}}\right)^{-\frac{s-1}{2}} \tag{3.46}$$

$$\nu_L = e\,B/(2\pi m_e c) \tag{3.47}$$

This is a power-law with an index $\alpha_{\mathrm{sync}} = -(s-1)/2$ which depends on the spectral index p of the electron population. For SNRs and in radio loud AGN this behavior is observed [34]. For the case that electron acceleration is perpendicular to the magnetic field B synchrotron emission is polarized. A detailed calculation gives a polarization degree of 70% for an isotropic electron distribution [34]. However in AGN lower values are observed, which can be explained by the fact that magnetic fields are strongly inhomogeneous.
In Figure 3.4 the synchrotron spectrum for a single electron (left) and an electron population (right) is shown. For frequencies below ν_1 electrons reabsorb their own radiation, synchrotron self-absorption.

3.4.1 Synchrotron self-absorption

In section 3.4 we assumed that all radiation emitted by the electron population within the AGN jet reaches Earth. However, this is a simplification since a low frequency photon will be absorbed by electrons within the source, know as synchrotron self-absorption.
An observer "sees" only low energy radiation coming from the outer layer of the source. The observed flux is smaller than if all photons escaped the source. For higher energies, photons from deeper regions within the source can reach the observer. For extreme energetic photons we can observe the interior of the source, since the mean free path of the photon is much larger than the source size. The self-absorbed region where the mean free path is small in comparison to the source size is called *optically thick*, while the remaining part where the mean free path is larger is called *optically thin*. Although the electron population is not thermal

distributed we can define an effective temperature

$$k_{\mathrm{B}} T_{\mathrm{eff.}}(\nu) \propto E \propto \nu^{1/2} \tag{3.48}$$

where we used the relation from equation (3.47). The spectrum is given by the Planck equation:

$$F_\nu(T_{\mathrm{eff.}}, \nu) = \frac{2\,h\nu^3}{c^3}\left(\exp\left(\frac{h\nu}{k_{\mathrm{B}} T_{\mathrm{eff.}}}\right) - 1\right)^{-1} \tag{3.49}$$

$$\tag{3.50}$$

For the low frequency tail the Rayleigh-Jeans limiting form will be used, which is:

$$F_\nu(T_{\mathrm{eff.}}, \nu) = \frac{2k_{\mathrm{B}} T_{\mathrm{eff}}\ , \nu^2}{c^2} \tag{3.51}$$

$$F_\nu(\nu) \propto \nu^{5/2}. \tag{3.52}$$

In equation (3.51) we used the relation from equation (3.48)

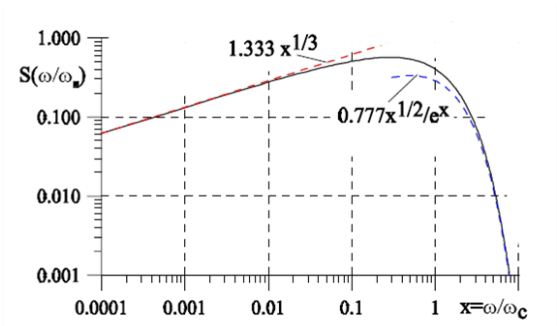

(A) Energy output of a single relativistic electron. The maximum energy output is located at a critical frequency ω_c [35].

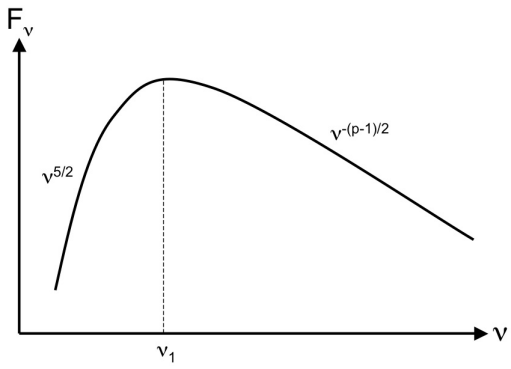

(B) Synchrotron spectrum for a power-law distributed electron population. Below $\nu_1 = \omega_1/(2\pi)$ photons are reabsorbed by electrons, synchrotron self absorption. Above ν_1 the spectrum decreases [36].

FIGURE 3.4: Left: Energy spectrum of a single relativistic electron. Right: Synchrotron spectrum for a electron population.

To sum up: For lower frequencies radiation is absorbed by electrons within the blob, and the spectrum is s independent. For increasing energy, the mean free path increases and photons can leave the source. The spectral shape depends on the electron spectrum s, Figure 3.4b.

3.5 Fanaroff-Riley I and II

AGN are divided into two groups, radio-loud and radio-weak AGN. Both groups are divided further into different sub-groups, Figure 3.5. Radio loud AGN can

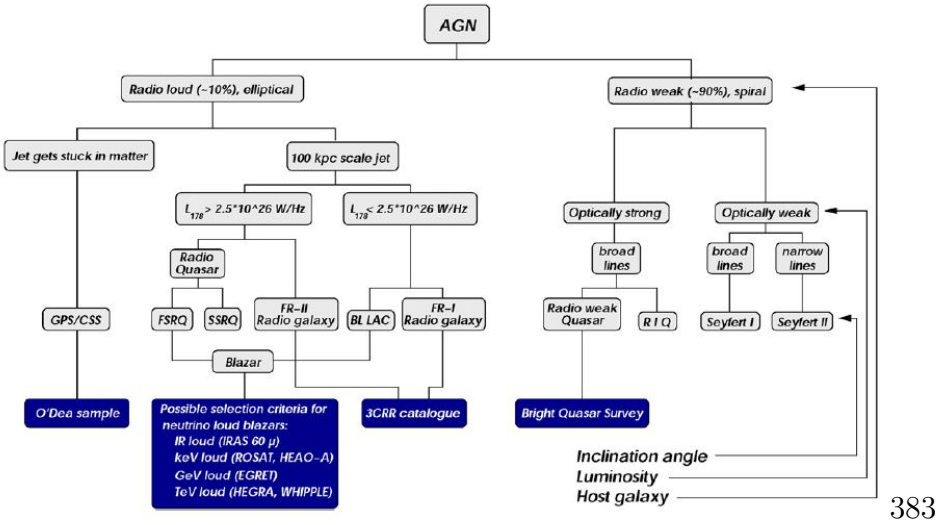

FIGURE 3.5: AGN sub-classes [37]

be classified according to their jet morphology. Prominent members of radio-loud AGN are among others Fanaroff Riley I (FR-I), Fanaroff-Riley II (FR-II) and Blazars.

FR-I galaxies are brightest close to the black hole. Their surface brightness decreases with increasing distance from the black hole, Figure 3.6a. They have radio luminosities up to $L_{\text{radio}}^{1.4\,\text{GHz}} \leq 10^{32}$ ergs^{-1}Hz^{-1}. In contrast, the surface brightness of **FR-II** galaxies increases with distance from the core, Figure 3.6b. Their radio luminosity is larger, in comparison to FR-I galaxies $L_{\text{radio}}^{1.4\,\text{GHz}} \geq 10^{32}$ ergs^{-1}Hz^{-1}. For small redshifts ($z < 0.5$), FR-I galaxies are located in galaxy clusters, while FR-II galaxies are often found to be hosted by field galaxies. For redshifts $z > 1$ both AGN types are found in rich environment [38]. Broadband imaging show that host galaxies of FR-II are bluer than host galaxies of FR-I and show signatures of mergers. On the other side, host galaxies of FR-I are more massive. Another

point is that optical spectra of FR-II hosts have emission lines, while this is almost never the case for FR-I optical spectra.

The origin of the "FR-I/FR-II dichotomy" is highly discussed. Many theories exist which try to answer the question, whether FR-I and FR-II galaxies may be same objects but with a different stage of development. One of the important contribution in this field is the Owen-Ledlow diagram, Figure 3.6c, where FR-I and FR-II galaxies are divided by a line [39]. The line goes roughly as $L_{\text{radio}} \propto L^2_{\text{optical}}$ and can be interpreted that FR-I galaxies evolve into FR-II sources.

Other theories which base on observations of emission lines try to explain differences mainly by accretion rate and spin of black holes. According to that in FR-I galaxies the accretion rate is lower, $\dot{m} \approx 10^{-3}\dot{m}_{\text{Edd}}$ compared with accretion rates in FR-II galaxies.

Kotanyi and Ekers observations of a small sample of radio galaxies showed that there is a perpendicularity of dust distribution and axis [40]. More sophisticated instruments, like the Hubble Space Telescope (HST) helped to extend the sample and to observe dust distribution on smaller scales within the host galaxy of the radio sources. Van Dokkum & Franx reported a possible link between dust presence and nuclear activity [41]. Further observations [42], [43] indicate that dust is distributed perpendicular to the radio axis, predominantly for FR-I sources. FR-II sources on the other hand showed less tendency for perpendicularity. Consequently, dust seems to play an important role for the classification of radio sources in FR-I and FR-II galaxies. Dust mass and dust distribution are important for AGN activities. Higher dust mass corresponds to higher accretion rates, and thus higher luminosities (FR-II galaxies), while lower masses correspond to lower luminosities (FR-I galaxies).

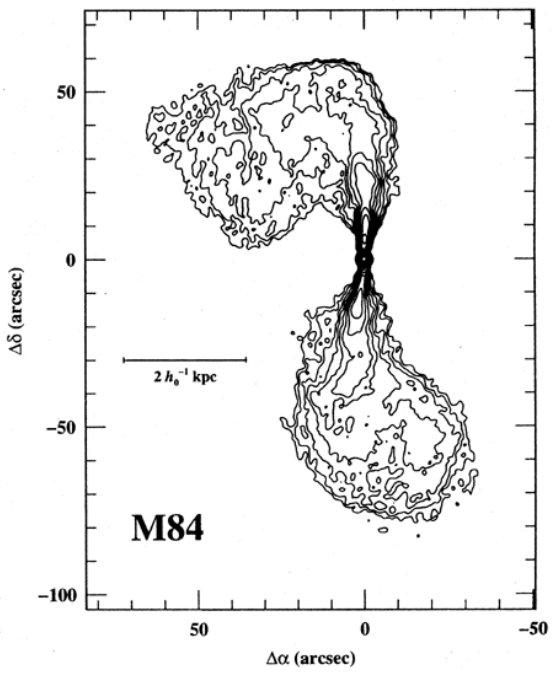

(A) Radio image of M 84 (FR-I) galaxy, base on 4.9 GHz observations by VLA. The AGN is brightest close to the core. The surface brightness decreases with distance from the core [44].

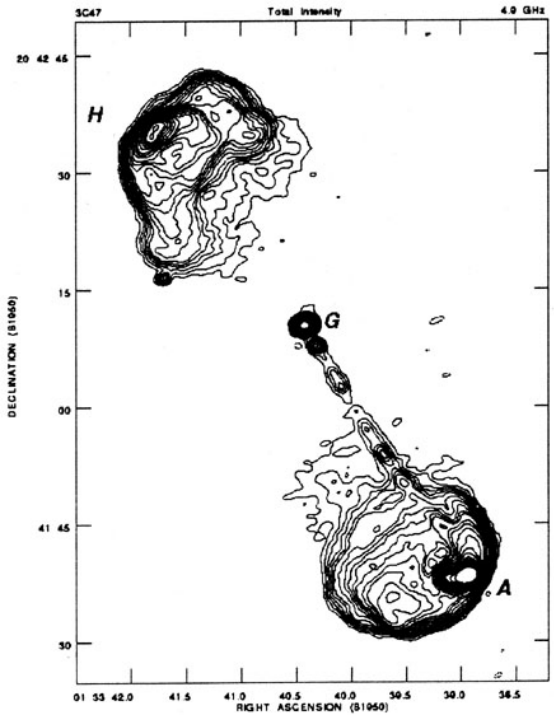

(B) VLA radio image of 3C 47 (FR-II). The brightness increases with distance to the core [45].

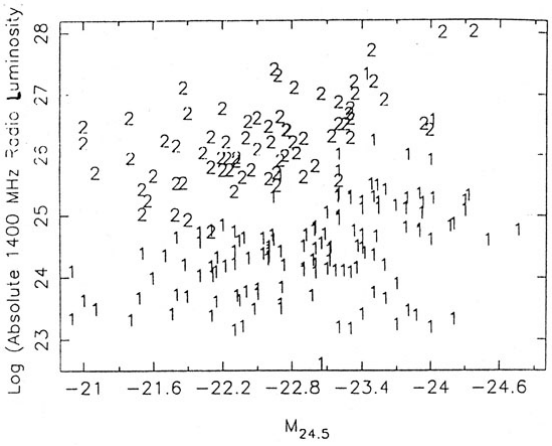

(C) Owen-Ledlow plot for FR-I (1) and FR-II (2) galaxies. The sources are divided by a line, with a slope of about 1.8 [39].

FIGURE 3.6: Radio images of FR-I (Figure 3.6a) and FR-II (Figure 3.6b) galaxies, and the Owen-Ledlow plot (Figure 3.6c)

3.6 Blazars

Adopting the unification scheme [31] Blazars are AGN whose jets point to the observer, and thus their physical properties are linked with the physics of the jet. The high energy output from the jet, its emanation from the vicinity of the black hole and its high degree of collimation offers information about the energy production close to the black hole. The presence of relativistic jets in Blazars can be established by the following arguments: Multi wavelength radio variability can be explained by relativistic shocks within the jet. Additionally strong and variable $\gamma-$ray emission implies a high compactness that the $\gamma-$ray source would inevitably be dominated by pair production unless the emission is relativistic. Furthermore, Blazars exhibit high brightness temperatures which imply high Doppler factors.

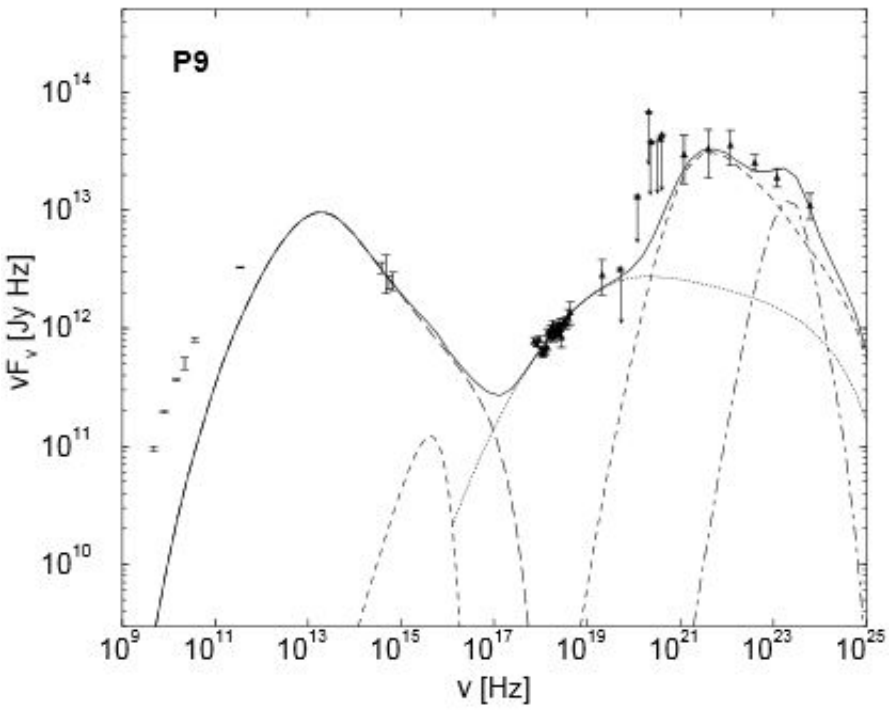

FIGURE 3.7: Energy spectra of Blazars. Two characteristic components can be found in the low and high energy regime. The low-energy component can be explained by synchrotron radiation, while the high-energy component can be explained by synchrotron-self Compton [46].

Blazar spectra show two characteristic components, a low-energy synchrotron bump and a high energy Compton scattered bump, Figure 3.7. The synchrotron component peaks from sub-infrared energies up to hard X-rays, while the Compton component peaks at higher energies.

Due to the small inclination angle $i \approx 0°$ and high Lorentz boost factors Γ_{B}, beaming effects have to be considered. Thus, the observed flux will be modified. Assuming a plasma blob moving with a relativistic velocity Γ_{B} and small inclination angle i, the observed luminosity and the intrinsic luminosity are related via [33]:

$$L_{\mathrm{obs.}} = \delta^{2+\alpha}\, L_{\mathrm{intr.}} \tag{3.53}$$

$$\delta = \frac{1}{\Gamma_{\mathrm{B}}\,(1 - \beta\cos(i))}. \tag{3.54}$$

Here, Γ_{B} gives the Lorentz boost factor of the blob and $\beta = \sqrt{1 - \frac{1}{\Gamma_{\mathrm{B}}^2}}$, i the inclination angle and α the spectral index.
Beaming effects give a good explanation for the strong variabilities observed in Blazars. For high velocities $\beta \leq 1$, small fluctuations in the jet velocity or in inclination angle i lead to strong fluctuations in δ, and thus in the observed flux. The effect of beaming in Blazars is explained in detail in [29], [33].
We focus on FR-I, FR-II and Blazars and use the radio luminosity function to calculate neutrino fluxes for these objects. For Blazars beaming effects will be considered, while for radio galaxies, due to small Γ_{B} and large i boosting effects are negligible.

3.7 Radio luminosity function

Our aim is to calculate the diffuse neutrino flux for FR-I, FR-II and for Blazars. Consequently, the total number of contributing objects, given by the luminosity function has to be considered.
To obtain the luminosity function for a specific AGN sub-class, the luminosity distance $d_L(z)$ and the local galaxy distribution have to be known. To achieve a galaxy distribution one has to consider large volumes, since the galaxy distribution is structured for scales $\sim 100\,\mathrm{Mpc}\,h^{-1}$. Otherwise faint galaxies can be observed only locally. That means, to calculate the luminosity function, for galaxies with small L, one has to concentrate on local galaxies. Despite the difficulties the global luminosity function will be approximated by a power-law function with an

exponential cutoff, the Schechter function

$$F(L,z) = \left(\frac{\eta*}{L^*}\right)\left(\frac{L}{L^*}\right)^{\alpha} \exp\left(-\frac{L}{L^*}\right) g(z). \tag{3.55}$$

The function $g(z)$ gives the z evolution, L^* gives the characteristic luminosity where the power-law form of $F(l,z)$ cuts off, α is the gradient and $\eta*$ gives the normalization.

For the calculation the radio luminosity function (RLF), giving the number of radio sources per co-moving volume $\mathrm{d}V_c$ and per unit logarithm of the radio luminosity is used. For FR-I galaxy the RLF is given by [47]:

$$F^{\text{FR-I}}_{\text{radio}}(L,z) = \eta^{\text{FR-I}}\left(\frac{L}{L^*_{\text{FR-I}}}\right)^{-\alpha_{\text{FR-I}}} \exp\left(-\frac{L}{L^*_{\text{FR-I}}}\right) \begin{cases} (1+z)^k & z < z_{\text{low}} \\ (1+z_{\text{low}})^k & z > z_{\text{low}}. \end{cases} \tag{3.56}$$

In addition to that, for FR-II galaxies the RLF is:

$$F^{\text{FR-I}}_{\text{radio}}(L,z) = \eta^{\text{FR-II}}\left(\frac{L}{L^*_{\text{FR-II}}}\right)^{-\alpha_{\text{FR-II}}} \exp\left(-\frac{L^*_{\text{FR-II}}}{L}\right) \begin{cases} \exp\left(0.5\left(\frac{z-z_{\text{high}}}{z_{h1}}\right)^2\right) & z < z_{\text{high}} \\ \exp\left(0.5\left(\frac{z-z_{\text{high}}}{z_{h2}}\right)^2\right) & z > z_{\text{high}}. \end{cases} \tag{3.57}$$

The characteristic terms η^X, L^*_X, z_X are constant and listed in table 3.1 and 3.2.

$\log_{10}(\eta^{\text{FR-I}})$	$\alpha_{\text{FR-I}}$	$\log(L^*_{\text{FR-I}})$	z_{low}	k
-7.53	0.586	26.48	0.710	3.48

TABLE 3.1: Used values for the radio luminosity function for FR-I galaxies for the current model of the Universe [47].

$\log_{10}(\eta^{\text{FR-II}})$	$\alpha_{\text{FR-II}}$	$\log(L^*_{\text{FR-I}})$	z_{high}	z_{h1}	z_{h2}
-6.747	2.42	27.39	2.03	0.568	0.956

TABLE 3.2: Used values for the radio luminosity function for FR-II galaxies for the current model of the Universe [47].

To calculate the total radio luminosity of the contributing objects, the RLF will be integrated:

$$L^{\text{total}}_{\text{radio}} = \int_L \int_z F^{\text{FR}}_{\text{radio}}(L,z)\,\mathrm{d}L\,\frac{\mathrm{d}V_c}{\mathrm{d}z}\,\mathrm{d}z. \tag{3.58}$$

The co-moving volume element $\mathrm{d}V_c$ and the RLF are cosmology dependent functions. In [47] the authors argue that their results for a $(\Omega_\mathrm{M}, \Omega_\lambda) = (0, 0)$ reproduce a ΛCDM cosmology with $(\Omega_\mathrm{M}, \Omega_\lambda) = (0.3, 0.7)$. Consequently, we use their results for the current picture of the Universe.
For Blazars the RLF is given by [48]:

$$F_\mathrm{radio}^\mathrm{Blazar}(L, z) = \eta^\mathrm{Blazar} \left(\left(\frac{L}{L_c(z)} \right)^\epsilon + \left(\frac{L}{L_c(z)} \right)^\lambda \right) \tag{3.59}$$

$$L_c(z) = 10^{a_0 + a_1 \cdot z + a_2 \cdot z^2}. \tag{3.60}$$

The parameters ϵ, λ and a_X are listed in table 3.3.

Parameter	Value
η^Blazar	$10^{0.85}\,\mathrm{Gpc}^{-3}$
ϵ	0.83
λ	1.96
a_0	24.89
a_1	1.18
a_2	-0.28

TABLE 3.3: Parameters for the radio luminosity function of Blazars. The used parameters are listed in [48].

The Blazar RLF in equation (3.59) is given for a flat Universe, i.e. $(\Omega_\mathrm{M}, \Omega_\lambda) = (0, 0)$. Nevertheless it is not necessary to repeat the modeling for other cosmologies since the RLFs for two different geometries are related via

$$F_1(L_1, z) \frac{\mathrm{d}V_{c,1}}{\mathrm{d}z} = F_2(L_2, z) \frac{\mathrm{d}V_{c,2}}{\mathrm{d}z}. \tag{3.61}$$

The luminosities $L_{1,2}$ are fixed by the flux-luminosity relation

$$S(L, z) = \frac{L}{4\pi d_L(z)^2}, \tag{3.62}$$

with $d_L(z)$ giving the redshift dependent luminosity distance.
As can be seen in equation (3.62), cosmological effects play an important role and have to be considered.

3.8 Cosmological effects

AGN are distant objects, and thus cosmological effects have to be considered.
If a neutrino is produced within an AGN which is distant ($z \gg 1$) cosmological effects like curvature and adiabatic energy loss play an important role. For nearby galaxies ($z \ll 1$) these effects can be neglected.
The Hubble parameter H_0 is the main parameter in cosmology which describes the Expansion rate of the universe

$$v = c \cdot z = H_0 \cdot d, \tag{3.63}$$

with d giving the distance to the object, z the redshift and v the recession speed. Current observations give a value for the Hubble constant [49]

$$H_0 \approx (74.3 \pm 2.1) \frac{\mathrm{km}}{\mathrm{s} \cdot \mathrm{Mpc}}. \tag{3.64}$$

The Hubble time

$$t_H \equiv \frac{1}{H_0} \approx 13.3 \cdot 10^9 \,\mathrm{year} \tag{3.65}$$

provides an estimate for the age of the Universe by presuming that the Universe has always expand at the same rate as it is expanding today. For small distances the curvature of the Universe is negligible and Euclidean metric can be applied. For large distances effects due the curvature have to be considered. The mass density ρ_0, the cosmological constant Λ, the curvature parameter k and the gravitational constant Γ can be transformed into dimensionless parameters

$$\Omega_M = \frac{8\pi\Gamma\rho_0}{3H_0^2} \tag{3.66}$$

$$\Omega_\lambda = \frac{\Lambda c^2}{3H_0^2} \tag{3.67}$$

$$\Omega_\mathrm{k} = -\frac{k}{c^2 H_0^2}, \tag{3.68}$$

which completely determine the geometry of the Universe if it is homogeneous and isotropic, and matter-dominated.
For large distances equation (3.63) cannot be used to calculate distances. For this reason one uses general relativity which describes the redshift of a distant object

correctly via the relation

$$1 + z = \frac{R(t_0)}{R(t_e)}, \tag{3.69}$$

where $R(t_0)$ gives the size of the Universe at the time the photon from the object was observed and $R(t_e)$ the time where it was emitted.

3.8.1 Co-moving volume & luminosity distance

The co-moving volume V_c is defined as the volume in which the number density of objects remains constant with time, assuming no evolution and that the objects are locked in the Hubble flow [50]. It is given by

$$\frac{\mathrm{d}V_c}{\mathrm{d}z} = d_\mathrm{H} \frac{(1+z)^2 d_\mathrm{A}^2}{\sqrt{\Omega_\mathrm{M}(1+z)^3 + \Omega_\mathrm{k}(1+z)^2 + \Omega_\Lambda}} \mathrm{d}\Omega, \tag{3.70}$$

with d_H giving the Hubble distance ($d_\mathrm{H} \equiv c/H_0$) and d_A giving the angular diameter distance [50].
The luminosity distance $d_L(z)$ is fixed by the relationship between the bolometric flux S (integrated over all frequencies) and bolometric luminosity L, equation (3.62). On the other hand it is related to the angular diameter distance via

$$d_L(z) = (1+z)^2 d_\mathrm{A}. \tag{3.71}$$

Thus, the cosmological parameters for our calculation are fixed and fluxes from distant AGN can be calculated.

3.9 Unification scheme

The physical properties of AGN are not fully understood yet. Sophisticated ground based and space telescopes help to have more and detailed information, and thus a deeper understanding. Observations indicate that many differences can be described within the unification framework. Differences are mainly explained by different inclination angle i:

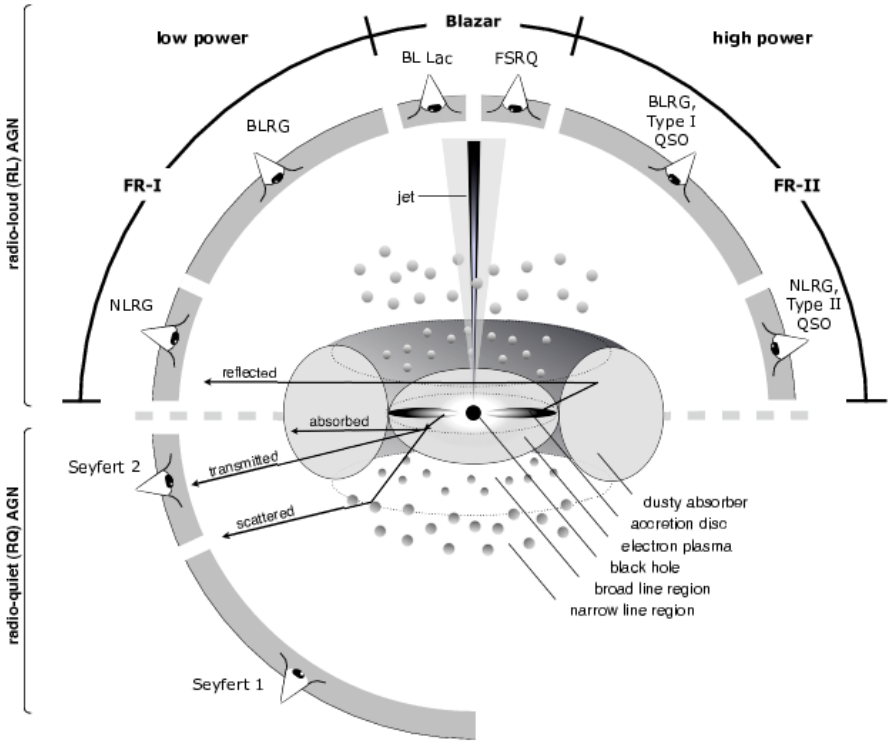

FIGURE 3.8: Schematic figure of an AGN. The observed appearance is among others a function of the inclination angle i [51].

- A super massive black hole with a mass up to $10^{10}\,\mathrm{M}_\odot$ is the source of the observed energies.
- The black hole is surrounded by matter which forms a disk due to angular momentum conservation. The continuum radiation in the optically and UV range is originating from the disk.
- Two high collimated opposed plasma jets are ejected, in which particles are believed to be accelerated to the highest energies. In AGN with high Doppler boosts only the approaching jet is observable, since the counter-jet is boosted out of our line of sight.
- Clouds which encounter the jet can be ionized.
- A direct view (for $i = 90°$) is not possible, since the dust torus prevent a direct observation of the core region.

Chapter 4

Transport equation

To give an accurate explanation of the proton flux $\phi_{\mathrm{p}}(E_{\mathrm{p}})$ in AGN, the transport equation will be solved. Protons and electrons undergo interactions among others with ambient matter, photon or magnetic fields which have large influences on the spectral shape of the particle flux.
In this work it will be assumed, that protons and electrons form a blob, moving along the jet, while they are accelerated through scattering at electromagnetic irregularities. Due to the blob size R which is much smaller than the distance of the blob to the observer d ($R/d \ll 1$), no spatial resolution of the blob is possible. Consequently, the energy/momentum solution of the transport equation is of interest.
Furthermore, no time variability in the particle number within the blob will be assumed, resulting in a time independent equation:

$$-Q(p) = \frac{1}{p^2}\frac{\partial}{\partial p}\left[p^2 D_{pp}\frac{\partial f(p)}{\partial p}\right] - \frac{1}{p^2}\frac{\partial}{\partial p}\left[p^2\left(\dot{p}_{\mathrm{gain}} + \dot{p}_{\mathrm{loss}}\right) f(p)\right] - \frac{f(p)}{T_{\mathrm{esc}}}. \tag{4.1}$$

The source function $Q(p)$ gives the number of injected protons with momentum p. The first summand on the right hand side gives the momentum diffusion, with D_{pp} giving the momentum diffusion coefficient. The second summand considers energy loss and energy gain processes.
Protons lose energy in inelastic $p - p$ interactions and adiabatic expansion of the blob, leading to an adiabatic deceleration of high energy particles. The last summand considers catastrophic losses due to particle escape.

4.1 Energy loss

To solve the transport equation, the parameters will be introduced in this section. Momentum loss for protons is considered by inelastic $p-p$ interactions and adiabatic expansion of the blob.
Interactions of high energy protons with different photon fields will not be discussed here, since the main focus is on inelastic $p-p$ interaction as main mechanism for neutrino production. Photohadronic interactions contain many unknown parameters which may lead to unprecise predictions.
Assuming that the mean Lorentz factor of created pions in the rest frame of the initial proton is

$$\overline{\gamma}_\pi = \gamma_{\mathrm{p}}^{\frac{3}{4}}, \tag{4.2}$$

the differential cross-section $\sigma^{\pi}_{n,\mathrm{pp}}(E_\pi, E_\mathrm{p})$ for the $n'th$ interaction can be approximated by a delta function [52]

$$\sum_n \sigma^{\pi}_{m,\mathrm{pp}}(E_\pi, E_\mathrm{p}) \approx \epsilon(E_\mathrm{p})\sigma^{\pi}_{\mathrm{pp}}(E_\mathrm{p})\frac{\delta(\gamma_\pi - \overline{\gamma}_\pi)}{m_\pi c^2} \tag{4.3}$$

$$\epsilon(E_\mathrm{p}) = \gamma_{\mathrm{p}}^{\frac{1}{4}} \tag{4.4}$$

Here, $\epsilon(E_\mathrm{p})$ gives the pion multiplicity, number of generated pions per one inelastic $p-p$ interaction and σ_{pp} the total inclusive cross-section in mb [53]. The pion power of a single relativistic proton is

$$P(E_\pi, E_\mathrm{p}) = 1.3\, c\, \gamma_\pi\, R\, n_\mathrm{H}\, \sigma_{\mathrm{pp}}\, \epsilon(E_\mathrm{p})\, \delta(\gamma_\pi - \overline{\gamma}_\pi) \tag{4.5}$$

The factor 1.3 considers the chemical composition of a target medium comparable to the interstellar medium, R gives the blob size and n_H the proton density. Integrating equation (4.5) over E_π, and considering the energy momentum relation for relativistic protons, $E = p \cdot c$, gives the momentum loss:

$$\dot{p}_{\mathrm{loss}} = -(1.3\, c\, \frac{m_\pi}{m_\mathrm{p}}\, \sigma_{\mathrm{pp}}(E_\mathrm{p})\, R\, n_\mathrm{H})\, p \tag{4.6}$$

$$= -a \cdot p. \tag{4.7}$$

4.1.1 Adiabatic deceleration

High-energy protons will diffuse due to random walk effect. Consequently, the blob size will expand. To give an accurate description of adiabatic energy losses it will be assumed that protons and electrons within the blob behave like an ideal gas. Results are given for a non-relativistic Maxwellian gas, but will be generalized for a relativistic gas.
When the blob is expanding it loses internal energy U, given by

$$\mathrm{d}U = -p\,\mathrm{d}V, \tag{4.8}$$

with p giving the pressure of the gas and V the volume of the blob. Assuming an ideal gas, $U = \frac{3}{2} n\, k_\mathrm{B}\, T\, V$ and $p = n\, k_\mathrm{B}\, T$ the energy loss is

$$\mathrm{d}U = n\, V\, \mathrm{d}E = -\frac{2}{3} n\, E\, \mathrm{d}V. \tag{4.9}$$

The average energy of each particle is $E = \frac{3}{2} k_\mathrm{B} T$, with T giving their temperature and k_B the Boltzmann constant. Consequently, it is

$$\frac{\mathrm{d}E}{\mathrm{d}t} = -\frac{2}{3}\frac{E}{V}\frac{\mathrm{d}V}{\mathrm{d}t}. \tag{4.10}$$

In [54] it is shown that $\mathrm{d}V/\mathrm{d}t = (\nabla \cdot \vec{v}(r))V$. The expansion velocity is given by $\vec{v}(r)$. The results will be adopted, which yields

$$\dot{p}_\mathrm{loss} = -\frac{1}{3}(\nabla \cdot \vec{v}(r))\, p, \tag{4.11}$$

for momentum loss due to adiabatic expansion.

4.2 Energy gain

Consider a blob moving along the AGN jet. In the rest frame of the blob the ambient matter (proton, electrons and charged dust) moves with a relativistic velocity towards the blob. A two stream instability is formed when blob and ambient matter collide, which causes the captured electrons and protons to isotropize rapidly. Alfvénic turbulences are generated by incident protons, electrons and dust. Electrons within the blob are accelerated by stochastic gyro-resonant acceleration with

turbulences generated by the isotropization of captured protons and charged dust, while protons are accelerated stochastically by dust induced turbulences [55].
It has to be mentioned that the particle density of the ambient matter n_a has to be much smaller than the particle density of the blob, which will be shown in section 5.1.4. Otherwise the generated low-frequency waves will be modified by the captured particles.
Thus, momentum gain and momentum diffusion coefficient are fixed by:

$$\dot{p}_\mathrm{gain} = \frac{v_\mathrm{s}^2}{4\,D_x} p^2 \tag{4.12}$$

$$D_\mathrm{pp} = \frac{v_\mathrm{A}^2}{9 D_x} p^2. \tag{4.13}$$

Here, v_s gives the shock velocity, v_A gives the Alfvén velocity and D_x gives the spatial diffusion coefficient.
Since the turbulent spectrum is assumed to be $\propto k^2$, T_esc is momentum independent [55], and the transport equation can be solved analytically.

4.3 Solution of the transport equation

Consider that the particle phase momentum distribution $f(p)$ and the flux are linked via

$$\phi_\mathrm{p}(E_\mathrm{p}) = \frac{\mathrm{d}N}{\mathrm{d}p\,\mathrm{d}V} = 4\pi\, f(p)^2. \tag{4.14}$$

The transport equation will be solved for $f(p)$ and by applying equation (4.31) the proton flux is fixed

$$-Q(p) = \frac{1}{p^2}\frac{\partial}{\partial p}\left[p^2 D_{pp}\frac{\partial f(p)}{\partial p}\right] - \frac{1}{p^2}\frac{\partial}{\partial p}\left[p^2\left(\dot{p}_\mathrm{gain} + \dot{p}_\mathrm{loss}\right) f(p)\right] - \frac{f(p)}{T_\mathrm{esc}}. \tag{4.15}$$

Considering momentum loss equation (4.6) and equation (4.11), and momentum gain equation (4.12) one obtains after some algebraic transformation:

$$-Q(p) = \underbrace{bp^2}_{g_0(p)} f''(p) + \underbrace{(4b-d)p}_{g_1(p)} f'(p) + \underbrace{(-3d - \frac{1}{T_{\text{esc}}})}_{g_2(p)} f(p) \tag{4.16}$$

$$b = \frac{v_A^2}{9D_x} \tag{4.17}$$

$$d = \frac{v_s^2}{4D_x} - \frac{1}{3}\nabla\vec{v} - a. \tag{4.18}$$

Multiplying equation (4.15) by $\frac{1}{g_0(p)} \exp\left(\int^p \frac{g_1(p')}{g_0(p')} \mathrm{d}p'\right)$ it is transformed into a Sturm-Liouville differential equation, which can be solved easily:

$$\begin{aligned} -\frac{Q(p)}{g_0(p)} \exp\left(\int^p \frac{g_1(p')}{g_0(p')} \mathrm{d}p'\right) = \frac{\mathrm{d}}{\mathrm{d}p}\left[\exp\left(\int^p \frac{g_1(p')}{g_0(p')} \mathrm{d}p'\right) \frac{\partial f(p)}{\partial p}\right] + \\ + \frac{g_3(p)}{g_0(p)} \exp\left(\int^p \frac{g_1(p')}{g_0(p')} \mathrm{d}p'\right) f(p) \end{aligned} \tag{4.19}$$

$$-M(p) = \frac{\mathrm{d}}{\mathrm{d}p}\left[H(p)\frac{\partial f(p)}{\partial p}\right] + Y(p)f(p) \tag{4.20}$$

$$H(p) = \exp\left[\int^p (4b-d)\frac{1}{bp'}\mathrm{d}p'\right] = p^{4-\epsilon} \text{ with } \epsilon = \frac{d}{b} \tag{4.21}$$

$$Y(p) = -\left(3\epsilon + \frac{1}{T_{\text{esc}} \cdot b}\right) p^{2-\epsilon} \tag{4.22}$$

$$M(p) = \frac{Q(p)}{bp^2} p^{4-\epsilon}. \tag{4.23}$$

The main focus is on loss dominated processes, meaning $\epsilon < 0$. Considering equation (4.21) and equation (4.22) one obtains:

$$\frac{\partial^2 f(p)}{\partial p^2} + \left(\frac{4-\epsilon}{p}\right)\frac{\partial f(p)}{\partial p} + \left(-3\epsilon - \frac{1}{T_{\text{esc}} \cdot b}\right)\frac{f(p)}{p^2} = -\frac{1}{bp^2}\delta(p-p_0). \tag{4.24}$$

The homogeneous solution of equation (4.24) is a Cauchy-Euler differential equation and solved by:

$$f_{\text{hom}}(p) = A\, p^{\frac{1}{2}(\epsilon-3)+\sqrt{\Delta}} + B\, p^{\frac{1}{2}(\epsilon-3)-\sqrt{\Delta}} \tag{4.25}$$

$$\Delta := \frac{1}{4}(3-\epsilon)^2 + (3\epsilon + \frac{1}{T_{\text{esc}}\, b}). \tag{4.26}$$

The inhomogeneous differential equation can be solved by introducing the Green's function $G(p, p_0)$:

$$G(p, p_0) = \begin{cases} A(p_0)\, p^{\frac{1}{2}(\epsilon-3)+\sqrt{\Delta}} & \text{for } p < p_0 \\ B(p_0) p^{\frac{1}{2}(\epsilon-3)-\sqrt{\Delta}} & \text{for } p > p_0. \end{cases} \tag{4.27}$$

Demanding that $G(p, p_0)$ is continuous at p_0

$$A(p_0) p_0^{\frac{1}{2}(\epsilon-3)+\sqrt{\Delta}} = B(p_0) p_0^{\frac{1}{2}(\epsilon-3)-\sqrt{\Delta}}, \tag{4.28}$$

and requiring that the derivation at p_0 is discontinuous

$$\frac{\mathrm{d}}{\mathrm{d}p} B(p_0) p^{\frac{1}{2}(\epsilon-3)-\sqrt{\Delta}}\Big|_{p_0} - \frac{\mathrm{d}}{\mathrm{d}p} A(p_0) p^{\frac{1}{2}(\epsilon-3)+\sqrt{\Delta}}\Big|_{p_0} = -\frac{1}{H(p_0)}, \tag{4.29}$$

the coefficients $A(p_0)$ and $B(p_o)$ are determined. The focus is on the high energy regime, i.e. $p > p_0$:

$$f(p) = \frac{1}{2\sqrt{\Delta}} p_0^{\frac{1}{2}(\epsilon+5)+\sqrt{\Delta}} p^{\frac{1}{2}(\epsilon-3)-\sqrt{\Delta}}. \tag{4.30}$$

Considering the relativistic energy impulse relation ($E = p \cdot c$) for extremely energetic protons, equation (4.31) and that protons are accelerated up to the energy E_0 given by the GZK cut off, the proton flux is:

$$\phi(E_\mathrm{p}) = \frac{8\,\pi^2 R^2}{\sqrt{\frac{1}{4}(3-\epsilon)^2 + (3\epsilon + \frac{1}{T_\mathrm{esc}\, b})}} E_0^{\frac{1}{2}(\epsilon+5)+\sqrt{\Delta}}\, c^{-(3+\epsilon)}\, E_\mathrm{p}^{\frac{1}{2}(\epsilon+1)-\sqrt{\Delta}} \exp\left(-\frac{E_\mathrm{p}}{E_0}\right). \tag{4.31}$$

It has to be mentioned, that the solution of the equation is given in the blob frame and thus has to be transformed in to the observer's frame. For FR-I and FR-II transformation effects cancels out, which will be explained in detail in section 5.1.5. For Blazars boosting effect play an important role and have to be considered. As can be seen the proton flux is a function of several parameters, which in turn are a combination of basic physics parameters. The determination of these parameters or functions is very complex or almost impossible, since the only tool we have are electromagnetic observations of AGN. The exact plasma conditions within the blob are mainly unknown.

Observational properties like the ratio of electrons to protons can be used to constrain these parameters. In order to compare with these observational quantities,

the proton flux can be described as a power-law function with normalization A_p and spectral index s, having a cutoff at $E_\mathrm{p} = E_0$. These parameters are described by the previously introduced ones.

$$A_\mathrm{p} = \frac{8\,\pi^2 R^2}{\sqrt{\Delta}} E_0^{\frac{1}{2}(\epsilon+5)+\sqrt{\Delta}}\, c^{-(3+\epsilon)} \tag{4.32}$$

$$s = \frac{1}{2}(\epsilon+1) - \sqrt{\Delta} \tag{4.33}$$

$$\phi(E_\mathrm{p}) = A_\mathrm{p} E_\mathrm{p}^{-s} \exp\left(-\frac{E_\mathrm{p}}{E_0}\right). \tag{4.34}$$

Having calculated the proton flux, the neutrino rate within the blob, the neutrino flux at Earth can be computed, by applying analytical and semi analytical methods.

Chapter 5

Analytical and semi-analytical calculation of neutrino flux for AGN

The detection of highly energetic neutrinos (PeV energy range) with the combined IC 79/IC 86 IceCube neutrino detector [24] gives rise to the question in which astrophysical sources, and under which conditions these neutrinos are produced.
Considering the maximum neutrino energy $E_\nu^{\max} \approx \frac{1}{20} E_{\mathrm{p}}^{\max}$ galactic sources can be ruled out with a high degree of certainty, as they are believed not to fulfill physical conditions, i.e. lack of strong magnetic fields B in combination with large acceleration regions R, to accelerate CRs to energies, needed to explain the observed energies [9]. Observations of high-energy γ-rays from extragalactic sources, AGN and GRBs, led to focus on these objects as possible sources of high-energy neutrinos.
The observed γ-rays are assumed to be produced among others by synchrotron cooling of relativistic electrons moving through magnetic fields, by inverse Compton scattering or by inelastic proton-proton $(p-p)$ interaction, leading to production of charged and neutral pions, where neutral pions decay in two γ-rays. Neutrinos can be produced either way, by proton-gamma $(p-\gamma)$ or by inelastic $p-p$ interactions.
Concerning photo-hadronic emission scenarios, a primary source of uncertainty comes from the composition of CRs. For a large fraction of heavy nuclei, the neutrino flux is significantly reduced with respect to a pure proton flux. In addition, the spectral shape of the neutrino spectrum from photo-hadronic interactions is

highly sensitive to the shape and bandwidth of the target photon field [56]. The main effect comes from the fact that a delta resonance must to be produced. This is a threshold effect depending on the bandwidth of the magnetic field. For moderate boost factors, relatively high-energy photon fields are needed in order to lower the spectral break to below the IceCube bandwidth of the detected signal: The IceCube observed bandwidth reaches larger than $\sim$ PeV neutrino energy, which corresponds to a proton energy of $E_\mathrm{p} > 20$ PeV. Thus, in order to have a flat spectrum, i.e. close to E^{-2}, a photon field with a significant contribution at an energy E_γ needs to be present with the condition

$$E_\mathrm{p}\, E_\mathrm{ph} = \frac{(m_\Delta^2 - m_\mathrm{p}^2)c^4}{2\,(1-\cos(\phi))}\,\frac{\Gamma_\mathrm{B}}{(1+z)}. \tag{5.1}$$

The collision angle is ϕ, the proton energy, at Earth is given in the observer's frame, and is therefore boosted with the Lorentz factor Γ_B of the production region [56]. Considering that the break needs to be at $E_\mathrm{p} < 20$ PeV in order to have a spectrum close to E^{-2} in the IceCube bandwidth, the photon field at the source needs to have a significant contribution at above $E_\gamma \approx 40\,(\Gamma_\mathrm{B}/10)\,(2/(1+z))$ eV [56]. Here, conservative values for the average boost factor and redshift have been assumed. It is therefore very difficult to receive an E^{-2}-type neutrino spectrum from photo-hadronic interactions in the relevant energy range. Furthermore, the photon field seen from the blob is highly anisotropic. These anisotropies have large influences on the threshold energy, equation (5.1). For interactions taking place at a distance d from the black hole, ϕ scales as $\phi \sim d/R_\mathrm{disk}$, with R_disk giving the emission size of the photon field. Consequently, larger proton energies are required [57].

Thus, only extreme high energetic protons can produce pions. Consequently, the $p\gamma$ mechanism is in comparison to inelastic $p-p$ interaction less efficient. Additionally the number of free parameters is higher, which are provided with large uncertainties, and thus making predictions difficult. Therefore, we only consider inelastic $p-p$ interactions as possible neutrino source in radio galaxies and Blazars.

5.1 Analytical approach

For many practical applications, simple approximations can be used. Numerical approaches like SIBYLL, QGSJet, EPOS or DPMJet provide much more detailed

and up to date particle physics in comparison to analytical methods. Nevertheless uncertainties by using analytical approximations are rather small compared to astrophysical uncertainties, which will be discussed later. The simplest approximation is based on the delta function representation of the generated pion power $P_{\pi^0,\pi^\pm}(E_\pi, E_\mathrm{p})$. It will be assumed that generated pions have a mean Lorentz factor, given in equation (4.2). Thus, it is:

$$P_{\pi^0,\pi^\pm}(E_\pi, E_\mathrm{p}) = 1.3\, R\, n_\mathrm{H}\, \gamma_\pi\, \epsilon(E_\mathrm{p}) \sigma_{\mathrm{pp}}(E_\mathrm{p}) \delta(\gamma_\pi - \overline{\gamma}_\pi). \tag{5.2}$$

The pion rate at the source is [58]:

$$Q_{\pi^\pm}(E_\pi, E_\mathrm{p}) = \frac{1.26}{E_\pi} \int_1^\infty \mathrm{d}E_\mathrm{p}\, \phi_\mathrm{p}(E_\mathrm{p}) P_{\pi^0,\pi^\pm}(E_\pi, E_{\mathrm{p}}) \tag{5.3}$$

$$Q_{\pi^\pm}(E_\pi) = \frac{1.26}{E_\pi} \int_1^\infty \mathrm{d}E_\mathrm{p}\, \phi_\mathrm{p}(E_\mathrm{p}) 1.3\, R\, n_\mathrm{H}\, \gamma_\pi\, \epsilon(E_\mathrm{p})\, \sigma_{\mathrm{pp}}(E_\mathrm{p}) \delta(\gamma_\pi - \gamma_\mathrm{p}^{3/4}) \tag{5.4}$$

$$= 1.64\, R\, n_\mathrm{H}\, \frac{\gamma_\pi}{E_\pi} \int_1^\infty \mathrm{d}E_\mathrm{p}\, \sigma_{\mathrm{pp}}(E_\mathrm{p}) \phi_\mathrm{p}(E_\mathrm{p})\, \epsilon(E_\mathrm{p}) \delta\left(\frac{1}{m_\pi\, c^2} \cdot (E_\pi - \overline{E}_\pi)\right) \tag{5.5}$$

$$= 1.64\, R\, n_\mathrm{H} \int_1^\infty \mathrm{d}E_\mathrm{p}\, \sigma_{\mathrm{pp}}(E_\mathrm{p}) \phi_\mathrm{p}(E_\mathrm{p}) \epsilon(E_\mathrm{p}) \delta\left(E_\pi - \overline{E}_\pi\right). \tag{5.6}$$

For the observed energy range the cross-section can be assumed to be constant [53], which simplifies the calculation

$$Q_{\pi^\pm}(E_\pi) = 1.64\, R\, n_\mathrm{H}\, \sigma_{\mathrm{pp}} \int_1^\infty \mathrm{d}E_\mathrm{p}\, \phi_\mathrm{p}(E_\mathrm{p}) \epsilon(E_\mathrm{p}) \delta\left(E_\pi - \overline{E}_\pi\right). \tag{5.7}$$

Taking results for pion multiplicity from equation (4.4), and for the mean pion energy from equation (4.2), and considering our results for the proton spectrum, it is

$$Q_{\pi^\pm}(E_\pi) = 1.64\, R\, n_\mathrm{H}\, \sigma_{\mathrm{pp}} \int_1^\infty \mathrm{d}E_\mathrm{p}\, E_\mathrm{p}^{-s} \exp\left(-\frac{E_\mathrm{p}}{E_0}\right) 2\, E_\mathrm{p}^{1/4}\, \delta\left(E_\pi - \frac{1}{6} E_\mathrm{p}^{3/4}\right). \tag{5.8}$$

Substitution $z = \frac{1}{6}\, E_{\mathrm{p}}^{3/4}$ GeV is used for the integration to give the pion rate within the blob:

$$Q_{\pi^{\pm}}\,(E_{\pi}) = 26.2\, A_{\mathrm{p}}\, R\, n_{\mathrm{H}}\, \sigma_{\mathrm{pp}}\, (6\, E_{\pi})^{-\alpha} \exp\left(-\frac{(6\, E_{\pi})^{\frac{4}{3}}}{E_0}\right) \tag{5.9}$$

$$\alpha = \frac{4}{3}\left(s - \frac{1}{2}\right). \tag{5.10}$$

For $s = 2$ the proton and the neutrino spectral index are equal. To obtain the total neutrino production rate at the source one must sum the first muon neutrino which is produced directly from the pion, the second muon neutrino and the electron neutrino which are produced in the muon decay. The link between pion and neutrino spectra can be explained by assuming that the total energy of the pions is distributed equally among the four produced particles [56]

$$Q_{\nu_i}(E_{\nu_i}) = Q_{\pi}(4\, E_{\nu_i})\frac{\mathrm{d}E_{\pi}}{\mathrm{d}E_{\nu_i}} = 4\, Q_{\pi}(4E_{\nu_i}) \tag{5.11}$$

for each neutrino, $\nu_i = \overline{\nu}_{\mathrm{e}}, \nu_{\mathrm{e}}, \nu_{\mu}, \overline{\nu}_{\mu}$. Since IceCube cannot distinguish between particle and its anti particle, the distinction will be not be made in the following. To calculate the neutrino rate from the pion rate, it is assumed that the number of a single neutrino flavor produced in the infinitesimally small energy bin $\mathrm{d}E_{\nu}$ comes from the original pion in the energy bin $\mathrm{d}E_{\pi} = 4\,\mathrm{d}E_{\nu}$ and use that one neutrino of a fixed flavor is produced in the final state of the pion decay, $Q_{\nu}(E_{\nu})\mathrm{d}E_{\nu} = Q_{\pi}(4\, E_{\nu})\mathrm{d}E_{\pi}$.
Thus, the total neutrino rate at the source is given by

$$Q_{\nu,\,\mathrm{tot}}(E_{\nu}) \approx 314\, N_{\mathrm{H}}\, A_{\mathrm{p}}\, \sigma_{\mathrm{pp}} \left(\frac{24 \cdot E_{\nu}}{\mathrm{GeV}}\right)^{-\alpha}. \tag{5.12}$$

Consider that density n_{H} and R are substituted by the column density $N_{\mathrm{H}} = R \cdot n_{\mathrm{H}}$. The analytical approach represents a reasonable method of particle-physical processes with only smaller deviations when using full representations of energy dependent cross-section and full energy distributions for secondaries. Results of semi analytical methods will be discussed in the next sections.
Thus, equation (5.12) provides an accurate estimation of the total neutrino rate at the source, and consequently gives good estimates of the neutrino flux at Earth. Assuming that IceCube data can be explained with this model, the spectral index in the calculation must to be compatible with the measured one: $2.0 \leq \alpha_{\mathrm{IceCube}} \leq 2.46$ [28].

The cross-section is a particle-physical property which is measured and parameterized for the observed energy range [53]. The column density N_{H} is one of the main free parameters. In this model it is assumed that a certain sub-class of the AGN explains the IceCube signal. The CR normalization A_{p} the second, relatively free parameter, will be fixed by considering radio observations of AGN.
The radio luminosity L_{radio} provides a measure for the AGN luminosity in electrons. The electron luminosity is equal to or larger than the radio luminosity of the source, as the latter is produced when electrons are accelerated and emit synchrotron radiation:

$$L_{\mathrm{e}} = \chi(s, B) L_{\mathrm{radio}}. \tag{5.13}$$

Here, s gives the spectral index of the electron population and B the magnetic field.
Furthermore, hadronic CRs and electrons are linked via the constant fraction:

$$g_e = \frac{L_e}{L_{\mathrm{p}}} \tag{5.14}$$

Accordingly, the proton and radio luminosity are connected via:

$$L_{\mathrm{p}} = \frac{\chi(s, B)}{g_{\mathrm{e}}} L_{\mathrm{radio}}. \tag{5.15}$$

Due to the assumption of $\propto k^2$ for the turbulent spectrum, the CR spectral index s is energy independent, and A_{p} can be fixed analytically:

$$\int_{E_{\mathrm{p}}} \mathrm{d}E_{\mathrm{p}}\, E_{\mathrm{p}}\, \phi(E_{\mathrm{p}}) = L_{\mathrm{p}} \tag{5.16}$$

$$A_{\mathrm{p}} = \frac{\chi(s, B)}{g_{\mathrm{e}}} L_{\mathrm{radio}} \left[\int_{E_{\mathrm{p}}} \mathrm{d}E_{\mathrm{p}}\, E_{\mathrm{p}}^{1-s} \exp\left(-\frac{E_{\mathrm{p}}}{E_0}\right) \right]^{-1} \tag{5.17}$$

Depending on the CR spectral index s, the integral in equation (5.17) is solved by the incomplete Gamma function ($s \neq 2$) or by the exponential integral ($s = 2$). Consequently, A_{p} is:

$$A_{\mathrm{p}} = \frac{\chi(s, B)}{g_{\mathrm{e}}} L_{\mathrm{radio}} \begin{cases} \left[\frac{1}{2-s} \left(E_0^{2-\alpha}\, \Gamma_{\mathrm{B}}\left(3 - s, \frac{E_{\mathrm{min}}}{E_0}\right) - E_{\mathrm{min}}^{2-s} \exp\left(-\frac{E_{\mathrm{min}}}{E_0}\right) \right) \right]^{-1} & s \neq 2 \\ \left[-\mathrm{Ei}\left(\frac{E_{\mathrm{min}}}{E_0}\right) \right]^{-1} & s = 2. \end{cases} \tag{5.18}$$

Considering equation (5.12), the cross-section σ_{pp} is given and α is limited by the IceCube measurement. The CR normalization A_{p} as a function of $\chi(s, B)$ and g_e is calculated.

5.1.1 Calculation of g_{e}

CR observations show that for same particle energies there are about 100 times more protons than electrons [52]. To have a theoretical explanation for this ratio, it will be assumed that electrons and protons have same the spectral index s same power-law spectrum for the differential number density in momentum p:

$$N_{\mathrm{e}} = N_{0,\mathrm{e}}\, p^{-s} \tag{5.19}$$

$$N_{\mathrm{p}} = N_{0,\mathrm{p}}\, p^{-s}. \tag{5.20}$$

Furthermore, it will be assumed that they have an equal total number density:

$$n_0 = \int_{T_0}^{\infty} \mathrm{d}E_{\mathrm{kin}} N_{\mathrm{e}}(E_{\mathrm{kin}}) = \int_{T_0}^{\infty} \mathrm{d}E_{\mathrm{kin}} N_{\mathrm{p}}(E_{\mathrm{kin}}) \tag{5.21}$$

$$E_{\mathrm{kin}} = \sqrt{p^2c^2 + m_{\mathrm{e,p}}^2 c^4} - m_{\mathrm{e,p}} c^2. \tag{5.22}$$

Thus, considering equation (5.22) the differential number density in units of E_{kin} is [58]:

$$N_{\mathrm{e,p}}(E_{\mathrm{kin}}) = N\left[p(E_{\mathrm{kin}})\right] \frac{\mathrm{d}p}{\mathrm{d}E_{\mathrm{kin}}} = \frac{N_{0,\mathrm{e\ p}}}{c^2}\left(E_{\mathrm{kin}} + m_{\mathrm{e,p}}c^2\right)\left[\left(\frac{E_{\mathrm{kin}}}{c}\right)^2 + 2E_{\mathrm{kin}} m_{\mathrm{e,p}}\right]. \tag{5.23}$$

Inserting equation (5.23) in equation (5.21) and integrating gives [52]

$$N_{0,\mathrm{e}} = (s-1) n_0 \left(\frac{T_0^2}{c^2} + 2T_0 m_{\mathrm{e}}\right)^{\frac{s-1}{2}} \tag{5.24}$$

$$N_{0,\mathrm{p}} = (s-1) n_0 \left(\frac{T_0^2}{c^2} + 2T_0 m_{\mathrm{p}}\right)^{\frac{s-1}{2}}, \tag{5.25}$$

resulting in

$$\frac{N_{0,\mathrm{e}}}{N_{0,\mathrm{p}}} = \frac{\left(\frac{T_0^2}{c^2} + 2T_0 m_\mathrm{e}\right)^{\frac{s-1}{2}}}{\left(\frac{T_0^2}{c^2} + 2T_0 m_\mathrm{p}\right)^{\frac{s-1}{2}}} \approx \left(\frac{m_\mathrm{e}}{m_\mathrm{p}}\right)^{\frac{s-1}{2}}. \tag{5.26}$$

Consequently, considering equation (5.23) and equation (5.26) the electron to proton ratio g_e is fixed:

$$g_\mathrm{e} = \frac{N_\mathrm{e}(E_\mathrm{kin})}{N_\mathrm{p}(E_\mathrm{kin})} = \frac{N_{0,\mathrm{e}}}{N_{0,\mathrm{p}}} \frac{(E_\mathrm{kin} + m_\mathrm{e}c^2)\left[\left(\frac{E_\mathrm{kin}}{c}\right)^2 + 2E_\mathrm{kin}m_\mathrm{e}\right]^{-\frac{(s+1)}{2}}}{(E_\mathrm{kin} + m_\mathrm{p}c^2)\left[\left(\frac{E_\mathrm{kin}}{c}\right)^2 + 2E_\mathrm{kin}m_\mathrm{p}\right]^{-\frac{(s+1)}{2}}} \tag{5.27}$$

$$= \left(\frac{m_\mathrm{e}}{m_\mathrm{p}}\right)^{\frac{s-1}{2}} \frac{(E_\mathrm{kin} + m_\mathrm{e}c^2)\left[\left(\frac{E_\mathrm{kin}}{c}\right)^2 + 2E_\mathrm{kin}m_\mathrm{e}\right]^{-\frac{(s+1)}{2}}}{(E_\mathrm{kin} + m_\mathrm{p}c^2)\left[\left(\frac{E_\mathrm{kin}}{c}\right)^2 + 2E_\mathrm{kin}m_\mathrm{p}\right]^{-\frac{(s+1)}{2}}} \tag{5.28}$$

For relativistic energies, $E_\mathrm{kin} \gg m_\mathrm{p}\, c^2$, g_e approaches a constant value

$$g_\mathrm{e} \approx \left(\frac{m_\mathrm{e}}{m_\mathrm{p}}\right)^{\frac{s-1}{2}} \approx 0.02 \text{ for} s = 2. \tag{5.29}$$

However, assuming equal spectral indices for protons and electrons is difficult to justify due to different energy loss processes. Both spectral indices, s_e and s_p, depend on several parameters which are difficult to measure. Detailed calculations of g_e for different spectral index can be found in [59]. Thus, to reduce the number of parameters and uncertainties and to fix g_e CRs and radio observations are used. Assuming that AGN are the sources of ultra high energetic CRs, g_e can be estimated empirically by comparing the average measured energy density rate, $\dot{\rho}_\mathrm{CR}$ (units: MeV/(Mpc^3 s)) and $\dot{\rho}_\mathrm{radio}$. $\dot{\rho}_\mathrm{CR}$ is received by integrating over the observed CR spectrum from $E_\mathrm{p}^\mathrm{min} \approx 10^{18}$ eV, see section 2.3:

$$\dot{\rho}_\mathrm{CR} = \frac{H_0}{c}\left(\int_{10^{18}\mathrm{eV}}^{10^{20}\mathrm{eV}} \phi_\mathrm{p}(E_\mathrm{p})\, E_\mathrm{p}\, \mathrm{d}E_\mathrm{p}\right) \tag{5.30}$$

$$= \frac{H_0}{c}\left(\int_{10^{18}\mathrm{eV}}^{10^{20}\mathrm{eV}} \mathrm{d}E_\mathrm{p}\, \phi_0\, E_\mathrm{p}^{-s}\left[1 + \exp\left(\frac{\log(E_\mathrm{p}) - \log(E_\mathrm{B})}{\log(W)}\right)\right]^{-1}\right) \tag{5.31}$$

$$\approx 4.3 \cdot 10^{42}\, \frac{\mathrm{MeV}}{\mathrm{Mpc}^3\mathrm{s}}. \tag{5.32}$$

in the regime](dashed) To calculate the radio energy density rate $\dot{\rho}_\mathrm{e}$ for AGN, the RLF for radio galaxies and Blazars introduced in section 3.7 is used. Thus, $\dot{\rho}_\mathrm{e}$ is obtained by integrating the radio luminosity function:

$$\dot{\rho}_\mathrm{e} = \frac{1}{\ln 10} \int_L F_\mathrm{radio}(L, z)\, \mathrm{d}L\, \mathrm{d}z \tag{5.33}$$

$$\dot{\rho}_\mathrm{e} \approx \begin{cases} 4.4 \cdot 10^{40}\, \frac{\mathrm{MeV}}{\mathrm{Mpc^3 s}} & \text{for FR-I} \\ 1.7 \cdot 10^{42}\, \frac{\mathrm{MeV}}{\mathrm{Mpc^3 s}} & \text{for FR-II} \\ 9 \cdot 10^{40}\, \frac{\mathrm{MeV}}{\mathrm{Mpc^3 s}} & \text{for Blazars.} \end{cases} \tag{5.34}$$

Having calculated $\dot{\rho}_\mathrm{CR}$ and $\dot{\rho}_\mathrm{e}$, g_e is fixed by:

$$g_\mathrm{e} = \frac{\dot{\rho}_\mathrm{radio}}{\dot{\rho}_{\ \mathrm{CR}}} \approx \begin{cases} 0.01 & \text{for FR-I} \\ 0.4 & \text{for FR-II} \\ 0.02 & \text{for Blazars.} \end{cases} \tag{5.35}$$

As can be seen the result for g_e is in the range of theoretical considerations. cosmic GRBs, we While both theoretical and experimental constraints bear uncertainties, they end up in approximately the same range and do not allow completely arbitrary values.
As it is extremely difficult to pinpoint the exact value, we start by using $g_\mathrm{e} = 10^{-1.2}$, so that a symmetric uncertainty $\Delta g_\mathrm{e} \approx 10^{\pm 0.8}$ is obtained. Thus, a higher value of g_e leads to a density increase.

5.1.2 Calculation of $\chi(s, B)$

Relativistic electrons within the blob lose energy due to different loss processes and radiate their energy over a wide energy range. To calculate the electron luminosity L_e it will be assumed that $\chi(s, B) = \dot{\rho}_\mathrm{e}(s)/\dot{\rho}_\mathrm{radio}(s, B)$ giving the ratio between total electron $\dot{\rho}_\mathrm{e}$ and radio $\dot{\rho}_\mathrm{radio}$ emissivity is equal for electron and radio luminosity, which is reasonable due to energy conservation:

$$\chi(s, B) = \frac{L_\mathrm{e}}{L_\mathrm{radio}} = \frac{\dot{\rho}_\mathrm{e}}{\dot{\rho}_\mathrm{radio}(s, B)} \tag{5.36}$$

$$\rho_e = \int_{E_\mathrm{min}}^{E_\mathrm{max}} \frac{\mathrm{d}N_\mathrm{e}}{\mathrm{d}E\, \mathrm{d}t}\, E\, \mathrm{d}E \tag{5.37}$$

$$\dot{\rho}_e = C_0 \int_{E_\mathrm{min}}^{E_\mathrm{max}} \mathrm{d}E\, E^{1-s} = C_0 \begin{cases} \ln\left(\frac{E_\mathrm{max}}{E_\mathrm{min}}\right) & \text{for } s = 2 \\ \frac{E_\mathrm{max}^{2-s} - E_\mathrm{min}^{2-s}}{2-s} & \text{for } s \neq 2. \end{cases} \tag{5.38}$$

The radio energy emissivity ρ_{radio} is calculated by integrating the emission coefficient j_ν over the radio band between $\nu_{\text{min}} = 100$ MHz and $\nu_{\text{max}} = 5$ GHz [56]:

$$\dot{\rho}_{\text{radio}} = \int_{\nu_{\text{max}}}^{\nu_{\text{min}}} \mathrm{d}\nu \, j_\nu \tag{5.39}$$

$$j_\nu = \frac{1}{4\pi} \int_{\gamma_{\text{min}}}^{\gamma_{\text{max}}} \mathrm{d}\gamma \, \frac{\mathrm{d}N_{\text{e}}}{\mathrm{d}\gamma} P_{\text{sync}}(\nu, \gamma) \tag{5.40}$$

$$P_{\text{sync}}(\nu, \gamma) = P_0(B) \left(\frac{\nu}{\nu_0 \gamma^2} \right)^{\frac{1}{3}} H\left[\nu_0 \gamma^2 - \nu\right] \tag{5.41}$$

$$\frac{\mathrm{d}N_{\text{e}}}{\mathrm{d}\gamma} = \tau_0 C_0 \left(m_{\text{e}} c^2\right)^{1-s} \gamma^{-1-s}. \tag{5.42}$$

$P_{\text{sync}}(\nu, \gamma)$ gives the radiated power of a single electron, $P_0(B)$ the normalization and the Heaviside step function $H[\nu_0 \gamma^2 - \nu]$ considers the spectral cut-off. The electron spectrum is given by $\mathrm{d}N_{\text{e}}/\mathrm{d}\gamma$. The characteristic synchrotron radiation frequency $\nu_0 = 4.2 \cdot 10^6 \, (B/1\,G)$ gives the frequency where a single electron loses most of its synchrotron energy. Since the main focus is on the radio energy range the normalization $P(B)$ must be recalculated for the observed frequency range:

$$P_0(B) \int_0^\infty \mathrm{d}\nu \left(\frac{\nu}{\nu_0 \gamma^2} \right) \exp\left(-\frac{\nu}{\nu_0 \gamma^2} \right) = P_1(B) \int_0^{\nu_0 \gamma^2} \mathrm{d}\nu \left(\frac{\nu}{\nu_0 \gamma^2} \right) \tag{5.43}$$

$$P_1(B) = \frac{4}{3} P_0(B) \int_0^\infty \mathrm{d}x \, x^{\frac{1}{3}} \exp(-x) \tag{5.44}$$

$$= \frac{4}{3} P_0(B) \Gamma_{\text{B}} \left(\frac{4}{3} \right). \tag{5.45}$$

Consequently, the emission coefficient is:

$$j_\nu = \frac{(m_{\text{e}} c^2)^{1-s}}{4\pi} \tau_0 C_0 P_0(B) \left(\frac{\nu}{\nu_0} \right)^{\frac{1}{3}} \int_{\gamma_{\text{min}}}^{\gamma_{\text{max}}} \mathrm{d}\gamma \, \gamma^{-\frac{5}{3}-s} H\left[\nu_0 \gamma^2 - \nu\right] \tag{5.46}$$

$$= \beta \int_{\gamma_{\text{min}}}^{\gamma_{\text{max}}} \mathrm{d}\gamma \, \gamma^{-\frac{5}{3}-s} H\left[\nu_0 \gamma^2 - \nu\right] \tag{5.47}$$

$$\beta = \frac{(m_{\text{e}} c^2)^{1-s}}{4\pi} \tau_0 C_0 P_1(B) \left(\frac{\nu}{\nu_0} \right)^{\frac{1}{3}}. \tag{5.48}$$

Due to the Heaviside step function, equation (5.46) can be divided into two ranges:

$$\int_{\gamma_{\text{min}}}^{\gamma_{\text{max}}} \mathrm{d}\gamma \, H\left[\gamma - \sqrt{\frac{\nu}{\nu_0}}\right] \gamma^{-\frac{5}{3}-s} = \frac{\beta}{\frac{2}{3}+s} \left\{ \left[\left(\sqrt{\frac{\nu}{\nu_0}} \right)^{-\frac{2}{3}-s} - \gamma_{\text{max}}^{-\frac{2}{3}-s} \right] H\left[\sqrt{\frac{\nu}{\nu_0}} - \gamma_{\text{min}}\right] \right.$$
$$\left. + \left[\gamma_{\text{min}}^{-\frac{2}{3}-s} - \gamma_{\text{max}}^{-\frac{2}{3}-s} \right] H\left[\gamma_{\text{min}} - \sqrt{\frac{\nu}{\nu_0}}\right] \right\}. \tag{5.49}$$

Equation (5.49) can be used to determine the radio energy emissivity $\dot{\rho}_{\text{radio}}$, by applying the results on equation (5.39).

Consequently, for $\gamma_{\rm min}^2\nu_0 > \nu$ the radio energy emissivity is given by:

$$\dot{\rho}_{\rm radio} = \frac{3}{4}\tilde{\beta}\left(\gamma_{\rm min}^{-\frac{2}{3}-s} - \gamma_{\rm max}^{-\frac{2}{3}-s}\right) H\left[\gamma_{\rm min}^2\nu_0 - \nu_{\rm min}\right]\left\{H\left[\nu_{\rm max} - \gamma_{\rm min}^2\nu_0\right]\cdot \right.$$
$$\left.\cdot\left((\nu_0\gamma_{\rm min}^2)^{\frac{4}{3}} - \nu_{\rm min}^{\frac{4}{3}}\right) + H\left[\gamma_{\rm min}^2\nu_0 - \nu_{\rm max}\right]\left(\nu_{\rm max}^{\frac{4}{3}} - \nu_{\rm min}^{\frac{4}{3}}\right)\right\}. \tag{5.50}$$

For $\gamma_{\rm min}^2\nu_0 < \nu$ the radio energy emissivity is:

$$\dot{\rho}_{\rm radio} = \tilde{\beta}H\left[\nu_{\rm max} - \gamma_{\rm min}\nu_0^2\right]\left\{\left(a\left(\nu_{\rm max}^{1-\frac{s}{2}} - \nu_{\rm min}^{1-\frac{s}{2}}\right) - b\left(\nu_{\rm max}^{\frac{4}{3}} - \nu_{\rm min}^{\frac{4}{3}}\right)\right) H\left[\nu_{\rm min} - \gamma_{\rm min}\nu_0^2\right]\right.$$
$$\left.\left(a\left(\nu_{\rm max}^{1-\frac{s}{2}} - (\gamma_{\rm min}^2\nu_0)^{1-\frac{s}{2}}\right) - b\left(\nu_{\rm max}^{\frac{4}{3}} - (\gamma_{\rm min}^2\nu_0)^{\frac{4}{3}}\right)\right) H\left[\gamma_{\rm min}\nu_0^2 - \nu_{\rm min}\right]\right\} \tag{5.51}$$

$$\tilde{\beta} = \frac{(m_e c^2)^{1-s}}{4\pi(\frac{2}{3}+s)}\tau_0 C_0 P_1(B)\nu_0^{-\frac{1}{3}} \tag{5.52}$$

$$a = \frac{\left(\sqrt{\frac{1}{\nu_0}}\right)^{-\frac{2}{3}-s}}{1-\frac{s}{2}} \tag{5.53}$$

$$b = \frac{3}{4}\gamma_{\rm max}^{-\frac{2}{3}-s}. \tag{5.54}$$

Hence $\chi(s,B) = \dot{\rho}_{\rm e}(s)/\dot{\rho}_{\rm radio}(s,B)$ can be expressed by:

$$\chi = \epsilon\cdot\left(E_{\rm max}^{2-s} - E_{\rm min}^{2-s}\right)\begin{cases}\left[(a\cdot\xi) - (b\cdot\zeta)\right]^{-1} & \nu_0\gamma_{\rm min}^2 < \nu_{\rm min}\\ \left[(a\cdot\tilde{\xi}) - (b\cdot\tilde{\zeta}) + \vartheta\right]^{-1} & \nu_{\rm min} \le \nu_0\gamma_{\rm min}^2 \le \nu_{\rm max}\\ \left[\tilde{\vartheta}\right]^{-1} & \nu_0\gamma_{\rm min}^2 > \nu_{\rm max}\end{cases} \tag{5.55}$$

$$\epsilon = \frac{4\pi}{(m_e c^2)^{1-s}}\frac{s+\frac{2}{3}}{2-s}\frac{\nu_0^{\frac{1}{3}}}{\tau_0 P_1(B)} \tag{5.56}$$

$$\xi = \left(\nu_{\rm max}^{1-\frac{s}{2}} - \nu_{\rm min}^{1-\frac{s}{2}}\right) \tag{5.57}$$

$$\tilde{\xi} = \left(\nu_{\rm max}^{1-\frac{s}{2}} - (\nu_0\gamma_{\rm min})^{1-\frac{s}{2}}\right) \tag{5.58}$$

$$\zeta = \left(\nu_{\rm max}^{\frac{4}{3}} - \nu_{\rm min}^{\frac{4}{3}}\right) \tag{5.59}$$

$$\tilde{\zeta} = \left(\nu_{\rm max}^{\frac{4}{3}} - (\nu_0\gamma_{\rm min}^2)^{\frac{4}{3}}\right) \tag{5.60}$$

$$\vartheta = \frac{3}{4}\left(\gamma_{\rm min}^{-\frac{2}{3}-s} - \gamma_{\rm max}^{-\frac{2}{3}-s}\right)\left((\nu_0\gamma_{\rm min}^2)^{\frac{4}{3}} - \nu_{\rm min}^{\frac{4}{3}}\right) \tag{5.61}$$

$$\tilde{\vartheta} = \frac{3}{4}\left(\gamma_{\rm max}^{-\frac{2}{3}-s} - \gamma_{\rm min}^{-\frac{2}{3}-s}\right)\left(\nu_{\rm max}^{\frac{4}{3}} - \nu_{\rm min}^{\frac{4}{3}}\right). \tag{5.62}$$

In Figure 5.1 $\chi(s,B)$ as a function of the magnetic field B for different electron spectral indices s is shown. The maximum Lorentz factor $\gamma_{\rm max}$ and the minimum Lorentz factor $\gamma_{\rm min}$ are fixed. The minimum Lorentz factor is fixed to be in the range of $\gamma_{\rm min} = 1 - 10$. The maximum energy reached by electrons limit $\gamma_{\rm max}$ to be in the range $\gamma_{\rm max} = 10^{10\pm1}$ in order to explain the observed CR energy. The uncertainty of γ for electrons produce an uncertainty factor of about $\Delta\chi \approx 10^{\pm0.2}$. The choice of the minimum Lorentz factor determines at which critical magnetic field $B_{\rm c}$ the parameter $\chi(s,B)$ changes from being constant to increasing with a power-law.
Increasing the spectral index for fixed magnetic fields B leads to a lower value for $\chi(s,B)$. This can be explained by the following manner:
The electron spectrum $\frac{{\rm d}N_{\rm e}}{{\rm d}\gamma} \propto \gamma^{-s}$ falls rapidly for higher energies and for higher s. The main

part of the energy output will be located in the radio range, while the higher energy output will be a minor part. Therefore, $\dot{\rho}_{\rm radio}$ increases, and consequently $\chi(s, B)$ decreases.

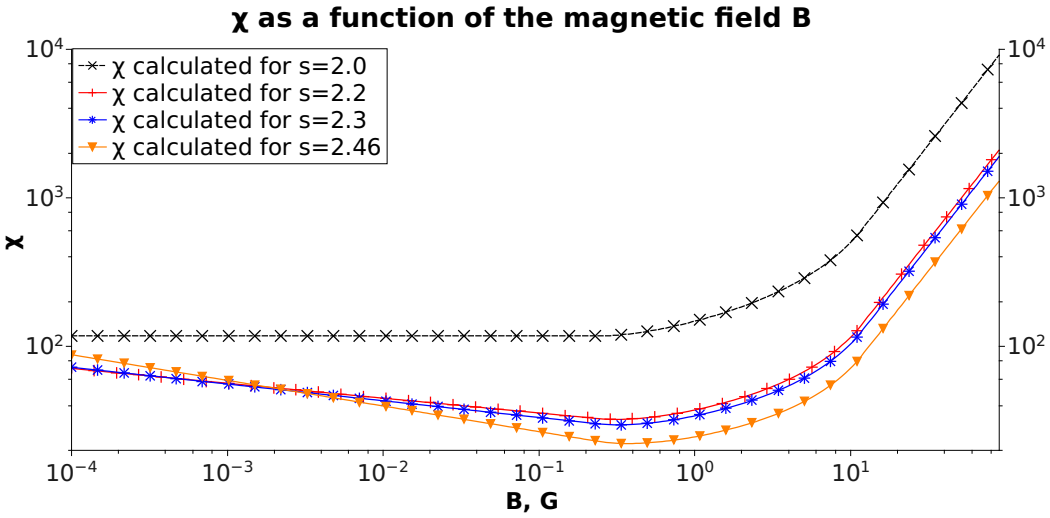

FIGURE 5.1: $\chi(s, B)$ as a function of the magnetic field B for different spectral index s. The black (diagonal cross) line gives χ for $s = 2$, the red (cross) line for $s = 2.2$, the blue (star) line for $s = 2.3$ and the orange (triangle down) line for $s = 2.46$. The maximum Lorentz factor is $\gamma_{\rm max} = 10^{10}$, and the minimum Lorentz factor is $\gamma_{\rm min} = 10$.

5.1.3 Flux calculation

Having calculated the electron to proton ratio $g_{\rm e}$, the radio to electron luminosity ratio $\chi(s, B)$, and the CR normalization $A_{\rm p}$, the number of free parameters in equation (5.12) is reduced to one, the column density $N_{\rm H}$ which will be fixed by the recent IceCube detection.

Assuming that the detected neutrinos are produced within relativistic moving blobs, leaving their point of origin isotropically, and considering adiabatic energy losses, $E_\nu = E_{\nu,0} \cdot (1 + z)$, with E_ν as the neutrino energy at the source and $E_{\nu,0}$ the energy at the detector, the flux of a single AGN blob at Earth is:

$$\phi_\nu(E_{\nu,0}) = \varsigma_{\rm osc.} \frac{Q_\nu(E_\nu)}{4\pi d_L(z)^2} \tag{5.63}$$

$$= \frac{\chi(s, B)}{g_{\rm e}} \frac{314}{24^\alpha} N_{\rm H} \sigma_{\rm pp} \left[\int_{E_{\rm p}} E_{\rm p}^{1-s} \exp\left(-\frac{E_{\rm p}}{E_0}\right) \right]^{-1} \frac{L_{\rm radio}}{4\pi d_L(z)^2} \left(\frac{E_\nu}{\rm GeV}\right)^{-\alpha} \tag{5.64}$$

$$= \Psi\, N_{\rm H} \frac{L_{\rm radio}}{4\pi d_L(z)^2} \left(\frac{E_\nu}{\rm GeV}\right)^{-\alpha} \tag{5.65}$$

$$\Psi = \frac{\chi(s, B)}{g_{\rm e}} \frac{314}{24^\alpha} \sigma_{\rm pp}\, a_{\rm p} \tag{5.66}$$

$$a_{\rm p} = \left[\int_{E_{\rm p}} E_{\rm p}^{1-s} \exp\left(-\frac{E_{\rm p}}{E_0}\right) \right]^{-1}. \tag{5.67}$$

Here, ς considers neutrino oscillation. At the source neutrinos are generated with the flavor ratio

$$\left(v_e^{\text{source}}, v_\mu^{\text{source}}, v_\tau^{\text{source}}\right) = (1, 2, 0). \tag{5.68}$$

On their way to the detector neutrinos oscillate. Due to the large distances a stable equilibrium is set up

$$\left(v_e^{\text{source}}, v_\mu^{\text{source}}, v_\tau^{\text{source}}\right) = (1, 1, 1), \tag{5.69}$$

leading to $\varsigma = 1/3$. To compare our calculated flux with the detected diffuse flux, the diffuse neutrino flux will be computed, by convolving the flux of a single point source, equation (5.63) with the number of contributing AGN at a given redshift z and radio luminosity L_{radio}:

$$\phi_\nu(E_{\nu,0}) = \varsigma \frac{1}{\ln(10)} \Psi\, N_{\text{H}} \left(\frac{E_\nu}{\text{GeV}}\right)^{-\alpha} \int_{L,z} \frac{1}{4\pi d_L(z)^2} F_{\text{radio}}(L, z)\, \mathrm{d}L\, \frac{\mathrm{d}V_c}{\mathrm{d}z}\, \mathrm{d}z. \tag{5.70}$$

Considering equation (5.70) all parameters except N_{H} are fixed. Consequently, it is

$$\phi_{\text{IceCube}}(E_\nu) = \phi_\nu(E_{\nu,0}), \tag{5.71}$$

with $\phi_{\text{IceCube}}(E_\nu)$ giving the observed and $\phi_\nu(E_{\nu,0})$ the calculated flux. First observations of 28 high energy neutrinos between May 2010 and May 2012 [24] indicate a best-fit E_ν^{-2} with

$$\phi_{\text{IceCube}}(E_\nu) = 1.2 \cdot 10^{-8}\, E_\nu^{-2} \qquad \frac{1}{\text{GeV}\,\text{cm}^2\,\text{s}\,\text{sr}} \tag{5.72}$$

Taking into account more statistics, new constraints on the neutrino flux of the previously flux (equation (5.72)) is given by

$$\phi_{\text{IceCube}}(E_\nu) = \phi_0\, E_\nu^{-\alpha} \tag{5.73}$$

$$= 2.06^{+0.4}_{-0.3}\, 10^{-6.5} E_\nu^{-2.3} \qquad \frac{1}{\text{GeV}\,\text{cm}^2\,\text{s}\,\text{sr}} \tag{5.74}$$

$$= 2.06^{+0.4}_{-0.3}\, 10^{-5.7} E_\nu^{-2.46} \qquad \frac{1}{\text{GeV}\,\text{cm}^2\,\text{s}\,\text{sr}}. \tag{5.75}$$

Hence, the column density is:

$$N_{\text{H}} = \phi_{\text{IceCube}}(E_\nu) E_\nu^\alpha \frac{\ln(10)}{\varsigma} \frac{g_e}{\chi(s, B)\sigma_{\text{pp}}} \frac{24^\alpha}{a_{\text{p}}} \left[\int_{L,z} \frac{1}{4\pi d_L(z)^2} F_{\text{radio}}(L, z)\, \mathrm{d}L\, \frac{\mathrm{d}V_c}{\mathrm{d}z}\, \mathrm{d}z\right]^{-1}. \tag{5.76}$$

For FR-I and FR-II galaxies, considering the current cosmological models for the Universe, the spectral index dependent column density N_{H} is:

$$N_{\text{H}}^{\text{FR-I}} = \phi_{\text{IceCube}}(E_\nu)\, E_\nu^\alpha \frac{24^\alpha}{a_{\text{p}}} \frac{g_{\text{e}}}{\chi(s, B)} \frac{10^{33}}{6.3} \tag{5.77}$$

$$N_{\text{H}}^{\text{FR-II}} = \phi_{\text{IceCube}}(E_\nu)\, E_\nu^\alpha \frac{24^\alpha}{a_{\text{p}}} \frac{g_{\text{e}}}{\chi(s, B)} \frac{10^{33}}{3.18}. \tag{5.78}$$

An important contribution is the normalization of the observed flux, ϕ_0. The more statistic used to give better constraints on the flux, the more precise the normalization, and thus the more

precise are the results for N_{H}.
Furthermore, the accuracy of the parameters a_{p}, g_e and $\chi(s, B)$ depends on the quality of flux observations. Consequently, the more precise observations and statistics are, the more precise the values. As can be seen, increasing the magnetic field B leads to lower values for N_{H}, since $N_{\mathrm{H}} \propto \chi(s, B)^{-1}$, equation (5.77) and (5.78).

-	$\alpha = 2.0; \chi = 100$	$\alpha = 2.3; \chi = 30$	$\alpha = 2.46; \chi = 26$
$N_{\mathrm{H}}^{\text{FR-I}}$ in cm^{-2}	$\approx 6.4 \cdot 10^{24}$	$\approx 7.4 \cdot 10^{24}$	$\approx 4.1 \cdot 10^{24}$
$N_{\mathrm{H}}^{\text{FR-II}}$ in cm^{-2}	$\approx 1.1 \cdot 10^{25}$	$\approx 1.3 \cdot 10^{25}$	$\approx 8.2 \cdot 10^{24}$

TABLE 5.1: Column densities for FR galaxies, for different neutrino spectral index α and $\chi(s, B)$. The value for χ is obtained by taking the average in the range of $B = 10^{-4} - 10$ G.

Differences in densities for FR-I and FR-II (table 5.1) can be explained by the radio luminosity function $F_{\mathrm{radio}}(L, z)$, giving the number of galaxies per radio luminosity and per co-moving volume V_{c}.
FR-II galaxies have higher radio luminosities but are outnumbered in comparison to FR-I galaxies. This leads to lower integrated luminosities, and consequently in higher column densities as can be seen in equation (5.78).
Differences within the sub-class can be explained by giving the ratio of the densities

$$\frac{N_{\mathrm{H},\alpha=2.0}}{N_{\mathrm{H},\alpha=2.3}} = \frac{\phi^0_{\mathrm{IceCube},\alpha=2.0}}{\phi^0_{\mathrm{IceCube},\alpha=2.3}} \frac{24^2}{24^{2.3}} \frac{a_{\mathrm{p},\alpha=2.3}}{a_{\mathrm{p},\alpha=2.0}} \frac{\chi(2.3)}{\chi(2.0)} \tag{5.79}$$

$$\approx 0.86 \tag{5.80}$$

$$\frac{N_{\mathrm{H},\alpha=2.0}}{N_{\mathrm{H},\alpha=2.46}} \approx 1.5 \tag{5.81}$$

$$\frac{N_{\mathrm{H},\alpha=2.3}}{N_{\mathrm{H},\alpha=2.46}} \approx 1.8, \tag{5.82}$$

which are the same for FR-I as well as for FR-II as the contribution of the radio luminosity function cancels out. These differences can be explained by the normalization of the detected neutrino flux $\phi^0_{\mathrm{IceCube},\alpha}$ as well as by the s dependent parameter a_{p} and $\chi(s, B)$.
In Figure (5.2a) and (5.2c) calculated diffuse neutrino fluxes for FR-I and FR-II are shown. Figure (5.2b) and (5.2d) illustrate column densities for FR-I and FR-II. As expected N_{H} remains constant up to a critical magnetic field $B_c \approx 10$ G. For higher magnetic fields $\chi(s, B)$ increases and N_{H} decreases due to the $N_{\mathrm{H}} \propto \chi(s, B)^{-1}$ dependence.
The radio luminosity L_{radio} used to calculate the neutrino flux originates from the knots in FR-I galaxies and from the lobes in FR-II galaxies. Consequently, we compare our results with column densities within knots and lobes. For particle densities n_{H} within the knot we adopt $n_{\mathrm{H}} \approx 10^9\,\mathrm{cm}^{-3}$, and for the knot size $R \approx 10^{15}$cm, close to the foot of the jet. With increasing distance from the foot of the jet z, the density decreases, while the knot size increases due to adiabatic expansion. Therefore the column densities remains constant $N_{\mathrm{H}} = n_{\mathrm{H}} \cdot R \approx 10^{24}\,\mathrm{cm}^{-2}$. Assuming $B(z) \propto z^{-1}$ the most important contribution is expected to come from the foot of

the jet, if typical magnetic fields $B = 0.1 - 10$ G are assumed. These considerations result in a possible parameter range for FR-I galaxies

$$(N_{\mathrm{H}}, B) = (10^{24\pm1}\,\mathrm{cm}^{-2}, 10^{0.5\pm0.5}\,\mathrm{G}\ ), \tag{5.83}$$

making FR-I galaxies serious candidates for the production of high energetic neutrinos, as can be seen in Figure 5.2b.

Figure 5.2d shows column densities for FR-II galaxies. According to our model the size of the moving blob increases further, while the particle density reduces among others due to catastrophic losses, particle escape from the blob. Assuming a lobe size of $R \approx 10^{22} - 10^{23}$cm and a target density of $n_{\mathrm{H}} = 0.01 - 0.1\,\mathrm{cm}^{-3}$ the column density for expected magnetic fields [60] is in the parameter range

$$(N_{\mathrm{H}}, B) = (10^{21\pm1}\,\mathrm{cm}^{-2}, 10^{4\pm1}\,\mathrm{G}). \tag{5.84}$$

Consequently, it is below the calculated densities, and inelastic $p-p$ interactions can be excluded in all probability as possible sources of the detected neutrino signal.

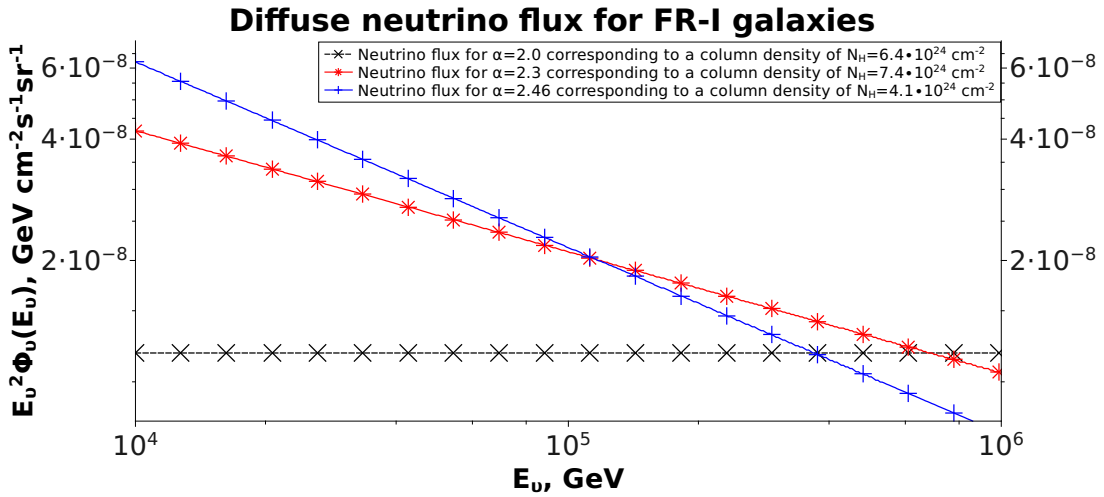

(A) Calculated diffuse neutrino flux for FR-I galaxies, for the energy range taken from [28]. The parameter g_e is fixed to $g_e = 0.06$ and $\chi(s, B)$ is obtained by taking the average in the range of $B = 10^{-4} - 10$ G, see Table 5.1. The column density is fixed by using the recent IceCube measurement [24],[28]. The (black) diagonal cross line gives the flux for $\alpha = 2.0$, the (red) star for $\alpha = 2.3$ and (blue) cross for $\alpha = 2.46$.

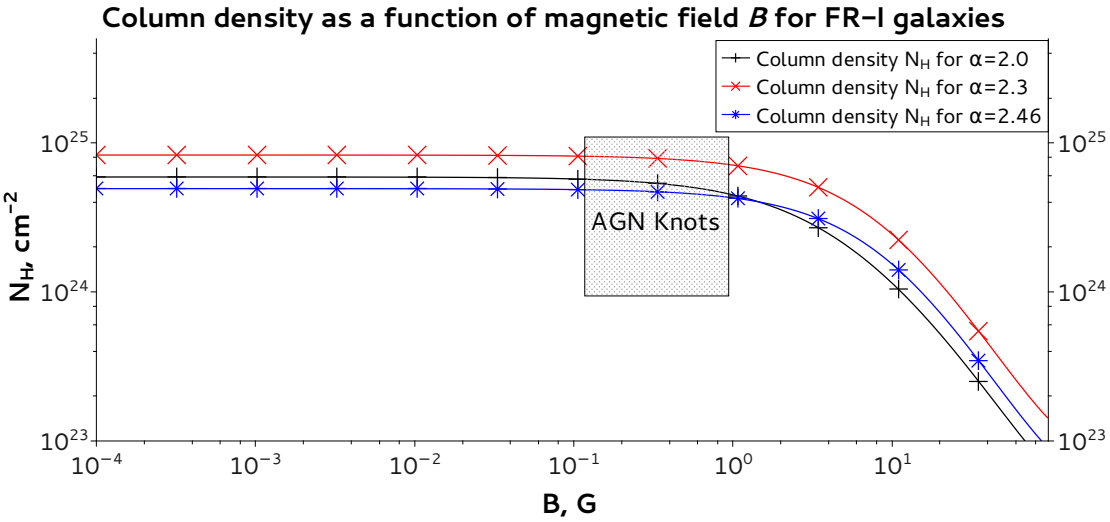

(B) Column density N_{H} as a function of magnetic field B for FR-I galaxies. For increasing magnetic field, N_{H} decreases. The (black) cross line gives the density for $\alpha = 2.0$, the (red) diagonal cross for $\alpha = 2.3$ and (blue) star for $\alpha = 2.46$. The rectangle gives the regions derived including uncertainties in the calculation, dominated by $\chi(s, B)$ and g_e.

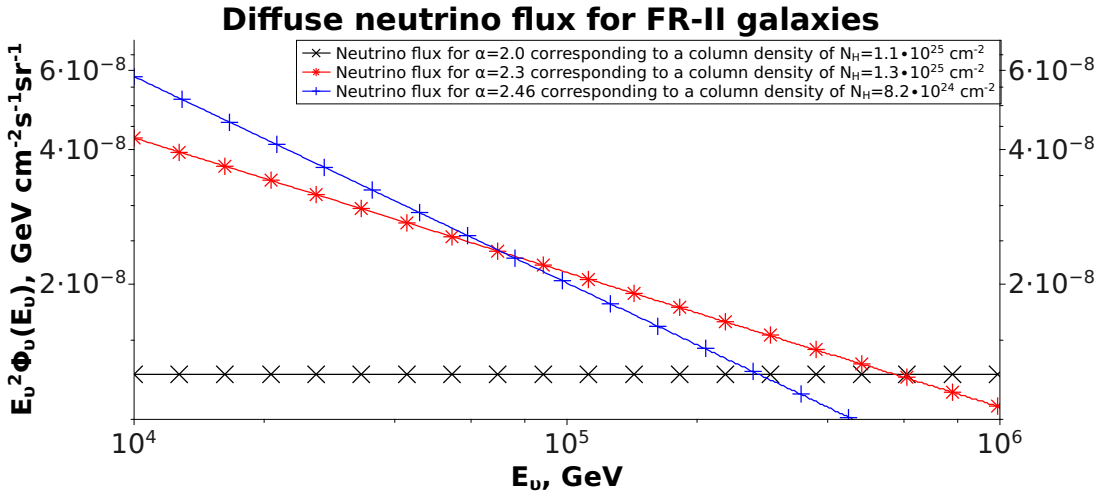

(C) Calculated diffuse neutrino flux for FR-II galaxies, for the energy range taken from [28]. The parameter g_e is fixed to $g_e = 0.06$ and $\chi(s, B)$ is obtained by taking the average in the range of $B = 10^{-4} - 10$ G, see Table 5.1. The column density is fixed by using the recent IceCube measurement.The (black) diagonal cross line gives the flux for $\alpha = 2.0$, the (red) star for $\alpha = 2.3$ and (blue) cross for $\alpha = 2.46$.

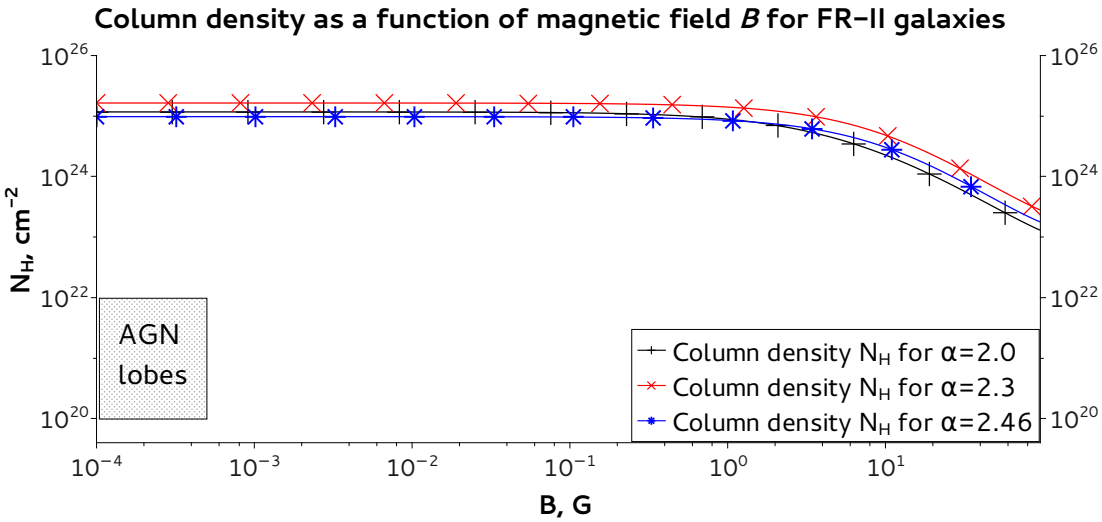

(D) Column density N_{H} as a function of magnetic field B for FR-II galaxies. For increasing magnetic field, N_{H} decreases. The (black) cross line gives the density for $\alpha = 2.0$, the (red) diagonal cross for $\alpha = 2.3$ and (blue) star for $\alpha = 2.46$. The rectangle gives the regions derived including uncertainties in the calculation, dominated by $\chi(s, B)$ and g_e.

FIGURE 5.2: Calculated neutrino flux and column densities for FR-I and FR-II galaxies, using the delta functional approximation. For the calculation of the densities current IceCube measurements from [24],[28] are used.

It is noteworthy that this model only includes $p-p$ interactions, and does not take into account photo-hadronic interaction. In general $p-\gamma$ interactions can contribute to a possible signal in the lobes. As very high energetic photons are needed in the lobes, but the dominant electromagnetic emission is coming from the radio range, neutrino production due to photo-hadronic interaction seems to be very unlikely [56]

5.1.4 Density of the ambient matter

To verify whether the used ansatz, see section 4.2 is convenient to calculate column densities and fluxes, the particle density within the blob n_{H} and the particle density of the ambient matter n_{a} must fulfill the condition

$$n_{\mathrm{a}} \ll n_{\mathrm{H}}. \tag{5.85}$$

In [61] n_{a} is calculated for several FR-I galaxies, which is in the range

$$n_{\mathrm{a}} = (10 - 10^3)\,\mathrm{cm}^{-3}, \tag{5.86}$$

which is comparing with $n_{\mathrm{H}}^{\text{FR-I}} = 10^9\,\mathrm{cm}^{-3}$, much smaller. These results are obtained by assuming that g_e can vary in the range

$$g_e = 0.1 - 0.01, \tag{5.87}$$

and that $\chi(s, B)$ is fixed

$$\chi(s, B) = 1. \tag{5.88}$$

Consequently, these results give upper limits for the ambient density, and thus fulfill the condition $n_{\mathrm{a}} \ll n_{\mathrm{H}}$.
For FR-II sources the mean density $\overline{n}_{\mathrm{H}}$ is calculated in [62] for the same values for g_e and $\chi(s, B)$:

$$n_{\mathrm{a}} < 2\,\mathrm{cm}^{-3}, \tag{5.89}$$

which is also in agreement with the condition. Consequently, our calculated column densities N_{H}, blob densities n_{H} and ambient densities n_{a} fulfill the condition required in section 4.2.

5.1.5 Neutrino flux and column density for Blazars

To calculate the neutrino flux for Blazars, not only the radio luminosity function for Blazars, but also boosting effects, which are negligible for radio galaxies have to be considered. For radio galaxies the Lorentz boost factor Γ_{B}, measured in the observer's frame, is small while the inclination angle i is large, resulting in small Doppler factors, $\delta \approx 1$. For Blazars Γ_{B} is large while i is small resulting in $\delta \gg 1$. The radio luminosity function used in equation (5.70) is

measured in the observer's frame. Thus, the additional factor based on the transformation of the luminosity from the observer's frame to the source frame cancels out, due to the inverse transformation of the flux from the blob to the observer. Effects of area transformation also cancel out, since we transform the radio luminosity per steradian to a luminosity by multiplying by an opening angle of 4π and then divide by the same factor to account for the fraction of neutrinos that reaches Earth. Both factors scale with the boost factor in the same way.
The remaining factor, influenced by Doppler boosting is the neutrino energy. Since we first calculate the neutrino rate at the source but measure the energy on Earth, the energy will be transformed [63]. Thus, the flux for Blazars is given by

$$\phi_\nu^{\mathrm{IceCube}}(E_\nu) = \frac{\varsigma}{\ln(10)} \Psi \cdot N_{\mathrm{H}} \frac{\chi}{g_{\mathrm{e}}} \left(\frac{E_\nu}{\mathrm{GeV}}\right)^{-\alpha} \delta^\alpha \int_L \int_z \frac{1}{4\pi d_L(z)^2} F_{\mathrm{radio}}(L,z) \mathrm{d}L \frac{\mathrm{d}V_{\mathrm{c}}}{\mathrm{d}z} \mathrm{d}z, \tag{5.90}$$

and the column density N_{H} by

$$N_{\mathrm{H}}^{\mathrm{Blazar}} = \underbrace{\frac{24^\alpha}{a_{\mathrm{p}}} \frac{g_{\mathrm{e}}}{\chi(s,B)} \frac{10^{33}}{1.2}}_{\mathrm{const}(\alpha,s,B)} \phi_{\mathrm{IceCube}}\left(E_\nu\right) E_\nu^\alpha \delta^{-\alpha}. \tag{5.91}$$

Comparing equation (5.77)and (5.78) with equation (5.91) clarifies that the main difference in the column densities is due boosting effects. For small Γ_{B} and large i equation (5.91) changes and gives appropriate densities for radio galaxies:

$$N_{\mathrm{H}} = \mathrm{const}(\alpha,s,B)\, \phi^{\mathrm{IceCube}}(E_\nu) E_\nu^\alpha\, \delta^{-\alpha} \tag{5.92}$$

$$= \mathrm{const}(\alpha,s,B)\, \phi^{\mathrm{IceCube}}\left(E_\nu\right) E_\nu^\alpha \cdot \underbrace{\Gamma_{\mathrm{B}}^\alpha}_{\approx 1} \left(1 - \underbrace{\beta \cos(i)}_{\to 0}\right)^\alpha \tag{5.93}$$

$$\approx N_{\mathrm{H}}^{\mathrm{radio}} \tag{5.94}$$

For relatively small Γ_{B} and $i = 0°$, N_{H} is in the range of radio galaxies. Increasing Γ_{B} and i leads to higher column densities, which is explained by equation (5.93). Increasing i leads to lower $\beta\cos(i)$, and thus $1 - \beta\cos(i)$ converges to one. Consequently, N_{H} is a function of Γ_{B}:

$$N_{\mathrm{H}} \approx \mathrm{const}\left(\alpha,s,B\right) \phi^{\ \mathrm{IceCube}}(E_\nu)^\alpha\, \Gamma_{\mathrm{B}}^\alpha. \tag{5.95}$$

On the other hand, reducing i leads to higher $\beta\cos(i)$ which is one for $i = 0°$. Thus, N_{H} decreases:

$$N_{\mathrm{H}} = \mathrm{const}(\alpha,s,B)\, \phi^{\mathrm{IceCube}}(E_\nu)^\alpha\, \Gamma_{\mathrm{B}}^\alpha\, (1-\beta)^\alpha \tag{5.96}$$

$$= \mathrm{const}(\alpha,s,B) \phi^{\mathrm{IceCube}}(E_\nu)^\alpha\ , \Gamma_{\mathrm{B}}^\alpha \left(1 - \sqrt{1 - \frac{1}{\Gamma_{\mathrm{B}}^2}}\right)^\alpha \tag{5.97}$$

$$= \mathrm{const}(\alpha,s,B) \phi^{\mathrm{IceCube}}(E_\nu)^\alpha \left(\Gamma_{\mathrm{B}} - \sqrt{\Gamma_{\mathrm{B}}^2 - 1}\right)^\alpha. \tag{5.98}$$

Differences for different α can be among others reduced to the Doppler factor. For $\Gamma_{\rm B} = 10$ and $i = 0°$, the fraction of the densities are:

$$\frac{N_{\rm H,\alpha=2.0}}{N_{\rm H,\alpha=2.3}} = \frac{\phi^0_{\rm IceCube,\alpha=2.0}}{\phi^0_{\rm IceCube,\alpha=2.3}} \frac{24^2}{24^{2.3}} \frac{\delta^{2.3}}{\delta^{2.0}} \frac{a_{\rm p,\alpha=2.3}}{a_{\rm p,\alpha=2.0}} \frac{\chi(2.3)}{\chi(2.0)} \tag{5.99}$$

$$\approx 1.5 \tag{5.100}$$

$$\frac{N_{\rm H,\alpha=2.0}}{N_{\rm H,\alpha=2.46}} \approx 4 \tag{5.101}$$

$$\frac{N_{\rm H,\alpha=2.3}}{N_{\rm H,\alpha=2.46}} \approx 2.7. \tag{5.102}$$

In Figure (5.3a) and (5.3b) neutrino fluxes for Blazars with different values for $\Gamma_{\rm B}$ and i are shown. Figures (5.3c)-(5.3f) illustrate column densities for different spectral index α and different $\Gamma_{\rm B}$ and i. The shaded box is fixed in the following way:
Equation (5.91) gives the averaged column density of all contributing Blazars considered by $F^{\rm Blazar}_{\rm radio}(L, z)$. Thus, it is expected that Blazar point sources have column densities which are in the range of the calculated ones. Consequently, observations of point sources can be used to give constraints on the Lorentz factor $\Gamma_{\rm B}$ and inclination angle i.
Fermi *LAT* observations of 23 Blazars give a limit for $N_{\rm H}$ to be in the range [64]

$$N_{\rm H} = \left(10^{20} - 10^{22}\right) {\rm cm}^{-2}. \tag{5.103}$$

Models used to fit $\gamma-$ray observations for Flat Spectrum Radio Quasars (FSRQs) predict a range of [65]

$$N_{\rm H} = \left(10^{22} - 10^{24}\right) {\rm cm}^{-2}. \tag{5.104}$$

For the magnetic field B a range of [66]

$$B = \left(10^{-3} - 10\right) {\rm G} \tag{5.105}$$

will be adopted. Thus, combining results from equation (5.103), (5.104) and (5.105) limit the range and fix the shaded box.

$$N_{\rm H} = \left(10^{20} - 10^{24}\right) {\rm cm}^{-2}. \tag{5.106}$$

Comparing the results with combined densities equation (5.106) show that Blazars with Lorentz factors $\Gamma_{\rm B} = 10 - 100$ and inclination angle $i = 0°$ are within the shaded box, and thus are potential candidates to be sources of high-energy CRs.
To have an estimate of the blob size and compare with our predictions we make use of γ-ray variability, observed for the high-energy end of the γ-ray flux for Blazars. The causality relation

$$R < c\, t_{\rm var}\, \delta (1 + z)^{-1}, \tag{5.107}$$

with $t_{\rm var}$ giving the variability time scale, δ the Doppler boost, c speed of light and z the redshift sets an upper limit for the blob size.

Adopting our values which we used to calculate fluxes and column densities, $z_{\max} = 10$ and observed time variabilities of one day, the emission region is in the range of $10^{14} \leq R \leq 10^{16}$cm for $10 \leq \Gamma_{\mathrm{B}} \leq 100$, which is in agreement with the predicted blob size of radio galaxies [67].
In Figure 5.4a, 5.4c and 5.4e N_{H} as a function of inclination angle i for each considered neutrino spectral index α is shown. Increasing i leads to a increase in N_{H}, reaching a maximum value of $N_{\mathrm{H}}^{\max} \approx 10^{28}\,\mathrm{cm}^{-2}$ for $\Gamma_{\mathrm{B}} = 20$. Such high values are inconsistent with the main assumption of low optical depth:

$$\tau_{\mathrm{pp}} = \sigma_{\mathrm{pp}}\, R\, n_{\mathrm{H}} = 10. \tag{5.108}$$

Furthermore, it is assumed that the blob density is limited by $n_{\mathrm{H}}^{\max} \approx 10^{9} - 10^{10}\,\mathrm{cm}^{-3}$. Such high column densities disagree with this assumption. The same behavior is found if N_{H} is plotted as a function of Γ_{B}, see Figure 5.4b, 5.4d and 5.4f.
Thus, only for $i = 0°$ and $10 < \Gamma_{\mathrm{B}} < 100$ physical relevant results are obtained.

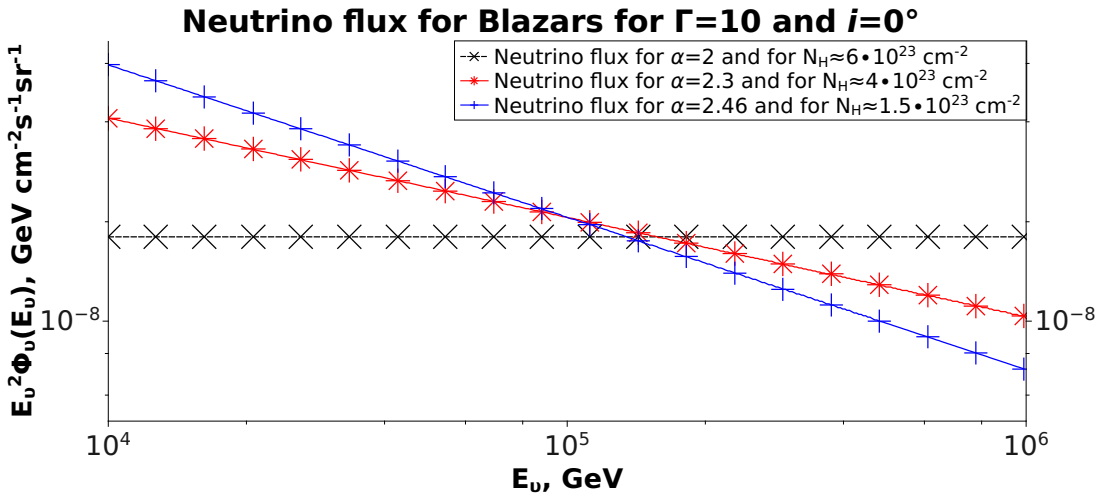

(A) Diffuse neutrino flux calculated for Blazars, for fixed g_e and fixed $\chi(s, B)$ (Table 5.1), for Lorentz factor $\Gamma_B = 10$ and inclination angle $i = 0°$. The (black) diagonal cross line gives the flux for $\alpha = 2.0$, the (red) star cross for $\alpha = 2.3$ and (blue) cross for $\alpha = 2.46$.

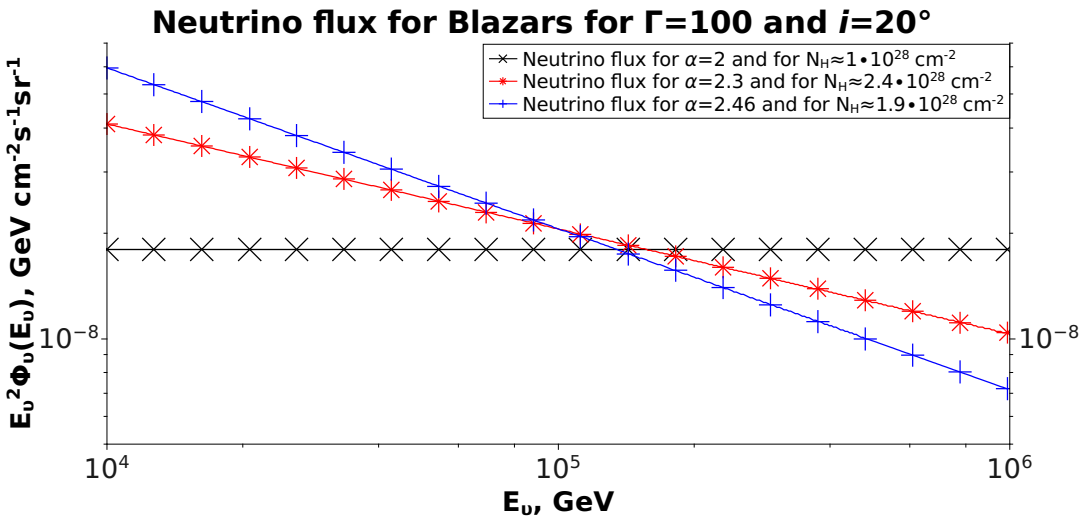

(B) Diffuse neutrino flux calculated for Blazars, for fixed g_e and fixed $\chi(s, B)$ (Table 5.1), for Lorentz factor $\Gamma_B = 100$ and inclination angle $i = 20°$.The (black) diagonal cross line gives the flux for $\alpha = 2.0$, the (red) star cross for $\alpha = 2.3$ and (blue) cross for $\alpha = 2.46$.

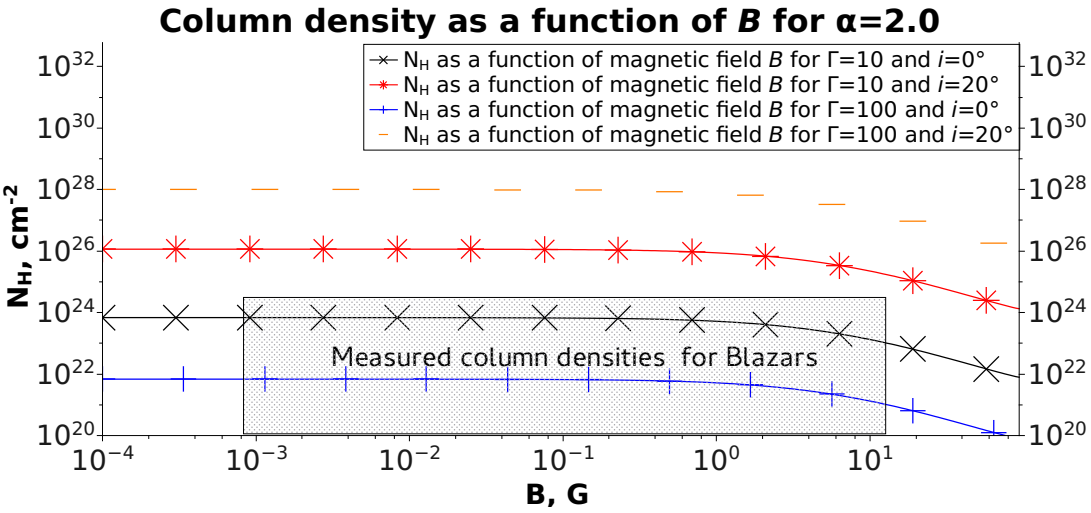

(C) Column density as a function of magnetic field B for different $\Gamma_{\rm B}$ and i, for $\alpha = 2.0$. The shaded area gives the densities from [64] and [65]. The (blue) crossed line gives $N_{\rm H}$ for $\Gamma_{\rm B} = 100$; $i = 0°$, the (black) diagonal crossed line for $\Gamma_{\rm B} = 10$; $i = 0°$, the (red) star line for $\Gamma_{\rm B} = 10$; $i = 20°$ and the (orange) for $\Gamma_{\rm B} = 100$; $i = 20°$.

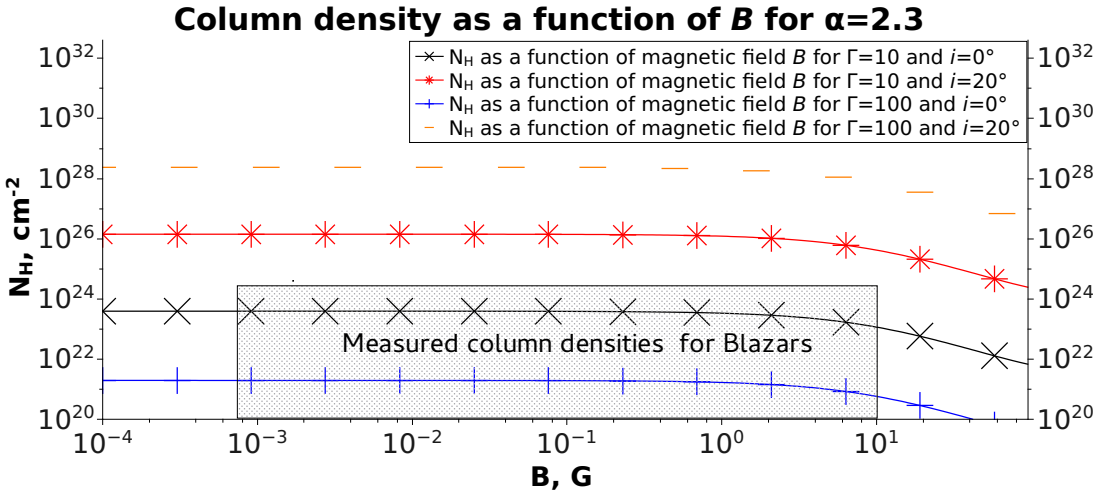

(D) Column density as a function of magnetic field B for different $\Gamma_{\rm B}$ and i, for $\alpha = 2.3$. The shaded area gives densities from [64] and [65]. The (blue) crossed line gives $N_{\rm H}$ for $\Gamma_{\rm B} = 100$; $i = 0°$, the (black) diagonal crossed line for $\Gamma_{\rm B} = 10$; $i = 0°$, the (red) star line for $\Gamma_{\rm B} = 10$; $i = 20°$ and the (orange) for $\Gamma_{\rm B} = 100$; $i = 20°$.

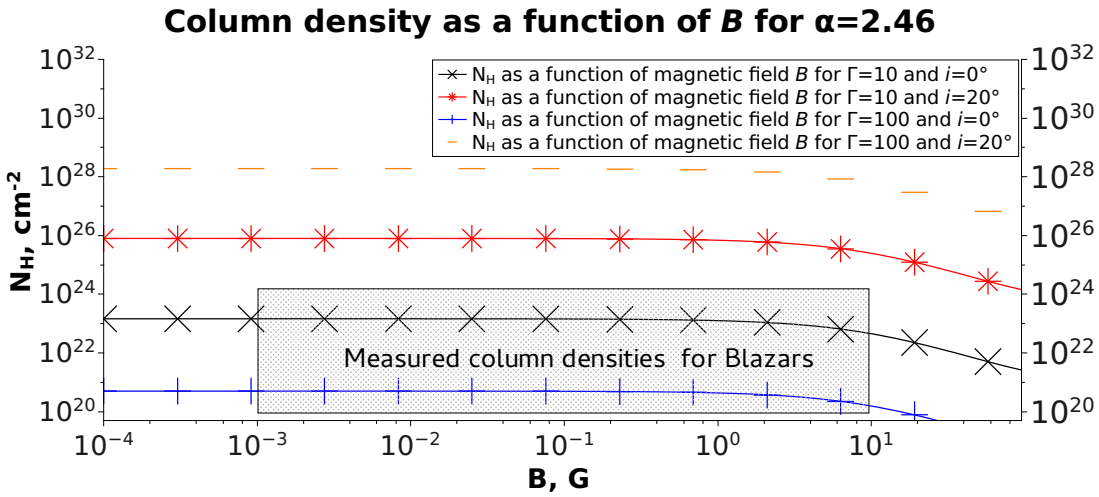

(E) Column density as a function of magnetic field B for different Γ_B and i, for $\alpha = 2.46$. The shaded area gives densities from [64] and [65]. The (blue) crossed line gives N_H for $\Gamma_B = 100$; $i = 0°$, the (black) diagonal crossed line for $\Gamma_B = 10$; $i = 0°$, the (red) star line for $\Gamma_B = 10$; $i = 20°$ and the (orange) for $\Gamma_B = 100$; $i = 20°$.

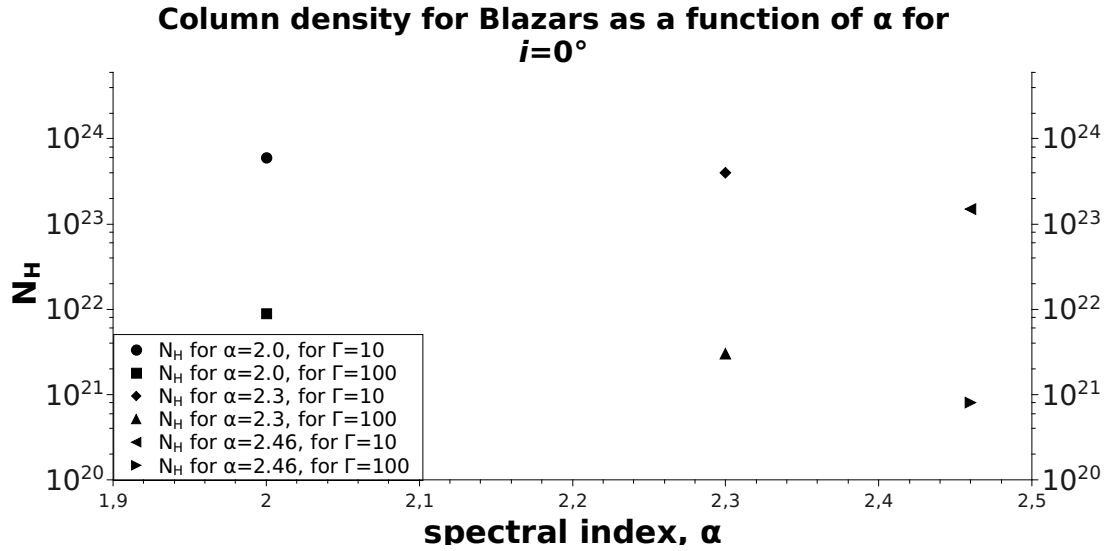

(F) Column density as a function spectral index α. The rectangle indicates N_H for $\Gamma_B = 100$, the dot for $\Gamma_B = 10$ in case of $\alpha = 2.0$. The rhombus indicates N_H for $\Gamma_B = 10$, triangle (up) for $\Gamma_B = 100$, in case of $\alpha = 2.3$. Triangle (left) for $\Gamma_B = 10$ and triangle (right) for $\Gamma_B = 100$, in case of $\alpha = 2.46$.

FIGURE 5.3: Calculated neutrino flux and column densities for Blazars, using the delta functional approximation. For the calculation of the densities current IceCube measurements from [24],[28] are used.

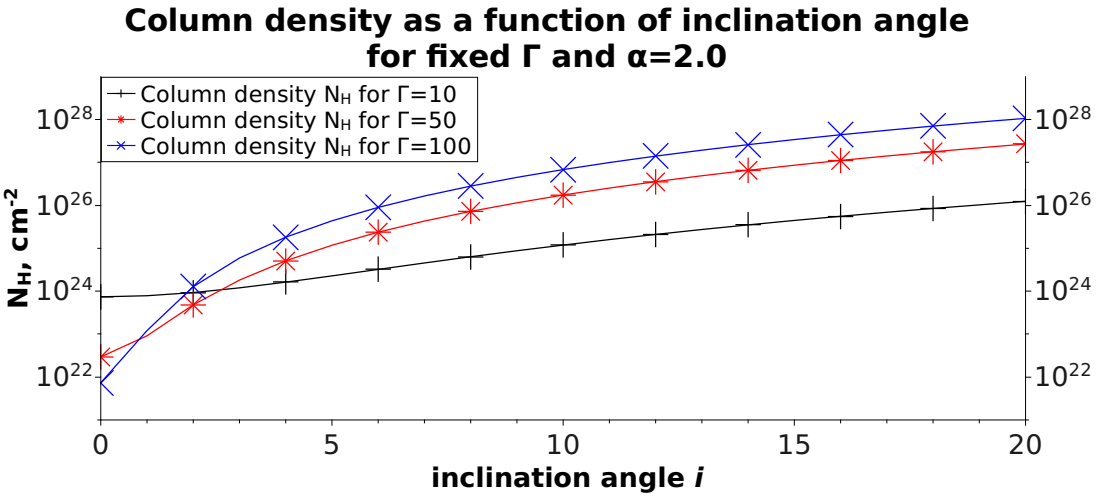

(A) Column density for fixed Lorentz factor Γ_B as a function of inclination angle i for $\alpha = 2.0$. The (black) crossed line gives the density for $\Gamma_B = 10$, the (red) star line for $\Gamma_B = 50$ and the (blue) diagonal crossed line for $\Gamma_B = 100$.

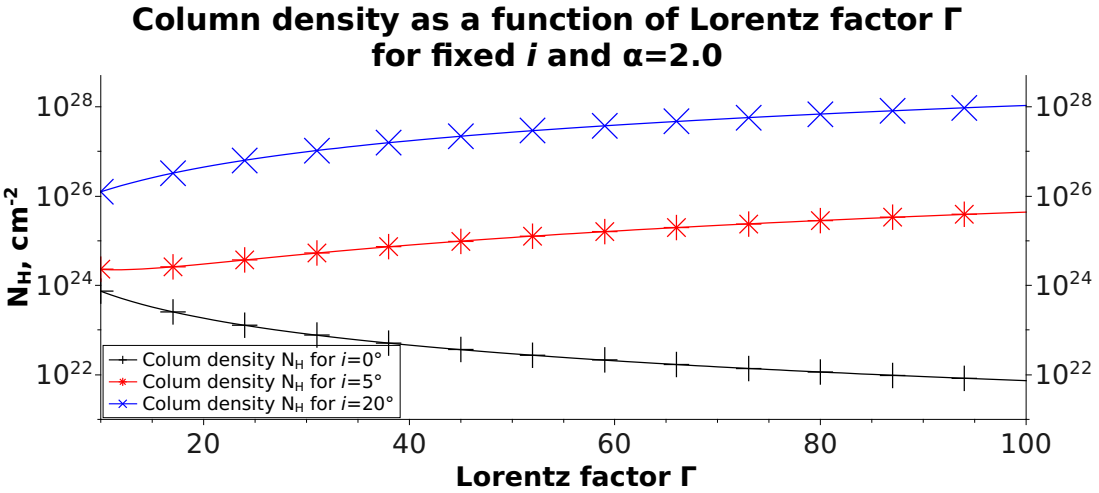

(B) Column density for fixed inclination angle i as a function of Lorentz factor Γ_B for $\alpha = 2.0$. The (black) crossed line gives the density for $i = 0°$, the (red) star line for $i = 5°$ and the (blue) diagonal crossed line for $i = 20°$.

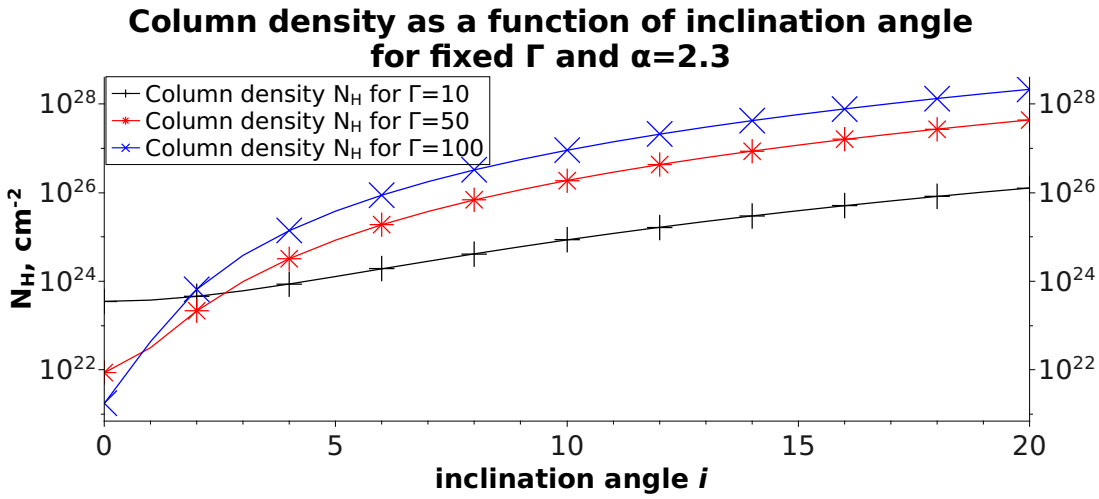

(C) Column density for fixed Lorentz factor Γ_B as a function of inclination angle i for $\alpha = 2.3$. The (black) crossed line gives the density for $\Gamma_B = 10$, the (red) star line for $\Gamma_B = 50$ and the (blue) diagonal crossed line for $\Gamma_B = 100$.

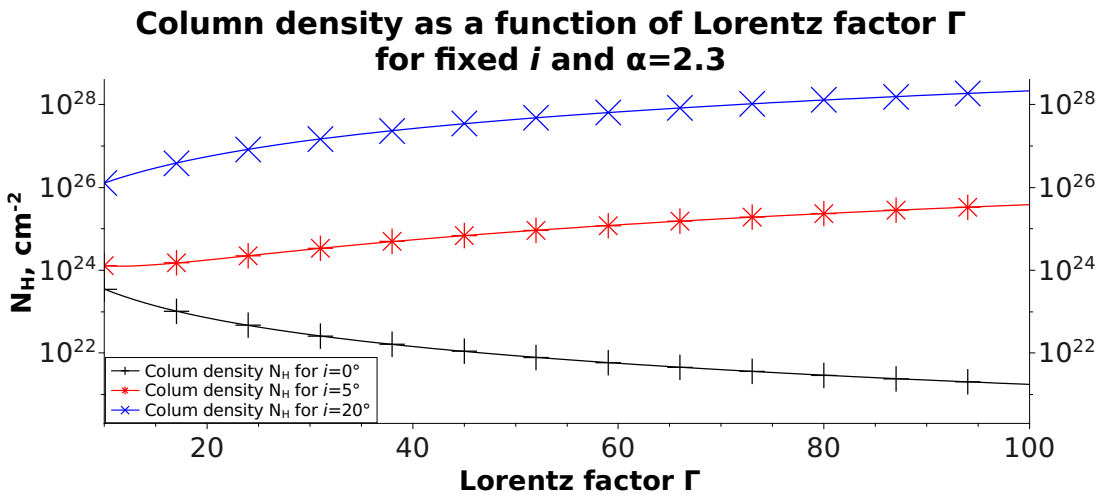

(D) Column density for fixed inclination angle i as a function of Lorentz factor Γ_B for $\alpha = 2.3$. The (black) crossed line gives the density for $i = 0°$, the (red) star line for $i = 5°$ and the (blue) diagonal crossed line for $i = 20°$.

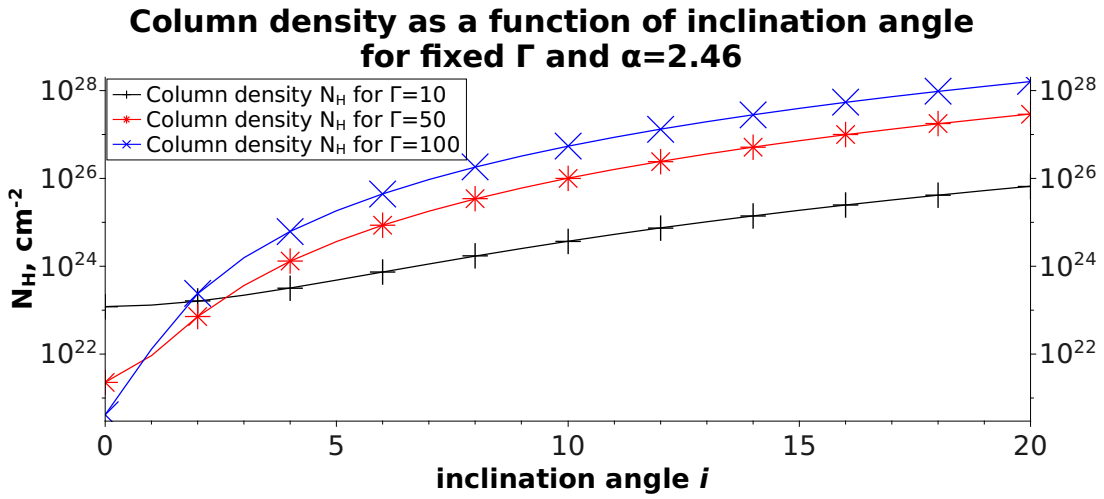

(E) Column density for fixed Lorentz factor Γ_B as a function of inclination angle i for $\alpha = 2.46$. The (black) crossed line gives the density for $\Gamma_B = 10$, the (red) star line for $\Gamma_B = 50$ and the (blue) diagonal crossed line for $\Gamma_B = 100$.

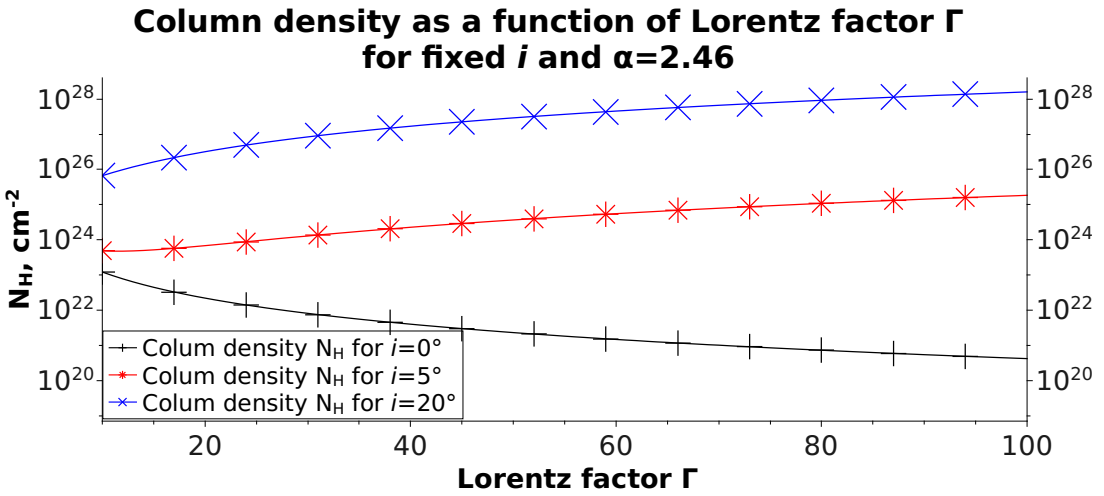

(F) Column density for fixed inclination angle i as a function of Lorentz factor Γ_B for $\alpha = 2.46$. The (black) crossed line gives the density for $i = 0°$, the (red) star line for $i = 5°$ and the (blue) diagonal crossed line for $i = 20°$.

FIGURE 5.4: Column density as a function of inclination angle i, for fixed Γ_B (Figure 5.4a, 5.4c, 5.4e) and as a function of Γ_B for fixed i (5.4b, 5.4d, 5.4f), for different spectral index α. The electron to proton ratio g_e, and $\chi(s, B)$ (Table 5.1) are fixed.

5.2 Semi analytical neutrino flux calculation for radio galaxies and Blazars

Having calculated the neutrino flux analytically by using a delta functional approximation, in this section a semi analytical method will be applied. The use of simple analytical methods can be justified only for a certain energy range and for special physical conditions, which have to be fixed. The results of such analytical methods may cause misleading conclusions, for example about the acceleration mechanism of particles. While fully numerical methods like PYTHIA, SIBYLL and QGSJet can directly be used to calculate neutrino fluxes, semi analytical methods not only reduce calculation time but also give an insight into characteristics of secondaries. Thus, we use a semi analytical method by giving analytical expressions for the distribution functions of secondaries F_ν and calculating fluxes by using numerical methods.
Considering the energy dependent distribution function F_ν of created neutrinos, the neutrino rate of a single source is:

$$\phi_\nu(E_\nu) = N_\mathrm{H} \int_{E_\nu}^{\infty} \sigma_\mathrm{pp}(E_\mathrm{p})\phi_\mathrm{p}(E_\mathrm{p}) F_\nu \left(\frac{E_\nu}{E_\mathrm{p}}, E_\mathrm{p}\right) \frac{\mathrm{d}E_\mathrm{p}}{E_\mathrm{p}} \tag{5.109}$$

$$= N_\mathrm{H} \int_0^1 \sigma_\mathrm{pp}\left(\frac{E_\nu}{x}\right) \phi_\mathrm{p}\left(\frac{E_\nu}{x}\right) F_\nu\left(x, \frac{E_\nu}{x}\right) \frac{\mathrm{d}x}{x} \qquad \text{with } x = \frac{E_\nu}{E_\mathrm{p}}, \tag{5.110}$$

$F_\nu\left(x, E_\nu/x\right)$ gives the number of created neutrinos per one inelastic $p-p$ interaction and x the fraction of the proton energy transferred to the neutrinos. For our calculation we use the energy dependent cross-section, which can be approximated by

$$\sigma_\mathrm{pp}(E_\mathrm{p}) = \left(34.3 + 1.88L + 0.25L^2\right)\left[1 - \left(\frac{E_\mathrm{th}}{E_\mathrm{p}}\right)^4\right]^2 \text{ with } L = \ln\left(\frac{E_\mathrm{p}}{10^3\,\mathrm{GeV}}\right), \tag{5.111}$$

with $E_\mathrm{th} = 1.22$ GeV giving the threshold energy of pion production [53]. Differences between semi analytical expressions, equation (5.109) and analytical ones, equation (5.7), are the energy dependent cross-section $\sigma_\mathrm{pp}(E_\mathrm{p})$ used in this section, and more detailed expressions for the energy distribution of secondaries. While the cross-section increases logarithmic and can be assumed to be constant for a wide energy range (Figure 5.5b), the main difference in the column densities will be due to different expressions for the energy distribution of the secondaries.

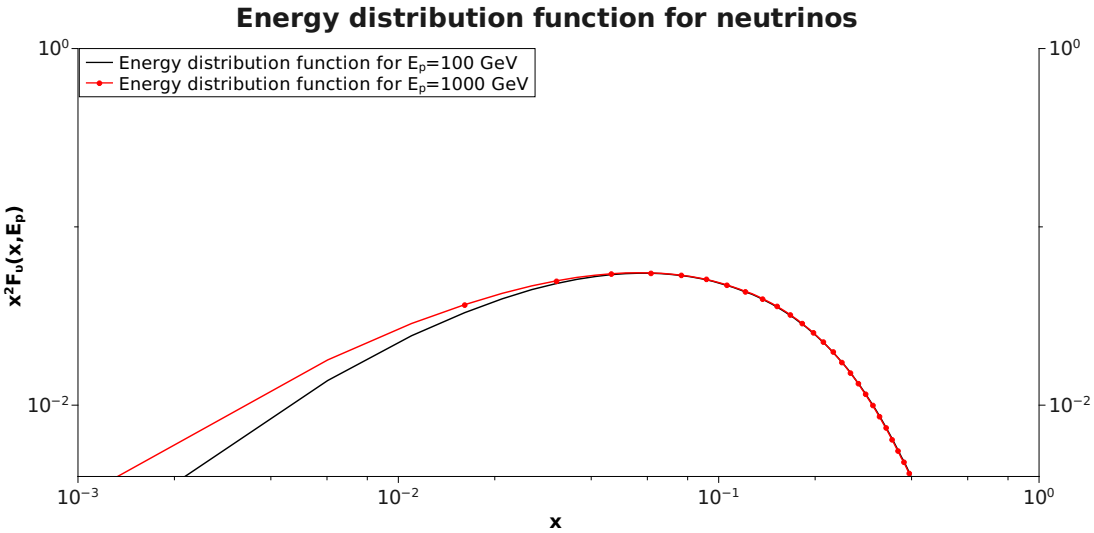

(A) Energy distribution function of neutrinos for different proton energies. The red (dotted) line shows the distribution function for $E_\mathrm{p} = 1000$ GeV and the black (solid) line for $E_\mathrm{p} = 100$ GeV. Due to the delta functional shape, analytical methods use delta functions to calculate fluxes.

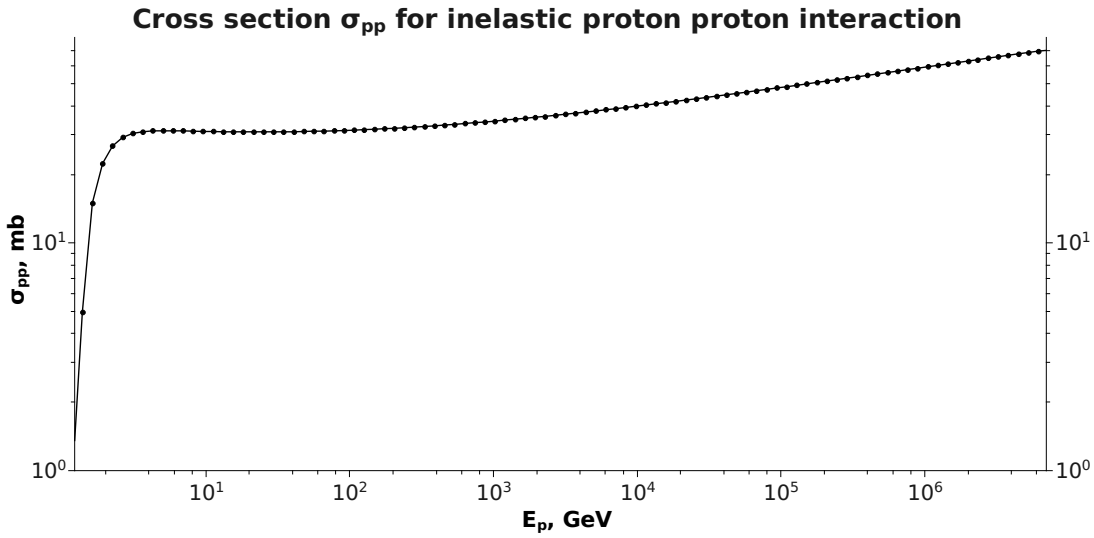

(B) Energy dependent cross-section $\sigma_\mathrm{pp}(E_\mathrm{p})$ for inelastic $p-p$ interaction. As can be seen the cross-section can be assumed to be constant for the energy range. 10^1 GeV $\leq E_\mathrm{p} \leq 10^4$ GeV.

FIGURE 5.5: Energy distribution function F_ν and the energy dependent cross section, which will be used to calculate the neutrino flux on Earth.

For the delta functional approach a simple ansatz, assuming that all created pions have an average energy of $\overline{E}_\pi = \frac{1}{6}E_\mathrm{p}^{3/4}$ and a simple power-law for the pion multiplicity $\epsilon(E_\mathrm{p})$ is used. In the semi analytical approach detailed expressions for the multiplicity and energy distribution,

-	$\alpha = 2.0$	$\alpha = 2.3$	$\alpha = 2.46$
$N_{\mathrm{H}}^{\mathrm{FR\text{-}I}}$(analytical)in cm^{-2}	$6.4\,10^{24}$	$7.4\,10^{24}$	$4.1\,10^{24}$
$N_{\mathrm{H}}^{\mathrm{FR\text{-}II}}$(analytical)in cm^{-2}	$1.1\,10^{25}$	$1.3\,10^{25}$	$8.2\,10^{24}$
$N_{\mathrm{H}}^{\mathrm{FR\text{-}I}}$(semi-analytical) in cm^{-2}	$3\,10^{24}$	$4\,10^{24}$	$3\,10^{24}$
$N_{\mathrm{H}}^{\mathrm{FR\text{-}II}}$(semi-analytical) in cm^{-2}	$6\,10^{24}$	$9\,10^{24}$	$5\,10^{24}$

TABLE 5.2: Column densities using analytical and semi analytical methods for different spectral index α, for FR-I and FR-II galaxies.

considered by the distribution function F_ν are used. For the energy range we are interested in ($E_{\mathrm{p}} \approx$ PeV) analytical expressions for the neutrino distribution F_ν and full numerical simulations deviate less than 10%, which can be neglected as error source, compared to other error sources, like the estimate of $\chi(s, B)$ and g_{e}, section 5.1.1. Thus, analytical expressions instead of fully numerical expressions for the distribution functions will be used [53]:

$$F_\nu^{(1)}(x, E_{\mathrm{p}}) = B\frac{\ln(y)^\beta}{y}\left(\frac{1-y^\beta}{1+k\,y^\beta(1-y^\beta)}\right)^4\left[\frac{1}{\ln(y)} - \frac{4\beta y^\beta}{1-y^\beta} - \frac{4k\beta y^\beta(1-2y^\beta)}{1+ky^\beta(1-y^\beta)}\right] \tag{5.112}$$

$$F_\nu^{(2)}(x, E_{\mathrm{p}}) = B_e\frac{(1+k_e\ln(x)^2)^3}{x(1+0.3/x^{\beta_e})}(-\ln(x))^5 \tag{5.113}$$

$$F_\nu^{\mathrm{tot}}(x, E_{\mathrm{p}}) = 2F_\nu^{(1)}(x, E_{\mathrm{p}}) + F_\nu^{(2)}(x, E_{\mathrm{p}}). \tag{5.114}$$

$F_\nu^{(1)}(x, E_{\mathrm{p}})$ gives the distribution of neutrinos, produced through the direct pion decay, while $F_\nu^{(2)}(x, E_{\mathrm{p}})$ gives the distribution function of neutrinos produced through the pion muon decay. Factor 2 can be explained by the fact that the distribution function of electron neutrinos can be approximated by $F_\nu^{(1)}(x, E_{\mathrm{p}})$. Due to the delta function shape of the distribution function (Figure 5.5a) it is clear why a delta functional approach is appropriate to give analytical expressions for the flux calculation. The calculation of the neutrino flux on Earth is based on the same assumptions, mentioned in the previous section.

The neutrino rate at the single source is convolved by the total number of the considered AGN sub-class. Further effects like adiabatic energy losses are also considered, resulting in the following expression for the neutrino flux at Earth:

$$\phi_\nu(E_\nu) = \frac{1}{3}N_{\mathrm{H}}\int_0^1\int_L\int_z \frac{F_{\mathrm{radio}}(L,z)}{4\,\pi d_L(z)^2}\sigma_{\mathrm{pp}}\left(\frac{E_\nu}{x}\right)\phi_{\mathrm{p}}\left(\frac{E_\nu}{x}\right)F_\nu^{\mathrm{tot}}\left(x, \frac{E_\nu}{x}\right)\frac{\mathrm{d}x}{x}\,\mathrm{d}L\frac{\mathrm{d}V}{\mathrm{d}z}\mathrm{d}z. \tag{5.115}$$

Column densities are obtained by using recent IceCube measurements. N_{H} is varied until the calculated and the detected flux match.

Results for densities, using the semi analytical method for FR-I and FR-II galaxies, for different spectral index α are listed in table 5.2. For a better overview the results using the delta functional approach are also listed. Differences between analytical and semi analytical methods can be explained by the energy range, we are interested in. The detected neutrinos have a maximum energy of few PeV. Up to these energies the pion multiplicity $\epsilon(E_{\mathrm{p}})$ from equation (5.3), can be used as a good approximation to calculate the neutrino flux without any considerable doubts. For higher energies, equation (5.3) will not give accurate results for the multiplicity, which is why semi analytical or full numerical methods must be applied. In Figure 5.6 the diffuse neutrino

flux and the column densities for different spectral indices are shown. Deviations from a power-law behavior can be explained by the energy dependent cross-section $\sigma_{\mathrm{pp}}(E_{\mathrm{p}})$ which becomes significant at energies above 10^3 GeV. Nevertheless, our semi analytical approach confirms our analytical results, excluding FR-II to be potential sources of high energy neutrinos, Figure 5.6d.

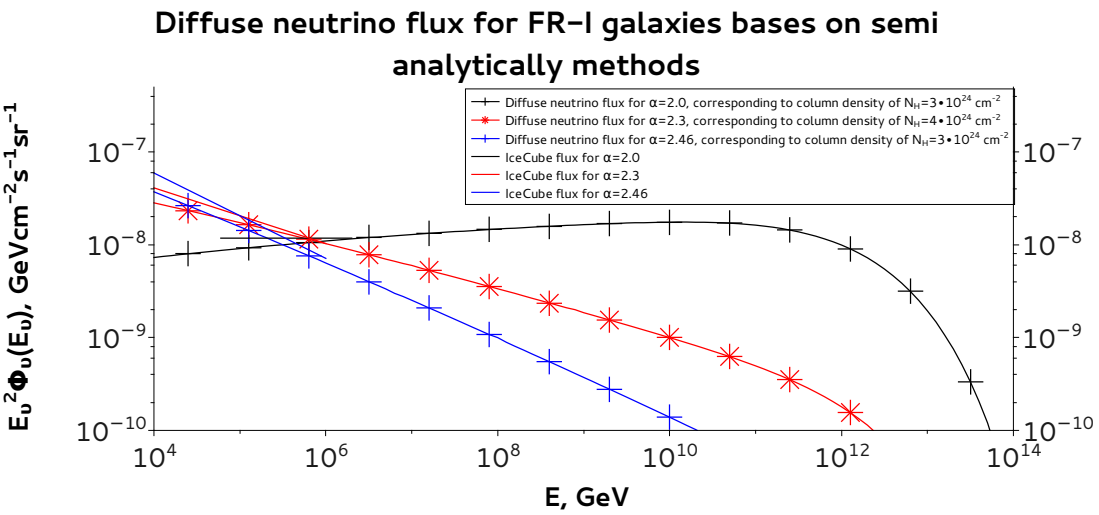

(A) Diffuse neutrino flux based on semi analytical methods for different spectral index α, for FR-I galaxies. For the calculation fixed values for g_e and $\chi(s, B)$ are used. The (blue) crossed line gives the flux for $\alpha = 2.46$. The blue solid line gives the IceCube signal for $\alpha = 2.46$. The (red) star line gives the flux for $\alpha = 2.3$. The red solid line gives the IceCube signal for $\alpha = 2.3$. The (black) diagonal crossed line gives the flux for $\alpha = 2.0$. The back solid line gives the IceCube signal for $\alpha = 2.0$. In Appendix A for each α the flux is shown in a separate plot.

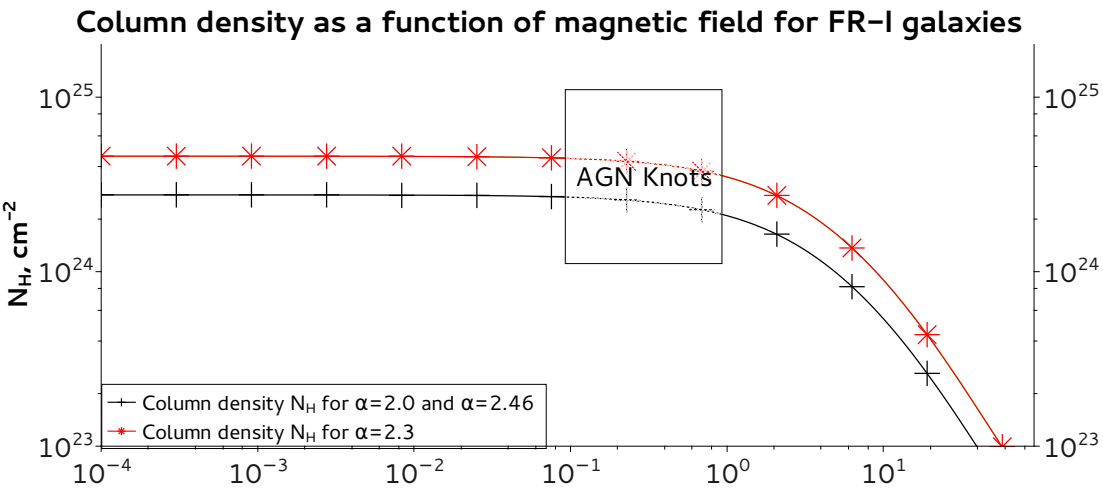

(B) Column density N_{H} as a function of magnetic field B for FR-I galaxies. The shaded area gives densities, used in common models. The (black) crossed line give N_{H} for $\alpha = 2.0$ and $\alpha = 2.46$. The (red) star line gives N_{H} for $\alpha = 2.3$. The rectangle gives the regions derived including uncertainties in the calculation, dominated by the parameters $\chi(s, B)$ and g_e

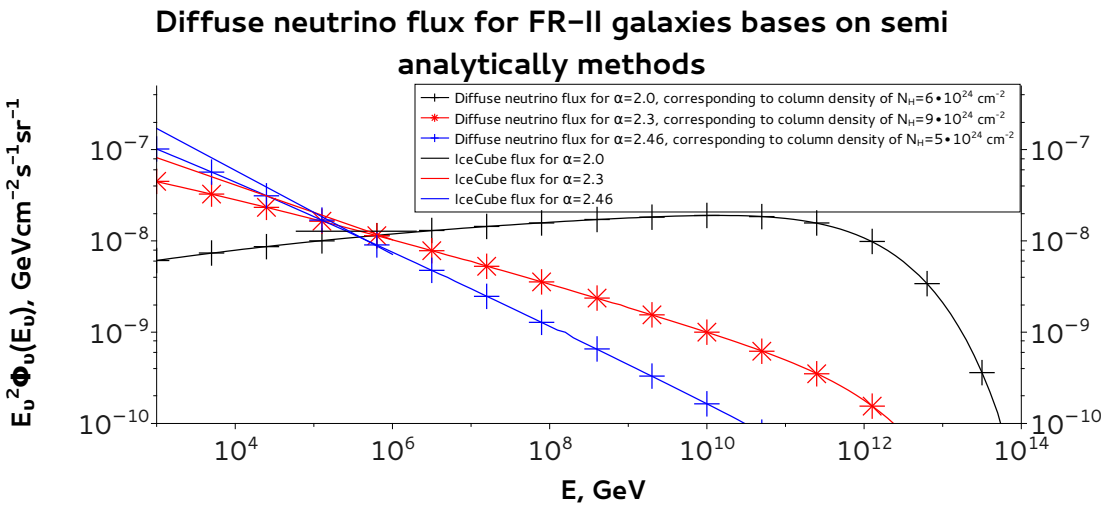

(C) Diffuse neutrino flux based on semi analytical methods for different spectral index α, for FR-II galaxies. For the calculation fixed values for g_e and $\chi(s, B)$ are used. The (blue) crossed line gives the flux for $\alpha = 2.46$. The blue solid line gives the IceCube signal for $\alpha = 2.46$. The (red) star line gives the flux for $\alpha = 2.3$. The red solid line gives the IceCube signal for $\alpha = 2.3$. The (black) diagonal crossed line gives the flux for $\alpha = 2.0$. The back solid line gives the IceCube signal for $\alpha = 2.0$. In Appendix A for each α the flux is shown in separate plot.

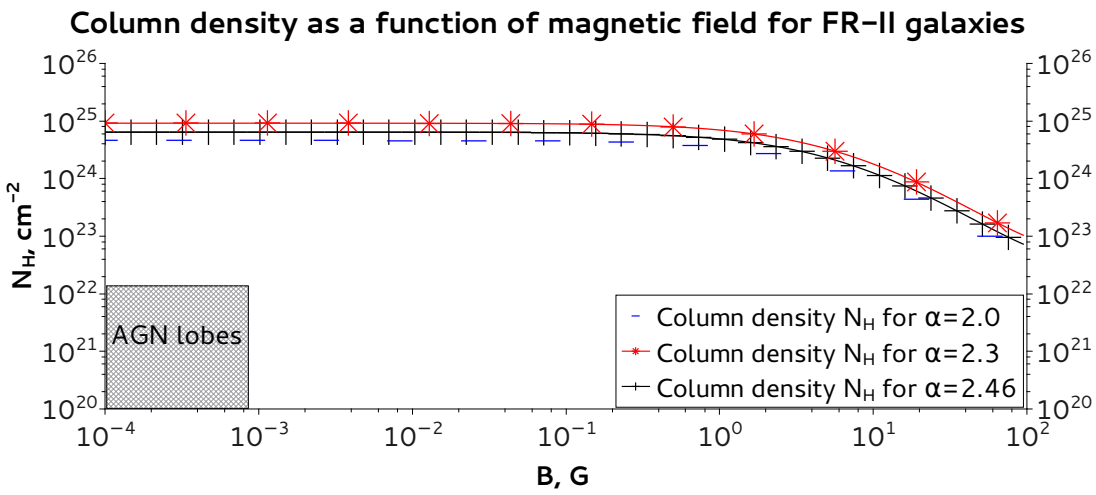

(D) Column density N_{H} as a function of magnetic field B for FR-II galaxies. The shaded area gives the column densities, used in common models. The (black) solid line give N_{H} for $\alpha = 2.46$, the (blue) dashed line for $\alpha = 2.0$. The (red) star line gives N_{H} for $\alpha = 2.3$. The rectangle gives the regions derived including uncertainties in the calculation, dominated by the parameters $\chi(s, B)$ and g_e.

FIGURE 5.6: Diffuse neutrino flux and column densities for FR-I and FR-II galaxies, based on semi analytical method, for different spectral index α and for fixed g_e and $\chi(s, B)$, see table 5.1. In Appendix A diffuse fluxes for different α are shown.

	$\Gamma_{\mathrm{B}} = 10; i = 0°$			$\Gamma_{\mathrm{B}} = 100; i = 20°$		
	$\alpha = 2.0$	$\alpha = 2.3$	$\alpha = 2.46$	$\alpha = 2.0$	$\alpha = 2.3$	$\alpha = 2.46$
N_{H} in cm^{-2}	$6 \cdot 10^{23}$	$4 \cdot 10^{23}$	$1.5 \cdot 10^{23}$	$1 \cdot 10^{28}$	$2.4 \cdot 10^{28}$	$1.9 \cdot 10^{28}$

TABLE 5.3: Column density for Blazars, for different spectral indices α and different Doppler factors δ. The results base on fixed proton to electron ratio g_{e} and fixed $\chi(s, B)$. The values for χ are listed in table 5.1.

To calculate the column density for Blazars, equation (5.115) will be modified by considering boosting effects:

$$\phi_\nu(E_\nu) = \varsigma\, N_{\mathrm{H}}\, \delta^\alpha \int_0^1 \int_{L,z} \frac{F_{\mathrm{radio}}^{\mathrm{Blazar}}\,(L,z)}{4\,\pi d_L(z)^2} \sigma_{\mathrm{pp}} \left(\frac{E_\nu}{x}\right) \phi_{\mathrm{p}} \left(\frac{E_\nu}{x}\right) F_\nu^{\mathrm{tot}} \left(x, \frac{E_\nu}{x}\right) \frac{\mathrm{d}x}{x}\, \mathrm{d}L \frac{\mathrm{d}V}{\mathrm{d}z} \mathrm{d}z \tag{5.116}$$

As analytical and semi analytical approaches give results for radio galaxies which are in the same range, the same is expected for Blazars[1]. N_{H} is obtained by varying the calculated fluxes until they match the detected IceCube observations, ϕ_{IceCube}.
Comparing N_{H} obtained by analytical methods, Figure 5.3, 5.4 with N_{H} obtained by semi analytical methods, Figure 5.7, show that our results are in agreement. The minimum column density is taken from Fermi observations.
Figure 5.7a shows N_{H} as a function of inclination angle i for different Γ_{B}. Increasing i leads to high column densities. Furthermore, the optical depth τ_{pp} is larger than one which is against the assumption of low optical depths, $\tau_{\mathrm{pp}} \ll 1$. The same situation can be found if N_{H} is plotted as a function of Γ_{B} for different inclination angles i, see Figure 5.7b. Adopting the range for the column density, equation 5.106 and for the magnetic field equation 5.105, the semi analytical calculations confirm that Blazars whose jets points to us, $i = 0°$, with Lorentz boost factors in the range $10 \leq \Gamma_{\mathrm{B}} \leq 100$ are potential CR sources, Figure 5.7c.

[1]The spectral shape does not differ from the shape obtained for FR galaxies (Figure 5.6a and Figure 5.6c. For this reason only column densities will be given

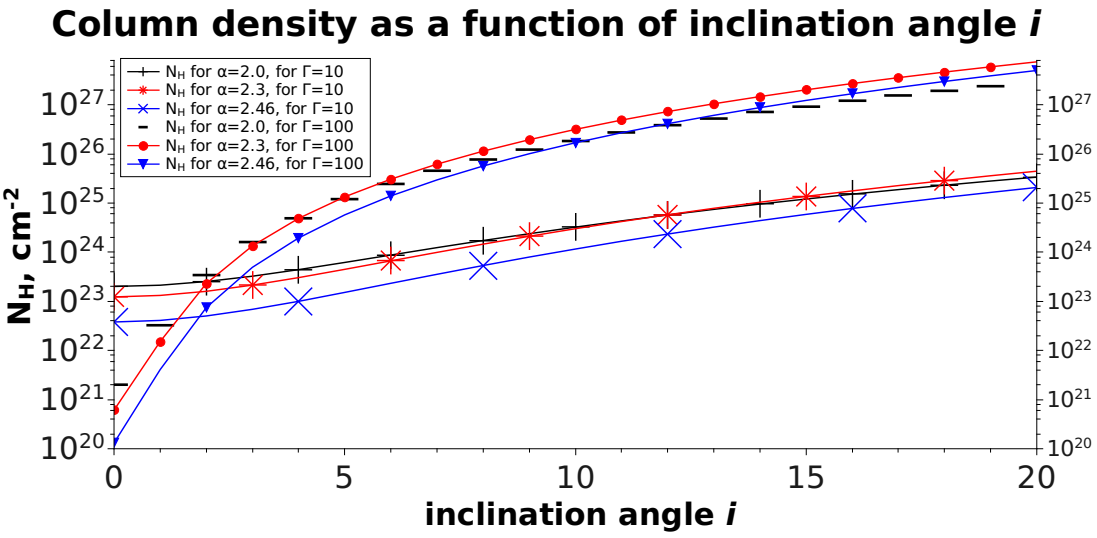

(A) Column density as a function of inclination angle i, for Blazars for different spectral index α, for fixed $\chi(s, B)$ and fixed g_e. The (blue) diagonal crossed, triangle down line give N_{H} for $\alpha = 2.46$ and $\Gamma_{\mathrm{B}} = 10, 100$. The (red) star, dotted gives for $\alpha = 2.3$ and $\Gamma_{\mathrm{B}} = 10, 100$. The (black) crossed, dashed line for $\alpha = 2.0$ and $\Gamma_{\mathrm{B}} = 10, 100$.

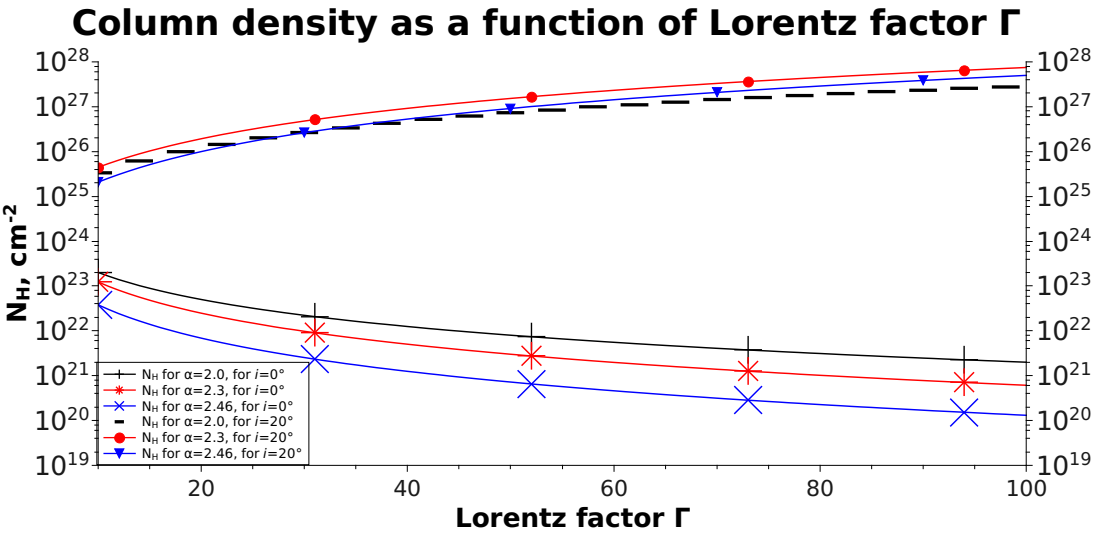

(B) Column density as a function of Lorentz factor Γ_{B}, for Blazars for different spectral index α, for fixed $\chi(s, B)$ and fixed g_e. The (blue) diagonal crossed, triangle down line give N_{H} for $\alpha = 2.46$ and $i = 0°, 20°$. The (red) star, dotted gives for $\alpha = 2.3$ and $i = 0°, 20°$. The (black) crossed, dashed line for $\alpha = 2.0$ and $i = 0°, 20°$.

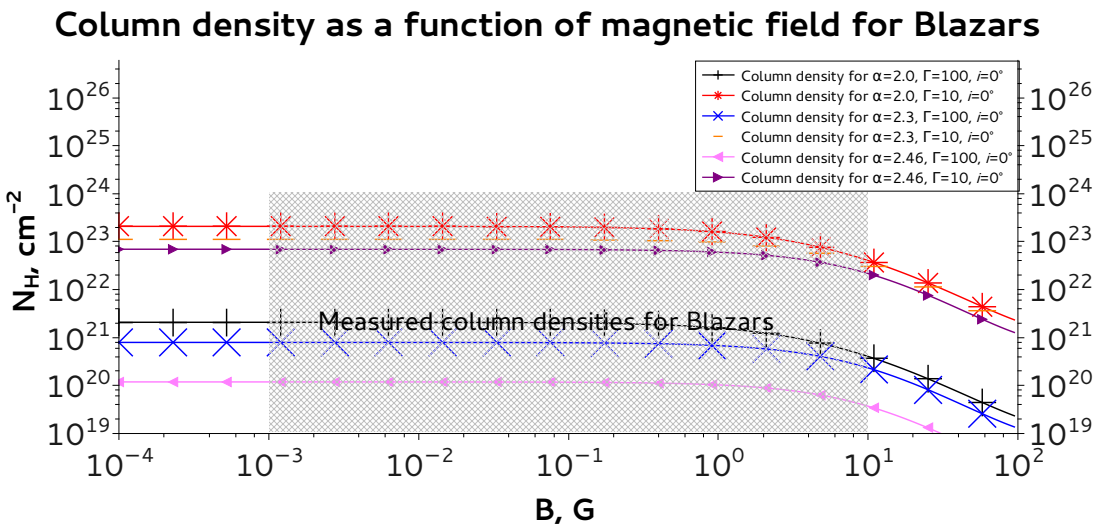

(c) Column density as a function of magnetic field B for different Γ_{B}, but fixed i. The shaded area gives the column density for common used models. The (black) crossed and (red) star line gives N_{H} for $\alpha = 2.0$, $\Gamma_{\mathrm{B}} = 100$ $\Gamma_{\mathrm{B}} = 10$. The (blue) diagonal crossed line and (dashed) orange line gives N_{H} for $\alpha = 2.3$, $\Gamma_{\mathrm{B}} = 100$ and $\Gamma_{\mathrm{B}} = 10$. The (pink) triangle left and (purple) triangle right gives N_{H} for $\alpha = 2.46$, $\Gamma_{\mathrm{B}} = 100$ and $\Gamma_{\mathrm{B}} = 10$.

FIGURE 5.7: Densities and fluxes calculated for Blazars. The shaded area in Figure 5.7c gives column obtained from observations [64].

Chapter 6

Calculating neutrino fluxes and column densities by using recent Fermi *LAT* observations

In the previous chapter the only measurable quantity used to calculate fluxes and column densities was radio luminosity functions $F_{\text{radio}}(L, z)$ for FR galaxies and Blazars. In this chapter, detailed Fermi *LAT* observations of seven radio galaxies are used to calculate the column densities and neutrino fluxes for AGN [68].
Fermi *LAT* is a pair conversion γ-ray telescope detecting photons with energies from 20 MeV to more than 300 GeV [69]. With an effective area of $> 8000\,\text{cm}^2$ and a field of view of ~ 2.4 sr of the full sky, it is designed for resolving the γ-ray sky and thus achieving a better understanding of physical mechanisms such as particle acceleration in sources like AGN, GRB or supernova remnants. As Centaurus A and Messier 87 are of special interest, they will be discussed in section 6.1.

With a distance of $d \approx 104$ Mpc, **NGC 6251** is classified as a FR-I galaxy with a radio luminosity of $L_{\text{radio}} \approx 9 \cdot 10^{30}\,\text{erg}\,\text{s}^{-1}\,\text{Hz}^{-1}\,\text{sr}^{-1}$ at 178 MHz. Radio images show that the inclination angle i is larger than $10°$. It contains a black hole with a mass of $(4-8)10^8 \cdot \text{M}_\odot$, which is assumed to be the main source of the observed X-ray radiation. Besides Fermi *LAT*, NGC 6251 is observed by Beppo-Sax and INTEGRAL [70].

3C 380, with a distance of $d \approx 4100$ Mpc has a steep radio spectrum. With a radio luminosity of $L_{\text{radio}} \approx 10^{35}\,\text{erg}\,\text{s}^{-1}\,\text{Hz}^{-1}\,\text{sr}^{-1}$ at 178 MHz, it is one of the most powerful radio sources. Many steep spectrum sources show FR-II structures. Indeed, 3C 380 seemed not to fit into this pattern [71]. However, sophisticated observations indicate that the source may be a FR-II galaxy, seen almost end-on. Characteristics such as superluminal motion in the core region or a halo which may be the overlapping lobes strengthen the idea that this source is an FR-II galaxy [71].

3C 207 ($d \approx 4000\,\text{Mpc}$; $z = 0.68$) is identified to be a FR-II galaxy with a relatively steep

radio spectrum, $\alpha \approx 0.9\,(F(\nu) \propto \nu^{-\alpha})$, between $150 - 750$ MHz. At higher frequencies it flattens, $\alpha \approx 0.64$ at 2.5 GHz. The diffuse X-ray emission is assumed to be produced through inverse Compton scattering of IR photons originating from the nuclear region [72].

3C 120 is a nearby Seyfert I radio galaxy, containing a black hole with a mass of $\sim 6 \cdot 10^7\,\mathrm{M}_\odot$. With a distance of ($d \approx 140\,\mathrm{Mpc}$; $z = 0.033$), it is quite nearby and well studied in all wavebands. Its radio morphology corresponds to a FR-I galaxy with a powerful one-sided jet. X-ray observations show strong variability on time scales from day to months. The origin of the emission is not answered yet [73].

3C 111 is a nearby ($d \approx 205\,\mathrm{Mpc}$; $z = 0.0485$) flat spectrum FR-II radio galaxy with a single sided jet. Although a counter jet is missing, a bright lobe is detected in the opposite direction of the observed jet, which is likely fed by the undetected counter jet [74].

6.1 Column densities and neutrino fluxes for Centaurus A and M 87

Due to their vicinity, Centaurus A (**Cen A**) and Messier 87 (**M 87**) are of special interest. With a distance of $d \approx 3.8\,\mathrm{Mpc}$; $z = 0.00183$, Cen A is the closest FR-I galaxy. It is near enough that its peculiar velocity dominates over the Hubble flow. It is well-studied through the entire electromagnetic spectrum from radio to γ-ray [75].
Fermi *LAT* observations of the core region show that the spectral index changes from $\epsilon_1 = 2.74 \pm 0.03$ below $E_{\mathrm{break}} \simeq 4$ GeV to $\epsilon_2 = 2.09 \pm 0.2$ above E_{break}, see Figure 6.1a. The break may be due to a superposition of different spectral components [76].
The low energy part of the flux can be approximated by

$$\phi_\gamma(E_\gamma)^{\mathrm{low}} = \phi_0^{\mathrm{low}}\, E_\gamma^{-\epsilon_1}, \tag{6.1}$$

and the high-energy part by

$$\phi_\gamma(E_\gamma)^{\mathrm{high}} = \phi_0^{\mathrm{high}}\, E_\gamma^{-\epsilon_2}. \tag{6.2}$$

There are several models that seek to explain the high-energy component of the flux. For example, it could be due to non-thermal processes of the magnetosphere of the black hole or due to $p\gamma$ interactions with UV or IR photons [76].
A further scenario, which is adopted in this work, is that the high-energy regime could be produced by high-energetic protons interacting with ambient matter, where among others π^0 are produced, which decay in $\gamma-$rays [76]. For this reason, the main focus is on the high-energy regime of the $\gamma-$ray flux.

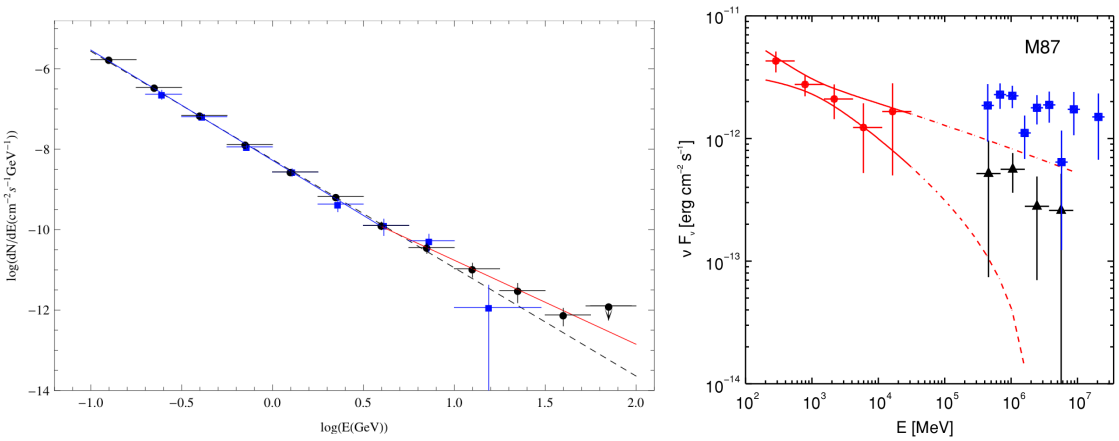

(A) Fermi $\gamma-$ray observations of the core of Cen A. The photon index ϵ becomes harder above $E_{\text{break}} = 4$ GeV, changing from $\epsilon_1 = 2.74 \pm 0.03$ to $\epsilon_2 = 2.09 \pm 0.2$ [76].

(B) $\gamma-$flux of M 87. The red circles gives the *LAT* observations, while the black triangles give H.E.S.S. observations of low state (year 2004), and blue squares show H.E.S.S. observations of high state (year 2005) [77]

FIGURE 6.1: Energy spectra of Centaurus A and Messier 87.

M 87 is, like Cen A, one of the closest ($d \approx 16\,\text{Mpc}$; $z = 0.00423$) and best studied AGN. At TeV energies it is observed by H.E.S.S. [78], MAGIC [79], and VERITAS [80]. The knot HST-1 and nucleus of M 87 show variability in the X-ray band on time scales of weeks to months [81]. Furthermore, variabilities in the high energy regime (TeV energies) are observed on time scales of ~ 1 day [81]. Figure 6.1b shows the $\gamma-$flux of M 87 during a low state in the year 2004 and during a high state in 2005.

The variability in the high-energy regime may be produced in the magnetosphere of the black hole [83], in star-jet interactions [82], or due to a complex jet geometry, collimating or decelerating jet [81].

A magnetospheric process can be the curvature emission of protons or electrons, which are accelerated in a vacuum gap of starved magnetosphere [83].

The low-energy regime changes smoothly to the low state TeV flux. In this work, it will be assumed that M 87 and all the other sources are in the low state activity while they were observed with the *LAT* telescope. Thus, there is no significant change in the spectral index ϵ, which must be considered for calculations.

6.2 $\gamma-$ray and neutrino flux calculation

Due to the vicinity of the objects $z \ll 1$, interactions of γ-rays with the electromagnetic background light (EBL) and adiabatic energy losses of neutrinos can be assumed to be negligible. The cross-section $\sigma_{\rm pp}$ can be assumed to be constant. Furthermore, the delta functional approximation can be used. Consequently, the flux is given by [53]

$$\phi_\gamma(E_\gamma) = \frac{2\,N_{\rm H}}{K_\pi}\frac{\sigma_{\rm pp}}{4\pi d_L^2}\int_{E_\gamma+\frac{m_\pi^2\,c^4}{4\,E_\gamma}}^{\infty}\frac{\phi_{\rm p}(E_{\rm p})}{\sqrt{E_\pi^2-(m_\pi\,c^2)^2}}\,{\rm d}E_\pi. \tag{6.3}$$

For the proton flux $\phi_{\rm p}(E_{\rm p})$, results from equation (4.34) are used. $K_\pi \approx 0.17$ gives the fraction of the incident proton energy transferred to the created γ-rays. Factor 2 considers the neutral pion decay in two γ-rays. The CR normalization $A_{\rm p}$ is calculated as explained in the previous section. Consequently, the column density as the only free parameter is fixed by varying $N_{\rm H}$ until the observed γ-ray flux fits the equation's calculation (6.3) fit. Figures 6.3a, 6.3c, 6.3e, 6.3g, 6.3i, 6.3k, and 6.3m show the $\gamma-$ray fluxes obtained by applying equation (6.3). $N_{\rm H}$ is varied for each source until Fermi *LAT* observations and computed fluxes fit.

Because in inelastic $p-p$ interactions, $\gamma-$ray and neutrino fluxes are linked, the computed column densities will be used to fix the neutrino flux for each source. These fluxes will be compared with the sensitivity of current neutrino telescopes, IceCube (Figure 6.2a) and ANTARES (Figure 6.2b) and with the sensitivity of the future telescope KM3NeT (Figure 6.2c).

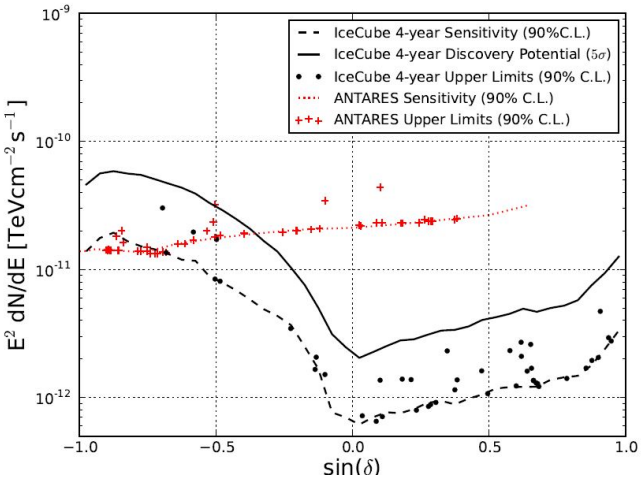

(A) IceCube four-year sensitivity (black dashed line), four-year Discovery Potential (black line) and four-year upper limits (black dots). For clarification the ANTARES sensitivity (red dashed) and upper limits (red dots) are also shown [84].

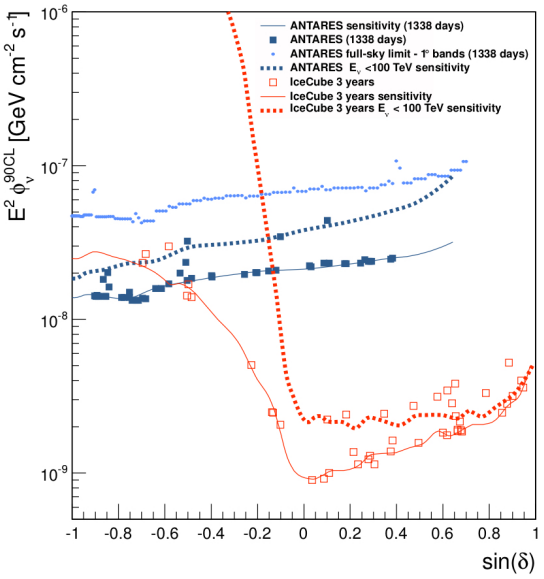

(B) ANTARES sensitivity (blue line). As can be seen the IceCube sensitivity (red dashed line) for the Northern Hemisphere is several magnitudes better than the sensitivity of ANTARES [85].

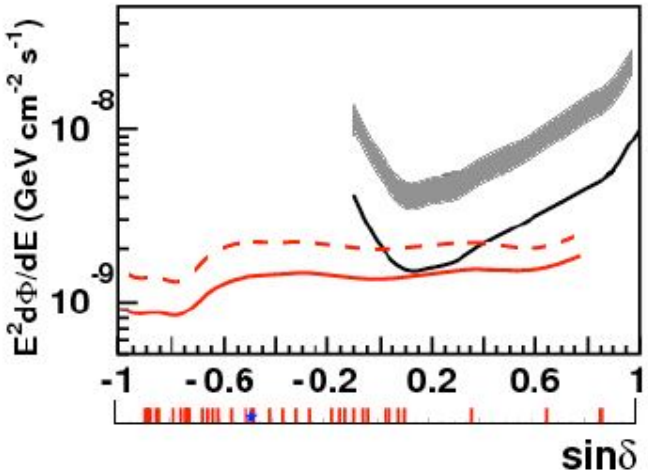

(C) Predicted one-year sensitivity of KM3NeT. If completed it will have a better sensitivity in both Hemispheres than IceCube [23].

FIGURE 6.2: Sensitivities of current (IceCube and ANTARES) and future (KM3NeT) neutrino telescope are used to verify the $p-p$ model used in this work.

Cen A is the only source whose calculated neutrino flux is below the one year sensitivity of KM3NeT, see Figure 6.3b. Thus, KM3NeT will be, if completed, more than suitable to give strong constraints on inelastic $p-p$ interactions as the source of neutrino production. Furthermore, constraints on parameters like g_e and $\chi(s, B)$ can be given. Consequently, Cen A is an excellent candidate to be detected by KM3NeT.

For M 87, the IceCube four-year sensitivity is less than one magnitude above the calculated flux, while the one year sensitivity of KM3NeT is approximately one magnitude above the flux, see Figure 6.3d. With passing of time, the sensitivity of KM3NeT will be better, in four years better than the sensitivity of IceCube [23], and M 87 will be a promising candidate to be identified as a possible neutrino source. The sensitivity of ANTARES is for all the sources more than one magnitude above the calculated fluxes. Consequently, ANTARES is not suitable to detect neutrinos from the sources.

For 3C111 it is a similar situation. The IceCube and the KM3NeT sensitivity are approximately the same and approximately one magnitude above the calculated flux, see Figure 6.3f. Even this source will be a good candidate to verify the $p-p$ model if KM3NeT is in use for a long time.

In 3C120 (Figure 6.3h), 3C 207 (Figure 6.3j), and 3C 380 (Figure 6.3l) the situation is similar to 3C111. Their fluxes and sensitivities deviate about one magnitude.

Due to its localization, NGC 6251 is out of the field of view of KM3NeT and ANTARES. However, the sensitivity of IceCube is more than one magnitude above the calculated flux. Thus, NGC 6251 is not suitable for focus as a neutrino source.

It must be mentioned that all sensitivities are given for an E_ν^{-2} flux. However, the sources considered in this work have photon indices deviating from a pure E_γ^{-2} behavior. Since $\gamma-$ray flux and neutrino flux are linked, the neutrino flux also deviates from an E_ν^{-2} behavior. Only Cen A has a spectral index $\epsilon_{\text{Cen A}} = 2.12$ which is comparable with the sensitivity of the detectors. Thus, errors due to different indices are negligible in comparison to errors originating from calculations of g_e and $\chi(s, B)$ as it is $\epsilon_{\text{detector}}/\epsilon_{\text{Cen A}} \approx 0.94$. The same argumentation can be applied for M 87, the second potential candidate.

For the rest, deviations due to different spectral indices become larger and must be considered for the future.

As can be seen, $\gamma-$ray observations can be used to give strong constraints on the $p-p$ model, since in this model the number of free parameters is lower than the number of free parameters in $p\gamma$ interactions.

The two closest objects Cen A and M 87 are of special interest. Their spectral indices ϵ are comparable with the telescope sensitivities, and their neutrino predicted fluxes are in the same range like the sensitivity of KM3NeT. For Cen A, the calculated flux is below the sensitivity.

Consequently, these two objects can be used to verify the $p-p$ model and give strong constraints on g_e and $\chi(s, B)$.

Thus, KM3NeT will give a unique opportunity to verify the model used in this work.

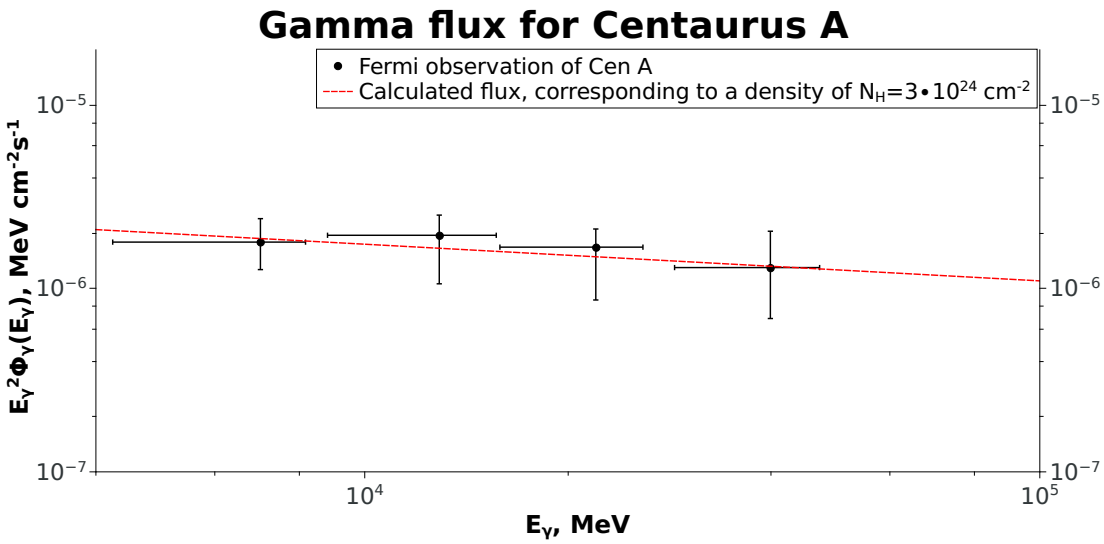

(A) Fermi *LAT* observation of Cen A. For the calculation the high-energy part of the core flux is taken. The photon flux is fitted with a power-law function with a spectral index of $\epsilon = 2.12$, for $g_e = 0.06$ and $\chi = 95$.

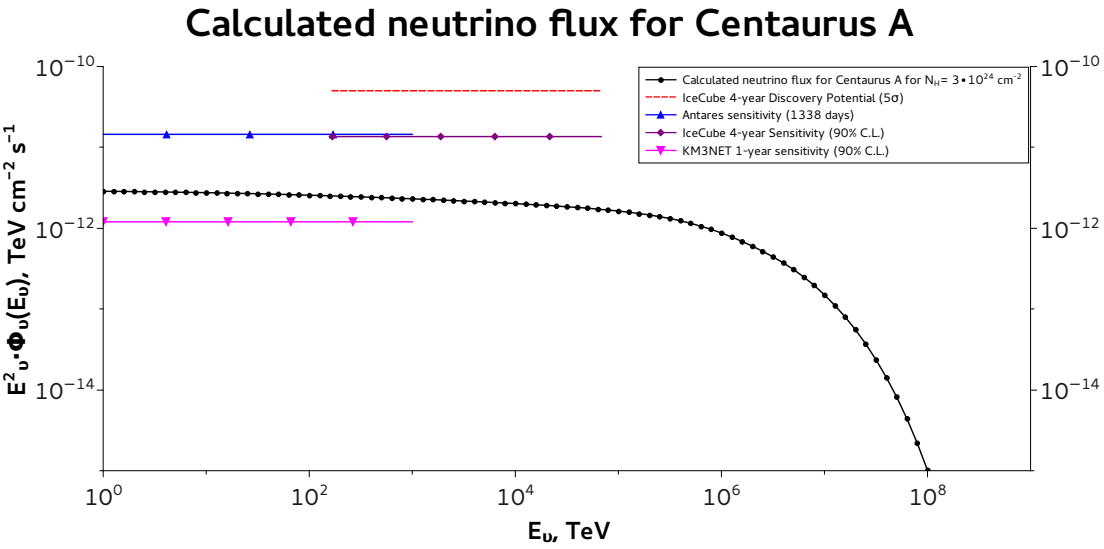

(B) Calculated neutrino flux for Cen A. The column density is fixed through Fermi *LAT* γ-observations. The blue horizontal line with triangle up gives the ANTARES sensitivity, the red dashed line the IceCube 4-year discovery potential, the magenta line with triangle down the KM3NeT 1-year sensitivity, and the rhombus violet line gives the IceCube 4-year sensitivity. The KM3NeT sensitivity is below the calculated flux. Thus, Cen A is a promising candidate which will give strong constraints on the used model in this work.

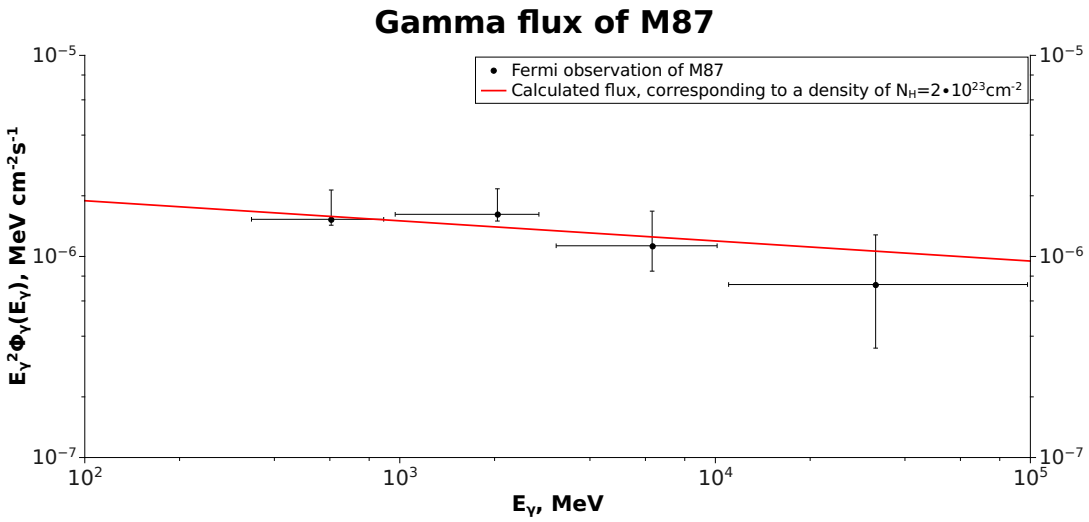

(C) Fermi *LAT* observation of M 87 The photon flux is fitted with a power-law function with a spectral index of $\epsilon = 2.21$for $g_e = 0.06$ and $\chi = 60$.

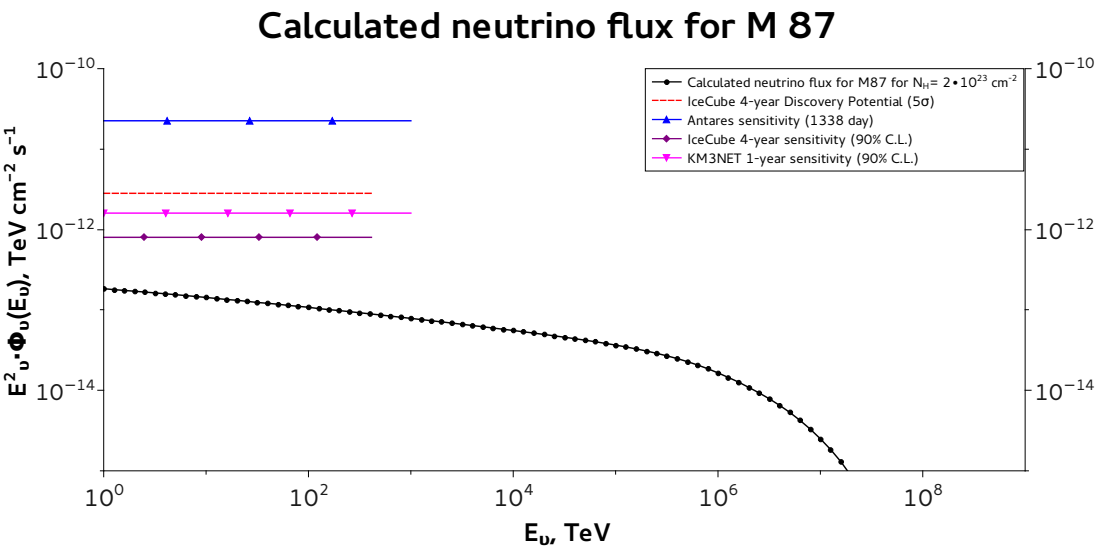

(D) Calculated neutrino flux for M 87. The column density is fixed through Fermi *LAT* γ-observations. The blue horizontal line with triangle up gives the ANTARES sensitivity, the red dashed line the IceCube 4-year discovery potential, the magenta line with triangle down the KM3NeT 1-year sensitivity, and the rhombus violet line gives the IceCube 4-year sensitivity. The KM3NeT 1-year sensitivity is less than one magnitude above the calculated flux. Thus, with passing time, the sensitivity improves and M 87 is a promising candidate which will give strong constraints on the used model in this work.

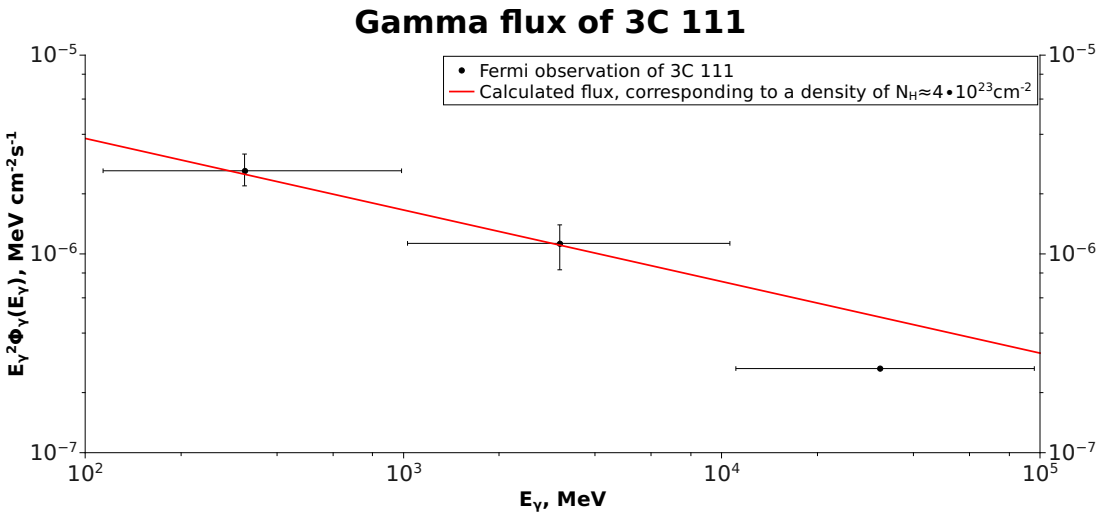

(E) Fermi *LAT* observation of 3C 111. The photon flux is fitted with a power-law function with a spectral index of $\epsilon = 2.36$, for $g_e = 0.06$ and $\chi = 30$.

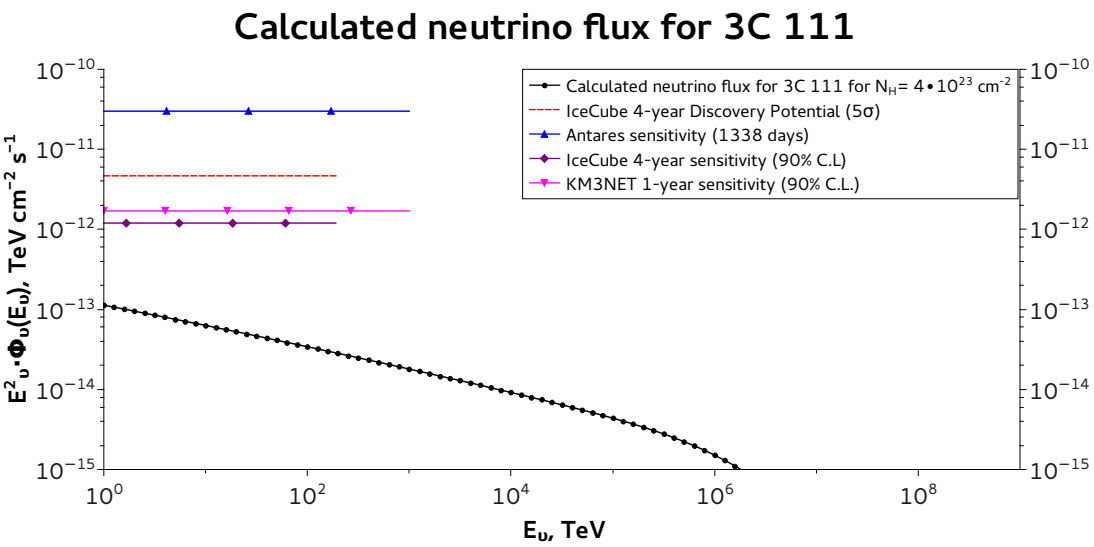

(F) Calculated neutrino flux for 3C 111. The column density is fixed through Fermi *LAT* γ-observations. The blue horizontal line with triangle up gives the ANTARES sensitivity, the red dashed line the IceCube 4-year discovery potential, the magenta line with triangle down the KM3NeT 1-year sensitivity, and the rhombus violet line gives the IceCube 4-year sensitivity. The KM3NeT 1-year sensitivity is approximately one magnitude above the calculated flux. Thus, with passing time, the sensitivity improves and 3C 111 is a promising candidate which will give strong constraints on the used model in this work.

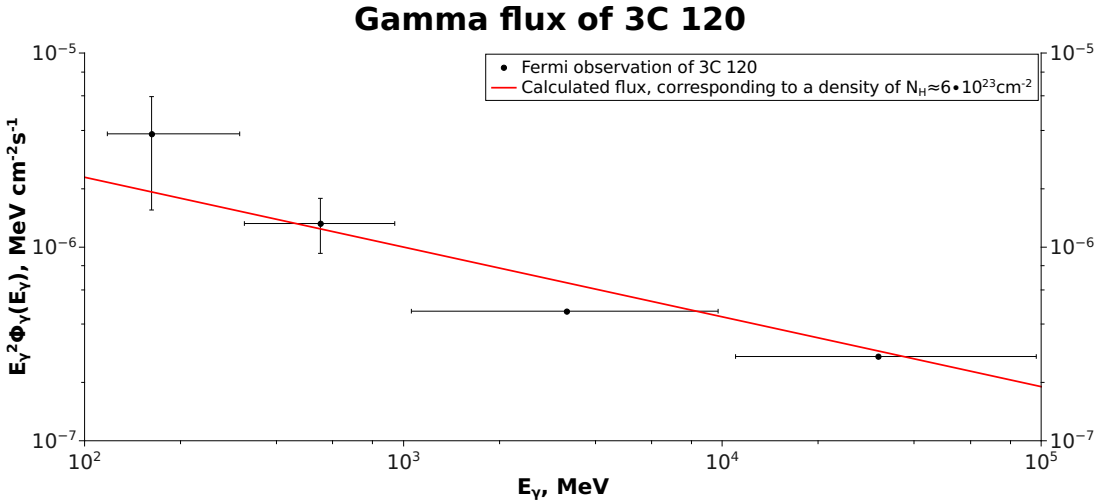

(G) Fermi *LAT* observation of 3C 120. The photon flux is fitted with a power-law function with a spectral index of $\epsilon = 2.36$, for $g_e = 0.06$ and $\chi = 30$.

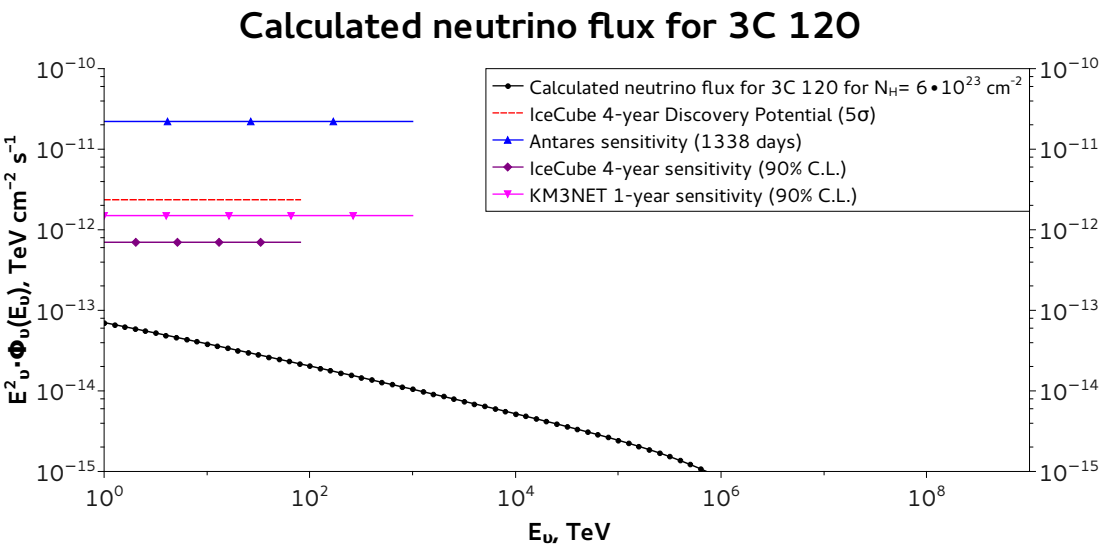

(H) Calculated neutrino flux for 3C 120. The column density is fixed through Fermi *LAT* γ-observations. The blue horizontal line with triangle up gives the ANTARES sensitivity, the red dashed line the IceCube 4-year discovery potential, the magenta line with triangle down the KM3NeT 1-year sensitivity, and the rhombus violet line gives the IceCube 4-year sensitivity.

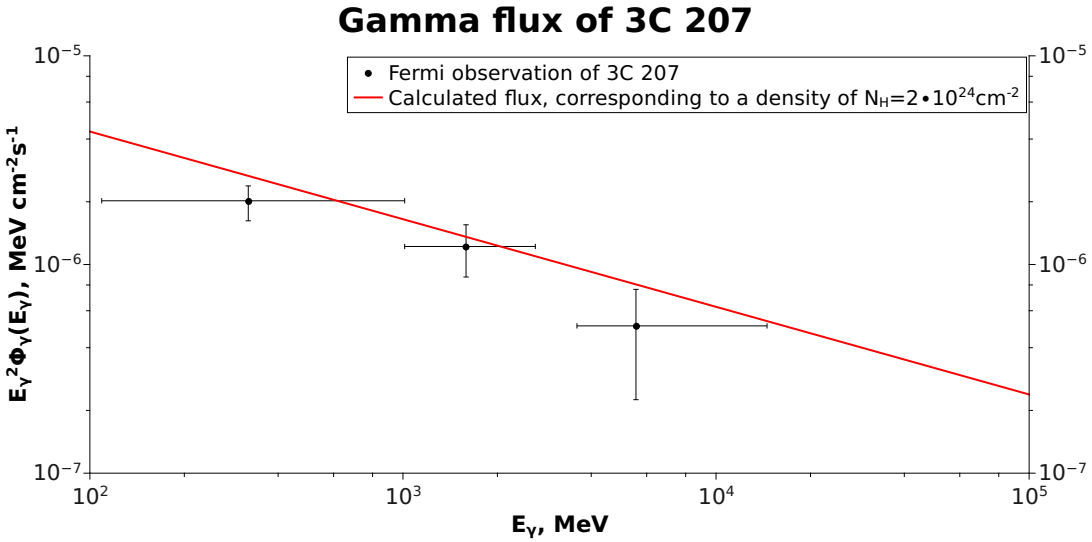

(I) Fermi *LAT* observation of 3C 207. The photon flux is fitted with a power-law function with a spectral index of $\epsilon = 2.42$, for $g_e = 0.06$ and $\chi = 26$.

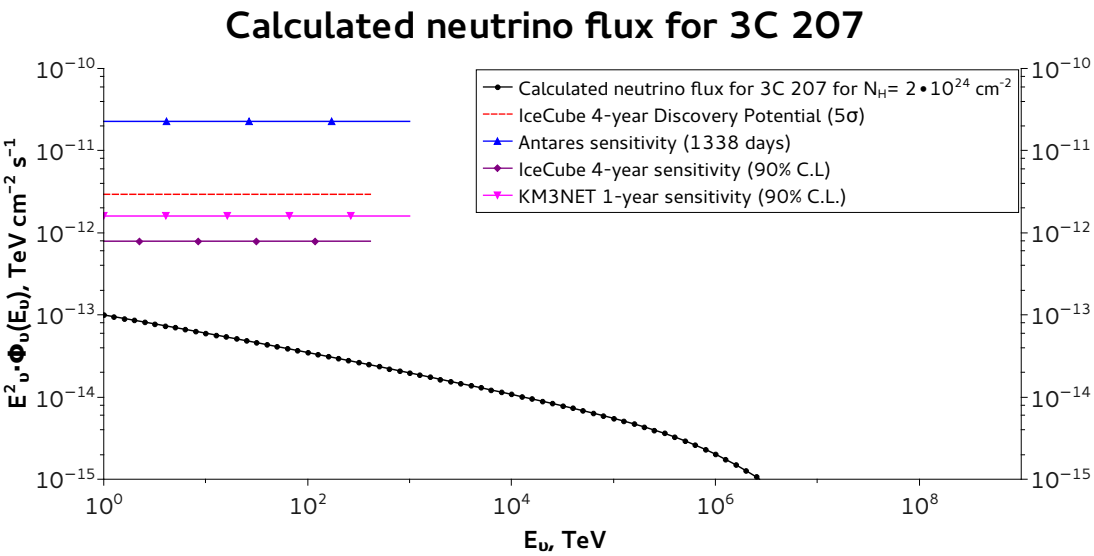

(J) Calculated neutrino flux for 3C 207. The column density is fixed through Fermi *LAT* γ-observations. The blue horizontal line with triangle up gives the ANTARES sensitivity, the red dashed line the IceCube 4-year discovery potential, the magenta line with triangle down the KM3NeT 1-year sensitivity, and the rhombus violet line gives the IceCube 4-year sensitivity.

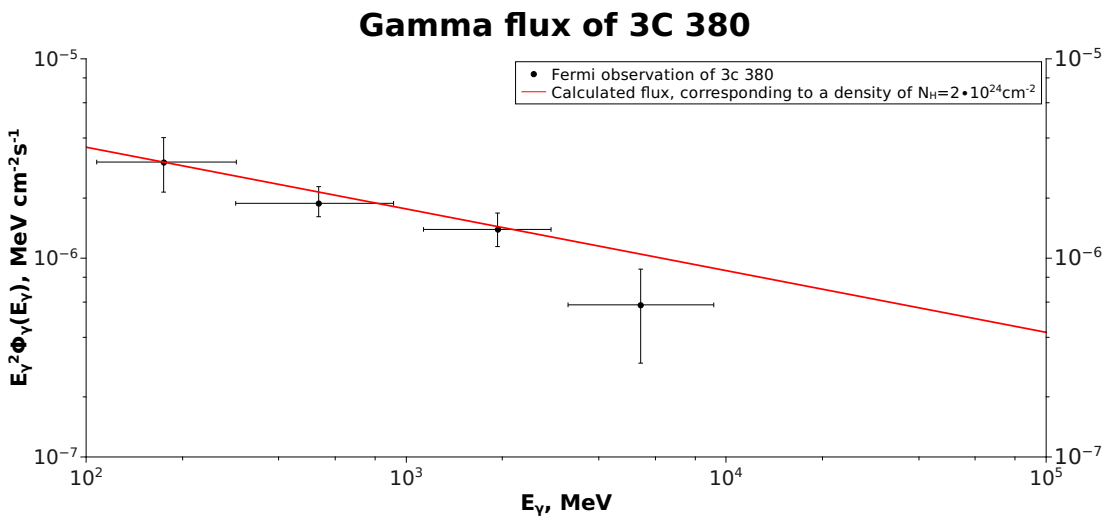

(K) Fermi *LAT* observation of 3C 380. The photon flux is fitted with a power-law function with a spectral index of $\epsilon = 2.21$, for $g_e = 0.06$ and $\chi = 60$.

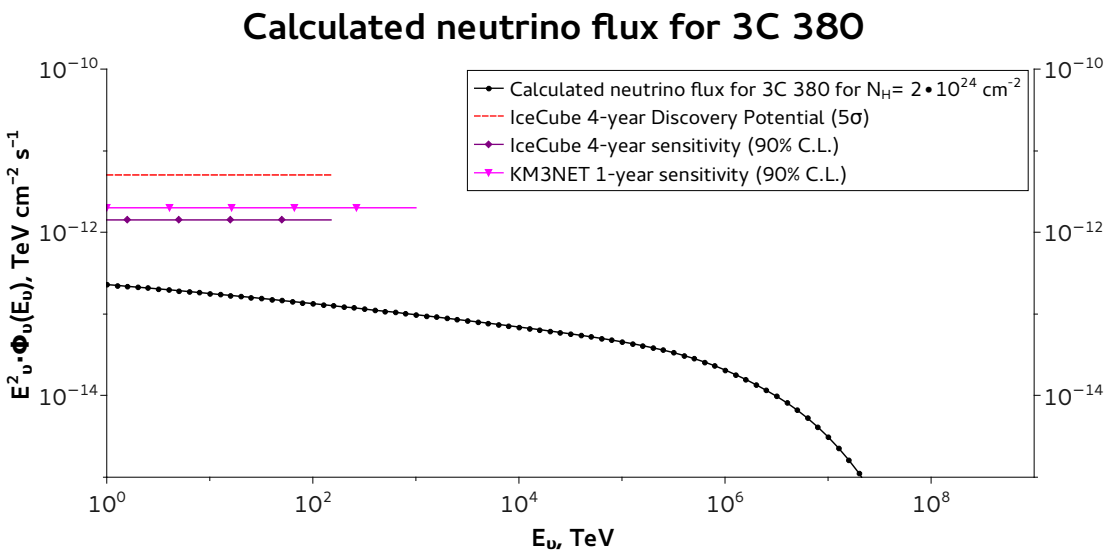

(L) Calculated neutrino flux for 3C 380. The column density is fixed through Fermi *LAT* γ-observations. The red dashed line gives the IceCube 4-year discovery potential, the magenta line with triangle down the KM3NeT 1-year sensitivity, and the rhombus violet line gives the IceCube 4-year sensitivity. Since 3C 380 is located outside the field of view of ANTARES no sensitivity is given.

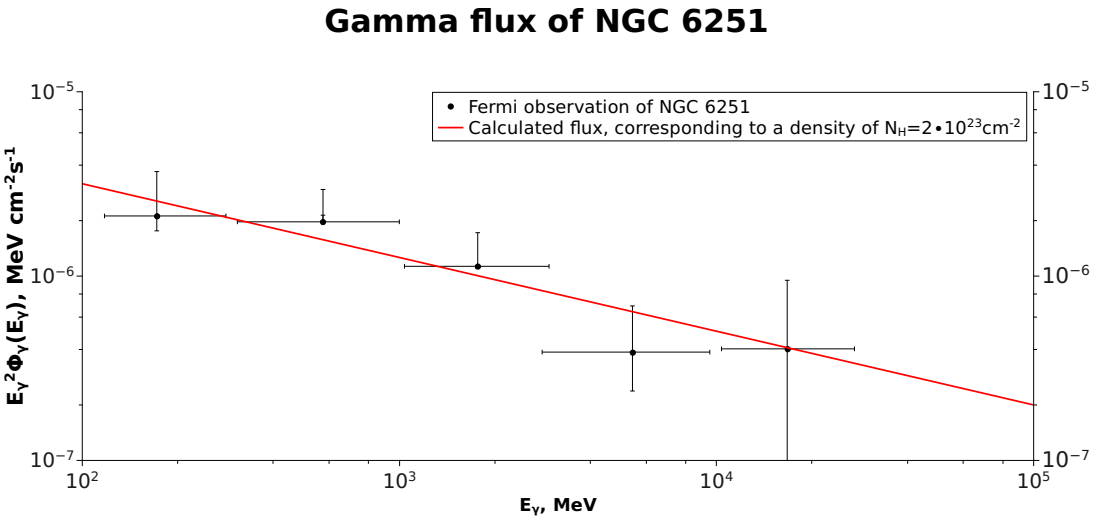

(M) Fermi *LAT* observation of NGC 6251. The photon flux is fitted with a power-law function with a spectral index of $\epsilon = 2.4$, for $g_e = 0.06$ and $\chi = 26$.

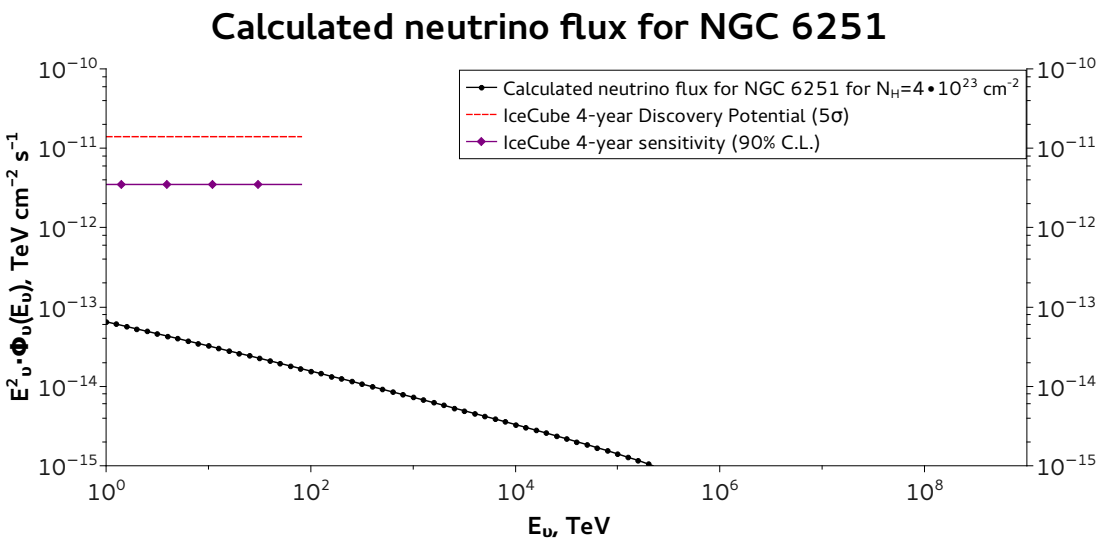

(N) Calculated neutrino flux for NGC 6251. The column density is fixed through Fermi *LAT* γ-observations. The red dashed line gives the IceCube 4-year discovery potential and the rhombus violet line gives the IceCube 4-year sensitivity. Since NGC 6251 is located outside the field of view of ANTARES and KM3NeT no sensitivity is given.

FIGURE 6.3: $\gamma-$ray observations and calculated neutrino fluxes for FR-I galaxies. The $\gamma-$ray measurement is taken from [68]. The (red) horizontal line gives the IceCube sensitivity for an E^{-2} spectrum.

Chapter 7

Conclusion & Outlook

The goal of this thesis is to test which AGN sub-classes are suitable to describe the detected neutrino flux. Current IceCube observations of high-energy neutrinos are used to test the used ansatz. Fermi LAT observations are used to make estimates about the point source neutrino fluxes for FR-I galaxies.
The main focus is on inelastic proton-proton interactions in Active Galactic Nuclei (AGN), where protons interact with ambient matter, and produce charged and neutral pions. Charged pions decay subsequently into neutrinos of different flavor and neutral decay in $\gamma-$ rays. The thesis is divided in six chapters:
Chapter 1 gives a historical introduction into the field of astrophysics. The motivation why focussing on AGN and the outline is given.
Chapter 2 gives a brief introduction into the physics of Cosmic Rays (CRs). Furthermore it is explained why neutrinos are excellent candidates to give information about acceleration processes and prodcution region in astrophysical sources. Chapter 2 ends with a brief summary of current and future neutrino telescopes. Here, the main focus is on the IceCube detections of high energetic neutrinos, which are used to calculate column densities for radio galaxies and Blazars 2.5.2.
Chapter 3 gives an introduction into the physics of AGN. In this work it is assumed that these extragalactic objects are sources of high energetic CRs. Furthermore, it is assumed that inelastic $p-p$ interactions take place in AGN jets.

In chapter 4 the transport equation for protons is solved. In this ansatz, it is tested what shape the proton have, after transport. Energy loss is considered by inelastic $p-p$ interactions and adiabatic expansion of the blob, section 4.1. Energy gain is considered by acceleration of protons in magnetic field irrigularities. The proton flux, see equation (4.31), is a function of several parameters, which in turn are a combination of basic physics parameters. The determination of these parameters or functions is very complex or almost impossible, since the only tool we have are electromagnetic observations of AGN. The exact plasma conditions within the blob are mainly unknown.
Observational properties like the ratio of electrons to protons g_e are be used to constrain these

parameters.

Chapter 5 deals with analytical and semi analytical methods which are used to calculate diffuse neutrino fluxes and column densities for radio galaxies and Blazars. The electron to proton ratio g_e and electron to radio luminosity ratio $\chi(s, B)$ are fixed by measurable quantities and compared with theoretical models, see section 5.1.1 and section 5.1.2. Theoretical results for g_e are obtained by assuming same spectral indices for the electron and proton population. This is justified, because both species are accelerated in Fermi I and Fermi II processes, leading to power-law functions for the particle distribution.

In section 5.2 a semi analytical ansatz is applied. The results are compared with analytical calculations. Assuming a common blob size of $R = 10^{15}$ cm and a particle density of $n_{\mathrm{H}} = 10^9\,\mathrm{cm}^{-3}$ for FR-I galaxies, our calculated, spectral indices α and magnetic field B dependent column densities are in agreement with theoretical models, see Figure 5.2b. The column density remains constant up to a critiqual magnetic field B_{c}, which depends on the minimum Lorentz factor γ_{min} of the electron population, and decreases for $B \geq B_{\mathrm{c}}$, due to the $N_{\mathrm{H}} \propto \chi(s, B)^{-1}$ behavior, for each AGN sub-class.

Consequently, knots of FR-I galaxies are potential candidates to be sources of high-energy CRs and neutrinos. On the other side, the lobes of FR-II galaxies can be ruled out, to be sources of high energy CRs and neutrinos, detected column densities are much smaller than needed to produce the observed signal.

Adopting the ansatz of a relativistic moving blob along the jet, the jet size increases, while moving along the jet. Since protons may escape from the blob or lose energy to fall below the threshold energy for pion prodcution, the effective particle density n_{H} within the blob decreases. Assuming a lobe size of $R = 10^{22-23}$ cm and a particle density of $n_{\mathrm{H}} = 0.01 - 0.1\,\mathrm{cm}^{-3}$, our calculated and predicted column column densities disagree, see Figure 5.2d, exlcuding lobes of FR-II galaxies as potential sources of high-energy CRs and neutrinos.

For Blazars, whose fluxes and column densities depend on the Doppler factor δ, N_{H} is given as a function of the magnetic field B, for different spectral indices α, different Lorentz boost factor Γ_{B} and inclination angle i. Adopting Fermi *LAT* observations of 23 Blazars [64], $\gamma-$ray observations of Flat Spectrum Radio Quasars [65], give a range for column densities, and magnetic fields [66].These results are used to give constraints on Γ_{B} and inclination angle i. According to that, Blazars with $10 \leq \Gamma_{\mathrm{B}} \leq 100$ and $i = 0°$, for all considered neutrino spectral indices α fulfill the condition to be potential sources of high energy CRs and neutrinos, see Figure 5.4a, 5.4c and 5.4e.

Chapter 6 deals with Fermi *LAT* observations of seven close radio galaxies, including the two closest AGN Centaurus A (Cen A) and Messier 87 (M 87).

Assuming that $\gamma-$rays are produced through the decay of neutral pions, $\gamma-$ray and neutrino flux are linked. Fermi *LAT* observations are used to calculate the column density. In equation 6.3 (section 6.2) N_{H} as the only free parameter will be varied, until *LAT* measurments and calculated fluxes are equal, for example Figure 6.3a. The column densities are used to fix the neutrino fluxes.

For Cen A, the calculated neutrino flux is below the sensitivities of the neutrino telescopes, except KM3NeT. Thus, KM3NeT is a chance to verify the used ansatz of neutrino production through inelastic $p - p$ interactions. Furthermore, constraints on parameters like $\chi(s, B)$ and g_e can be given. Although the sensitivities of all telescopes are given for E_ν^{-2} fluxes, erros due to

differnt spectral indices for Cen A are negligible, in comparison to other error sources like the estimation of g_e and $\chi(s, B)$, since it is $\epsilon_{\text{detector}}/\epsilon_{\text{Cen A}} = 2.0/2.12 \approx 0.94$

M 87, the second close AGN has calculated neutrino fluxes below the sensitivity of all telescopes. However, with passing time the sensitivity of KM3NeT will be in the same range like the calculated flux, making M 87 as a potential source to verify the ansatz, and to give constraints on $\chi(s, B)$ and g_e.

For all other sources neutrino fluxes and sensitivities differs more than one magnitude. Additionally, errors due to different spectral indices become significant.

One of the most important parameters used to calculate fluxes and column densities are radio luminosity functions, which also play an important role in the normalization of the CR flux A_{p} and in fixing the electron to proton ratio g_e. Consequently they have a large influence on the calculations. In this work the radio luminosity function $F_{\text{radio}}^{\text{FR-I,FR-II}}(L, z)$ for radio galaxies is from the year 2001 and for Blazars $F_{\text{radio}}^{\text{Blazars}}(L, z)$ from the 1990. More updated functions with sophisticated telescopes will reduce uncertainties in the parameters and will give better results for densities and fluxes.

Detailed observations of the CR spectrum, specially of the high energy regime ($E_{\text{CR}} \geq 10^{18}$) eV will help to have more accurate results for the CR normalization A_{p}.

The ratio of electron luminosity L_e to radio luminosity L_{radio} is fixed by the electron population $\mathrm{d}N/\mathrm{d}\gamma_e$. To guarantee analytical solutions for $\chi(s, B)$ a power-law function is assumed. Other assumptions lead to the fact that calculations can only be solved numerically. In a further step different more complex functions can be adopted to calculate $\chi(s, B)$ numerically and to give more exact results.

While in this work seven close radio galaxies are considered and their fluxes are compared with the sensitivities of neutrino telescops, and increase in numbers of radio galaxies will help to have more statistics and thus more results. These results can be used to verify used ansatz, used in this work.

Of special interest are Cen A and M 87, the two closest AGN which are in the field of view of the future telescope KM3NeT and which have fluxes comparable with the one year sensitivity. Thus, KM3NeT gives a great oppurtunity to verify the $p - p$ model and to give strong constraints on parameters like g_e and $\chi(s, B)$.

Zusammenfassung & Ausblick

Das Ziel der Arbeit ist es, zu überprüfen, welche AGN-Unterklassen geeignet sind, den von IceCube beobachteten Neutrinofluss zu beschreiben. Fermi LAT-Beobachtungen werden verwendet, um Neutrinoflüsse von Punktquellen zu berechnen.
Das Hauptaugenmerk dieser Arbeit liegt auf inelastischen Proton-Proton Wechselwirkungen. In diesen Wechselwirkungen werden neben geladenen Pionen, die in Neutrinos zerfallen, auch neutrale Pionen erzeugt, die ihrerseits in Photonen zerfallen. Die Arbeit ist wie folgt aufgebaut:
Kapitel 1 gibt eine historische Einführung in das Thema der Astrophysik und endet mit der Begründung dafür, wieso Aktive Galaxien berücksichtigt werden.
Kapitel 2 gibt eine kurze Einführung in die Physik der kosmischen Strahlung und erklärt, welche galaktischen und extragalaktischen Quellen für die beobachteten Teilchen verantwortlich sein können. Weiterhin wird in Abschnitt 2.4 erklärt, wieso Neutrinos ausgezeichnete Teilchen sind, um physikalisch wichtige Informationen über die Beschleunigung und über die Quellen selbst zu erhalten. Desweiteren wird in Abschnitt 2.5 das Prinzip der Neutrinodetektion erklärt. Kapitel 2 hört mit dem Abschnitt über die Detektion hochenergetischer Neutrinos mit Hilfe des IceCube-Detektors auf, Abschnitt 2.5.2.
Kapitel 3 beschäftigt sich mit der Physik der Aktiven Galaxien. Da in dieser Arbeit Aktive Galaxien eine wichtige Rolle spielen, werden ihre physikalischen Eigenschaften erörtert. Abschnitt **??** beschreibt ein mögliches Szenario, wie die charakteristischen Jets produziert werden könnten. Aktive Galaxien zeichnen sich auch dadurch aus, dass sich in ihnen einige Objekte mit Überlichtgeschwindigkeit bewegen. Die Erklärung des Effekts, der auch ein weiteres Indiz für ein massives schwarzes Loch als Energiequelle ist, wird in Abschnitt 3.3 gegeben.
Ein wichtiger Punkt sind radio Leuchtkräfte, die verwendet werden, um die Berechnung durchführen zu können. Aus diesem Grund gibt Abschnitt 3.4 eine kurze Einführung in das Thema der Synchrotronstrahlung hochenergetischer Elektronen.
Kapitel 3 wird durch die Theorie der Vereinheitlichung der Aktiven Galaxien (Abschnitt 3.9) beendet.
In Kapitel 4 wird die Transportgleichung für Protonen gelöst. Hierfür muss der Energieverlust (Abschnitt 4.1) sowie der Energiegewinn durch Streuung an Magnetfeldern (Abschnitt 4.2) berücksichtigt werden. Die Lösung der Transportgleichung ist eine Potenzfunktion, die von vielen Parametern abhängig ist, die ihrerseits von anderen Parametern abhängig sind, deren Bestimmung komplex ist. Aufgrund dieser Tatsache werden die Parameter zusammengefasst und durch messbare Größen substituiert.
In Kapitel 5 werden Neutrinoflüsse und Säulendichten für FR-I, FR-II und Blazare sowohl analytisch, als auch semianalytisch berechnet und miteinander verglichen. Die Säulendichte wird durch die aktuelle IceCube-Beobachtung hochenergetischer Neutrinos festgelegt. Zur Berechnung der Flüsse und Säulendichten wird das Elektron-zu-Protonverhältnis g_e sowie das Verhältnis der Elektron- zur Radioleuchtkraft berechnet (Abschnitt 5.1.1 und Abschnitt 5.1.2). Für die theoretische Berechnung der Größe g_e werden gleiche spektrale Indizes für Elektronen und Protonen angenommen. Dies kann durch die Annahme der Teilchenbeschleunigung durch Fermi I und Fermi II erklärt werden.
Aus den berechneten Flüssen können für FR-I-und FR-II-Galaxien Einschränkungen für den

Produktionsort der Neutrinos innerhalb des Jets abgeleitet werden. Unter der Annahme einer Blobgröße von $R = 10^{15}$ cm und einer Teilchendichte von $n_{\mathrm{H}} = 10^{15}\,\mathrm{cm}^{-3}$ innerhalb des Blobs für FR-I-Galaxien ergibt sich eine Säulendichte, die mit der berechneten Säulendichte übereinstimmt, siehe Abbildung 5.2b. Aufgrund dieser Tatsache können die "knots" von FR-I-Galaxien als potenzielle Quellen der hochenergetischen kosmischen Strahlung und Neutrinos in Frage kommen. Für FR-II-Galaxien sehen die Resultate anders aus. Unter der Annahme einer Lobegröße von $R = 10^{22-23}$ cm und einer Teilchendichte von $n_{\mathrm{H}} = 0.01 - 0.1\,\mathrm{cm}^{-3}$ ergeben sich Säulendichten, die mit den hier berechneten Werten nicht übereinstimmen. Somit können die Lobes von FR-II-Galaxien als Quellen hochenergetischer kosmischer Strahlung sowie Neutrinos mit großer Wahrscheinlichkeit ausgeschlossen werden.

In Kapitel 6 werden für sieben nahe FR-I-Galaxien Fermi LAT-Beobachtungen verwendet, um aus den gemessenen $\gamma-$Flüssen Neutrinoflüsse zu berechnen.

Die $\gamma-$Flüsse werden anhand von Gleichung (6.3) berechnet. Alle Parameter bis auf die Säulendichte N_{H} sind bestimmt. N_{H} wird als freier Parameter variiert, bis der berechnete Fluss (rote Linie) und die Beobachtungsdaten (schwarze Punkte), übereinstimmen (6.3a).

Die so berechneten Werte werden verwendet, um die Neutrinoflüsse der Quellen zu berechnen. Diese Neutrinoflüsse werden mit den Sensitivitäten aktueller Teleskope (IceCube und ANTARES) und mit der Sensitivität des zukünftigen Teleskops KM3NeT verglichen.

Es zeigt sich, dass die beiden nähesten Objekte Cen A und M 87 vielversprechende Kandidaten sind um, mit KM3NeT detektiert zu werden. Insbesondere Cen A ist hierbei von besonderem Interesse, da der berechnete Neutrinofluss unterhalb der Sensitivität liegt. Alle Sensitivitäten sind für E_ν^{-2}-Flüsse gegeben. Da Cen A einen spektralen Index von $\epsilon_{\mathrm{Cen\ A}} = 2.12$ hat, sind Fehler aufgrund unterschiedlicher Indizes im Vergleich zu den anderen Fehlerquellen wie der Berechnung der Parameter g_e und $\chi(s, B)$ vernachlässigbar.

Für M 87 ist die Situation ähnlich. Obwohl der berechnete Fluss unterhalb der Sensitivität aller Detektoren liegt, wird mit voranschreitender Beobachtungszeit von einigen Jahren der berechnete Fluss unterhalb der Sensitivität von KM3NeT liegen. So kann auch diese Quelle dazu dienen, Einschränkungen auf die hier verwendeten Parameter zu geben.

Die Flüsse der anderen Quellen sind um mehr als eine Größenordnung unterhalb der Sensitivitäten aller Detektoren. Auch zeigen die spektralen Indizes der Quellen im Vergleich zum E_ν^{-2}-Verhalten große Abweichungen, sodass diese Fehlerquelle nicht mehr vernachlässigbar ist.

Zu den wichtigsten Parametern zur Berechnung der Flüsse und Dichten gehören die Radioleuchtkraftfunktionen $F_{\mathrm{radio}}^{\mathrm{FR\text{-}I,FR\text{-}II}}(L, z)$ für FR-I und FR-II sowie $F_{\mathrm{radio}}^{\mathrm{Balazars}}(L, z)$ für Blazare. In dieser Arbeit werden RLF für FR-I und FR-II sowohl verwendet, die im Jahre 2001 bzw. im Jahr 1990 aufgestellt wurden. Da die Rechnungen in dieser Arbeit allgemein gehalten wurden, können neue und verbesserte Messungen der Radioobjekte zu verbesserten Funktionen und dementsprechend zu genaueren Flussvorhersagen führen.

Weiterhin spielen die RLFs eine wichtige Rolle für die Berechnung der CR-Normierung A_{p} und für die Berechnung von g_e. Auch hier können aktuellere RLFs genauere Ergebnisse liefern.

Zur Berechnung von $\chi(s, B)$ wurde ein einfaches Potenzgesetz für das Elektronenspektrum angenommen. Dies kann damit erklärt werden, dass die Berechnungen nur für einfache Potenzgesetze analytisch lösbar sind. In einem weiteren Schritt können somit komplexere Funktionen verwendet werden, um $\chi(s, B)$ numerisch zu berechnen, und so verbesserte Ergebnisse zu liefern.

In Kapitel 6 wurden sieben nahe FR-I-Galaxien berücksichtigt. Eine Erhöhung der Anzahl führt

zu einer besseren Statistik und damit zu genaueren Aussagen. Weiterhin können die Ergebnisse aus Kapitel 5 überprüft werden, da davon auszugehen ist, dass alle FR-I-Punktquellen Säulendichten haben, die im Bereich $10^{23} - 10^{25}\,\mathrm{cm}^{-2}$ liegen.
Das neue Neutrinoteleskop KM3NeT wird in Zukunft von besonderer Bedeuutung sein. Unter der Annahme inelastischer Proton-Proton-Wechselwirkung als Produktionsmechanismus der beobachteten Neutrinofüsse kann KM3NeT verwendet werden, um die zwei nahesten FR-I Galaxien Cen A und M 87 zu beobachten. Hierbei kann KM3NeT helfen, Einschränkungen für die beiden wichtigen Parameter g_e und $\chi(s, B)$ zu geben, deren theoretische Berechnung komplex ist.

Appendix A

Diffuse neutrino fluxes for FR galaxies, based on semi analytical calculation

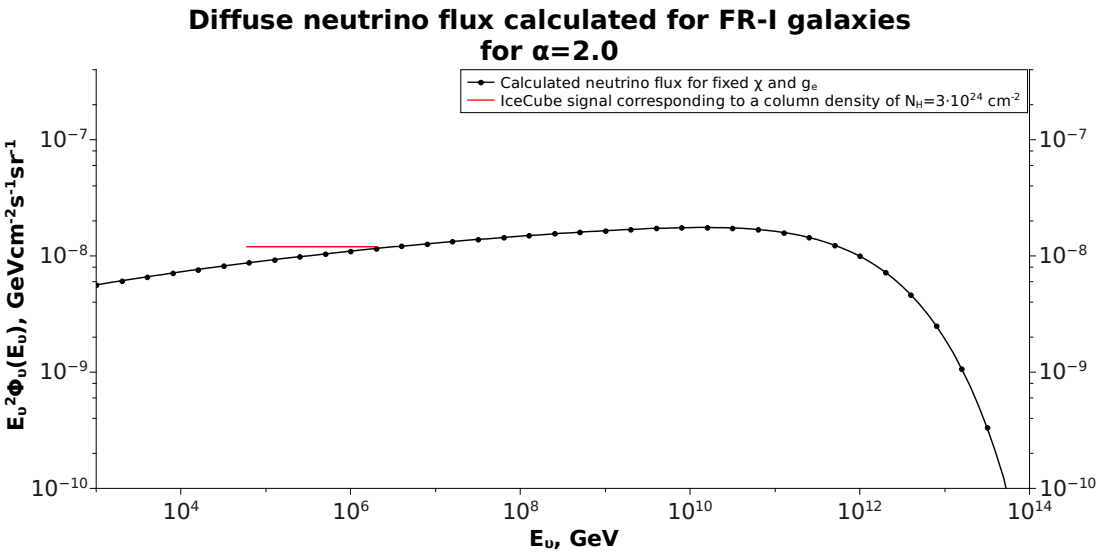

(A) diffuse neutrino flux for FR-I galaxies for $\alpha = 2.0$, with fixed $\chi(s)$ and fixed g_e.

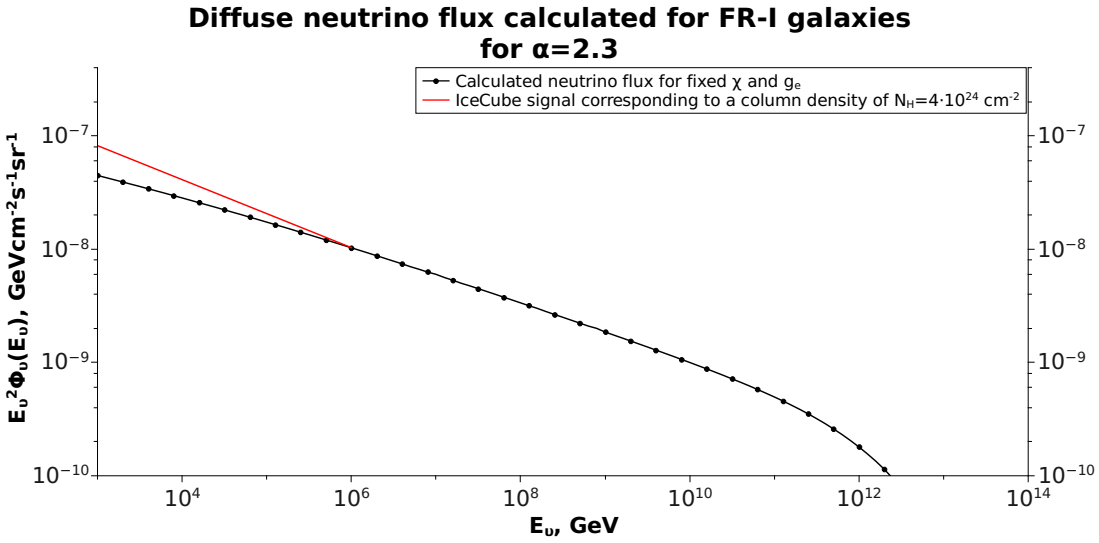

(B) diffuse neutrino flux for FR-I galaxies for $\alpha = 2.3$, with fixed $\chi(s)$ and fixed g_e.

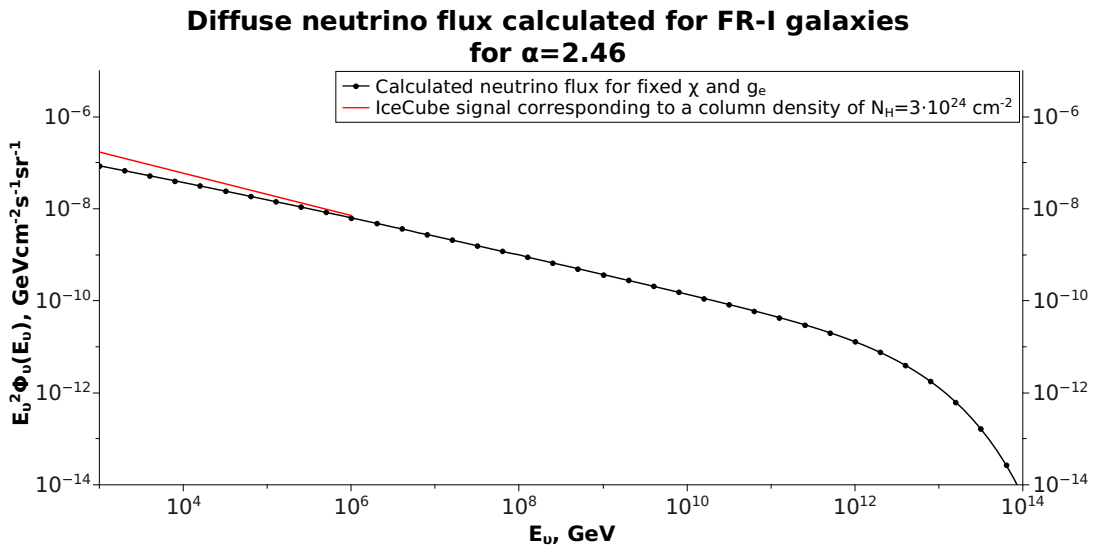

(C) diffuse neutrino flux for FR-I galaxies for $\alpha = 2.46$, with fixed $\chi(s)$ and fixed g_e.

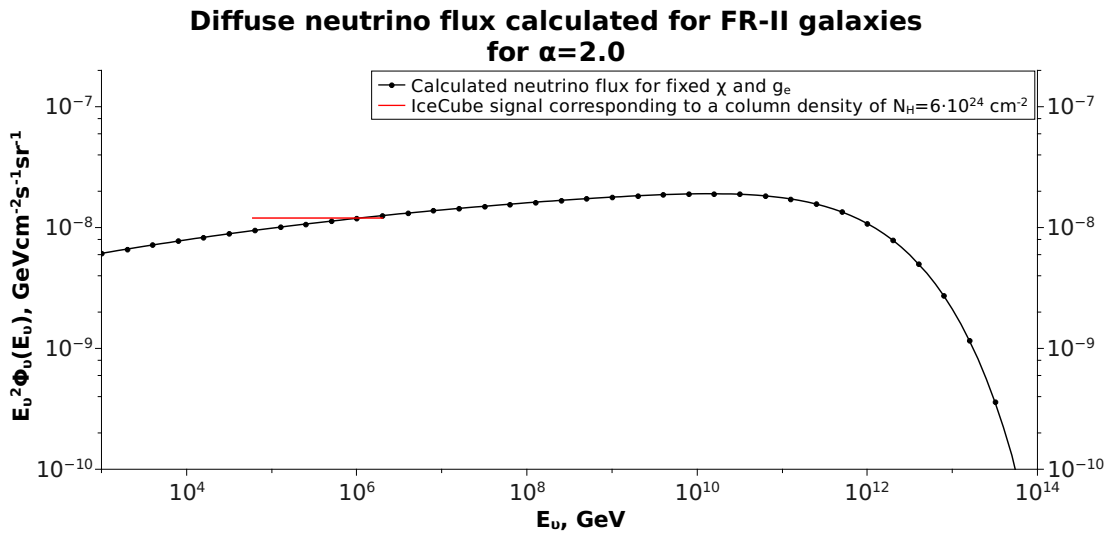

(D) diffuse neutrino flux for FR-II galaxies for $\alpha = 2.0$, with fixed $\chi(s)$ and fixed g_e.

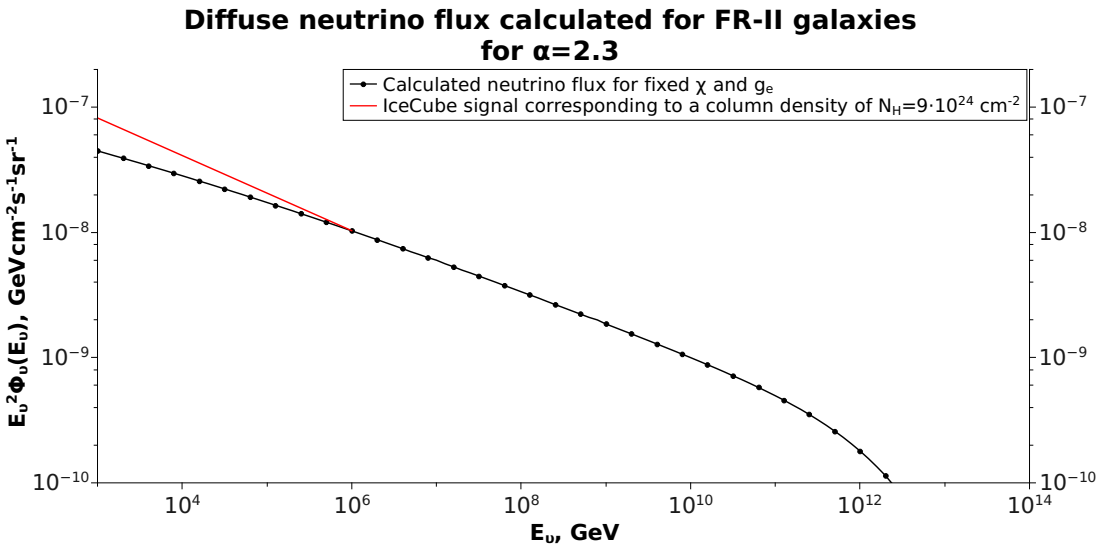

(E) diffuse neutrino flux for FR-II galaxies for $\alpha = 2.3$, with fixed $\chi(s)$ and fixed g_e.

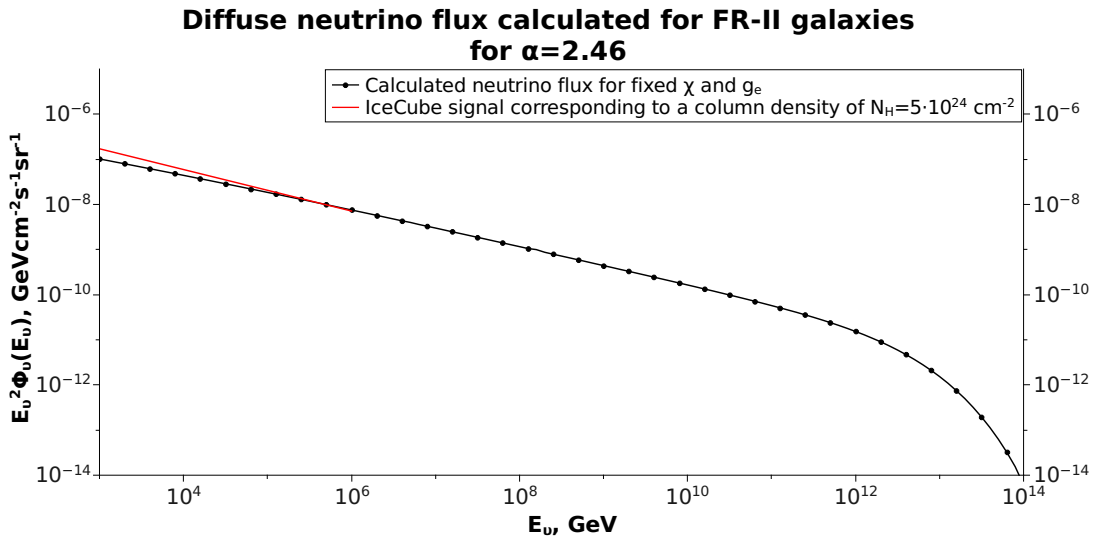

(F) diffuse neutrino flux for FR-II galaxies for $\alpha = 2.46$, with fixed $\chi(s)$ and fixed g_e.

FIGURE A.1: Neutrino fluxes based on semi analytical method for FR galaxies. The red line gives the IceCube signal from [28].

Publications in the context of this thesis

[1] L. Merten, J. Becker Tjus & I. Saba
Estimate of the proton-to-electron ratio at cosmic ray interaction sites and consequences for source modeling
to be submitted to Astrophysics, 2015

[2] J. Becker T. et al.
High-energy neutrinos from radio galxies
Physical Review D, Volume 89, 06/2014

[3] I. Saba & J. Becker Tjus
Calculating column densities for FR-I and FR-II galaxies
Proceedings of the 49th Recontres de Moriond, 2014

[4] I. Saba, J. Becker Tjus & F. Halzen
Limits on the source properties of FR-I galaxies from high-energy neutrino and gamma observations
Astroparticle Physics, Volume 48, 08/2013

[5] I. Saba, J. Becker Tjus & F. Halzen
Neutrinos from Astrophysical Sources
Acta Physica Polonica B Proceedings Supplement, Volume 6, 2012

Bibliography

[1] Todor Stanev
High Energy Cosmic Rays
Springer Verlag, 2004

[2] M. Kachelrieß
Lecture Notes on High Energy Cosmic Rays
arXiv:0801.4376, 01/2008

[3] J. K. Becker
High-energy neutrinos in the context of multimessenger astrophysics
Physics Reports, Volume 458, pp. 173-246, 03/2008

[4] D. O. Chernyshv et al.
Fermi bubbles as a source of cosmic rays above 10^{15} eV
Nuclear Physics B, Volume 256, pp. 179-185, 11/2014

[5] M. Amenomori et al. (The Tibet Collaboration)
Cosmic-ray energy spectrum around the knee obtained by the Tibet experiment and future prospects
Advances in Space Research, Volume 47, pp. 629-639, 02/2011

[6] P. Bhattacharjee & G. Sigl
Origin and propagation of extremely high energy cosmic rays
Physics Reports, Volume 327, pp. 109-247, 03/2000

[7] M. Nagano & A. A. Watson
Observations and implications of the ultrahigh-energy cosmic rays
Reviews of Modern Physics, Volume 72, 07/2000

[8] J. B. et al.
Cosmic rays from the knee to the highest energies
Progress in Particle and Nuclear Physics, Volume 63, pp. 293-338, 10/2009

[9] A. M. Hillas
The Origin of Ultra-High-Energy Cosmic Rays.
Annual Reviews, Massachusetts, 1984, pp. 425-444

[10] A. Meli, J. K. Becker & J. J. Quenby
On the origin of ultra high energy cosmic rays: subluminal and superluminal relativistic shocks
Astronomy and Astrophysics, Volume 492, pp. 323-336, 12/2008

[11] K. V. Ptitsyna & S. V. Troitsky
Physical conditions in potential accelerators of ultra-high-energy cosmic rays: updated Hillas plot and radiation-loss constraints
Physics Uspekhi, Volume 53, pp. 691-701, 10/2010

[12] K. Kotera & A. V. Olinto
The Astrophysics of Ultrahigh Energy Cosmic Rays
arXiv:1101.4256, 01/2011

[13] P. Abreu et al. (The Auger Collaboration)
Measurement of the energy spectrum of cosmic rays at the highest energies using data from Pierre Auger Observatory
UHECR 2012 - International Symposium on Future Directions in UHECR Physics, CERN, Geneva, Volume 53, 06/2013

[14] F. Halzen
Cosmic Neutrinos and the Energy Budget of Galactic and Extragalactic Cosmic Rays
Energy Budget in the high energy regime. Proceedings of the International Workshop, Kashiwa (Japan), 03/2007

[15] T. Piran & R. Jimenez
Possible Role of Gamma Ray Bursts on Life Extinction in the Universe
Physical Review Letters, Volume 113, 12/2014

[16] T. Piran
Gamma-Ray Bursts and the Fireball Model
arXiv:astro-ph/9810256, 10/1998

[17] C. B. Finley
Anisotropy of Arrival Directions of Ultrahigh Energy Cosmic Rays
Doctoral thesis, Columbia University 2006

[18] W. Wagner
Design and Realisation of a new AMANDA Data Acquisition System with Transient Waveform Recorders
PhD thesis, 2004

[19] F. Halzen & S. R. Klein
IceCube: An Instrument for Neutrino Astronomy
arXiv:1007.1247, 10/2010

[20] J. Becker
Calculations of the AGN Neutrino Flux and of Event Rates for Large Volume Neutrino Telescopes
Diploma thesis, 2004

[21] S. Mangano, on behalf of the ANTARES Collaboration
ANTARES Deep Sea Neutrino Telescope Results
arXiv:1310.8451, 10/2013

[22] A. Margiotta, on behalf of the ANTARES Collaboration
The ANTARES neutrino telescope
ISVHECRI 2012 - XVII International Symposium on Very High Energy Cosmic Ray Interactions, Berlin, Germany, 06/2013

[23] F. Aharonian et al. (The KM3NeT Collaboration)
Technical Design Report for a Deep-Sea Research Infrastructure in the Mediterranean Sea Incorporating a Very Large Volume Neutrino Telescope
http://www.km3net.org/KM3NeT-TDR, 2015

[24] M. G. Aartsen et al. (The IceCube Collaboration)
Evidence for High-Energy Extraterrestrial Neutrinos at the IceCube Detector
Science, Volume 342, 11/2013

[25] M. G. Aartsen et al. (The IceCube Collaboration)
IceCube-Gen2: A Vision for the Future of Neutrino Astronomy in Antarctica
arXiv:1412.5106v2, 12/2014

[26] D. B. Fox, K. Kashiyama & P. Mészarós
Sub-PeV Neutrinos from TeV Unidentified Sources in the Galaxy
The Astrophysical Journal, Volume 774, 09/2013

[27] M. Mandelartz & J. B. Tjus
Prediction of the diffuse neutrino flux from cosmic ray interactions near supernova remnants
Astroparticle Physics, Volume 65, pp. 80-100, 05/2015

[28] M. G. Aartsen et al. (The IceCube Collaboration)
Atmospheric and astrophysical neutrinos above 1 TeV interacting in IceCube
Physical Review D, Volume 91, 01/2015

[29] P. Schneider
Extragalaktische Astronomie und Kosmologie
Springer Verlag, Corrected 8th Edition, 2008

[30] Centre for Astrophysics and Planetary Science
http://astro.kent.ac.uk/, 04/2015

[31] C. M. Urry, L. Maraschi & E. S. Phinney
The GUTs of AGN
Comments Astrophysics, Volume 15, pp. 111-117, 03/1991

[32] N. I. Shakura & R. A. Sunyaev
Black holes in binary systems. Observational appearance.
Astronomy and Astrophysics, Volume 24, pp. 337-355, 01/1973

[33] M. Böttcher, D. E. Harris & H. Krawczynski
Relativistic Jets from Active Galactic Nuclei
WILEY-VCH Verlag GmbH & Co. KGaA, 2012

[34] T. J. L. Courvoisir
High Energy Astrophysics
Springer Verlag, 2013

[35] U.S. Particle Accelerator School
Synchrotron radiation-I
https://uspas.fnal.gov/, 04/2015

[36] Institute for Astronomy, University of Hawaii
The Interstellar Medium
http://www.ifa.hawaii.edu/~jpw/classes/ast622.spring2008/, 04/2015

[37] A. Achterberg et al.
On the selection of AGN neutrino source candidates for a source stacking analysis with neutrino telescopes
Astroparticle Physics, Volume 26, pp. 282-300, 11/2006

[38] G. J. Hill & S. J. Lilly
A change in the cluster environments of radio galaxies with cosmic epoch
Astrophysical Journal, Volume 367, pp. 1-18, 01/1991

[39] M. J. Ledlow & F. N. Owen
20 CM VLA Survey of Abell Clusters of Galaxies. VI. Radio/Optical Luminosity Functions
Astronomical Journal, Volume 112, pp. 9-, 07/1996

[40] C. G. Kotanyi & R. D. Ekers
Radio galaxies with dust lanes
Astronomy and Astrophysics, Volume 73, 03/1979

[41] P. G. van Dokkum & M. Franx
Dust in the Cores of Early-Type Galaxies
Astronomical Journal, Volume 110, pp. 2027-, 11/1995

[42] S. de Koff et al.
The Dust-Radio Connection in 3CR Radio Galaxies
The Astrophysical Journal Supplement Series, Volume 129, pp. 33-59, 07/2000

[43] H. R. de Ruiter et al.
HST images of B2 radio galaxies: A link between circum-nuclear dust and radio properties?
Astronomy and Astrophysics, Volume 396, pp. 857-866, 12/2012

[44] B. M. Peterson
An Introduction to Active Galactic Nuclei
Cambridge University Press, 1997

[45] A. K. Kembhavi & J. V. Narlikar
Quasars and Active Galactic Nuclei
Cambridge University Press, 1999

[46] R. C. Hartmann et al.
Multiepoch Multiwavelength Spectra and Models for Blazar 3C 279
The Astrophysical Journal, Volume 553, Issue 2, pp. 683-694, 06/2001

[47] C. J. Willlot et al.
The radio luminosity function from the low-frequency 3CRR, 6CE and 7CRS complete samples
Monthly Notices of the Royal Astronomical Society, Volume 322, pp. 536-552, 04/2001

[48] J. S. Dunlop & J. A. Peacock
The Redshift Cut-Off in the Luminosity Function of Radio Galaxies and Quasars
Monthly Notices of the Royal Astronomical Society, Volume 247, pp. 19-, 11/1990

[49] W. L. Freedman et al.
Carnegie Hubble Program: A Mid-infrared Calibration of the Hubble Constant
The Astrophysical Journal, Volume 758, 10/2012

[50] D. W. Hogg
Distance measures in cosmology
http://arxiv.org/abs/astro-ph/9905116, 04/2015

[51] V. Beckmann, C. Shrader
The AGN phenomenon: open issues
http://arxiv.org/abs/1302.1397, 04/2015

[52] R. Schlickeiser
Cosmic Ray Astrophysics
Springer Verlag, Corrected Second Edition, 2003

[53] S. R. Kelner, F. A. Aharonian & V. V. Bugayov
Energy spectra of gamma rays, electrons, and neutrinos produced at proton-proton interactions in the very high energy regime
Physical Review D, Volume 74, 08/2006

[54] M. S. Longair
High Energy Astrophysics
Cambridge University Press, 1981 The Astrophysical Journal, Volume 553, Issue 2, pp. 683-694, 06/2001

[55] C. D. Dermer & R. Schlickeiser
Proton and electron acceleration through magnetic turbulence in relativistic outflows
Astronomy and Astrophysics, Volume 360, pp. 789-794, 08/2000

[56] J. Becker Tjus et al.
High-energy neutrinos from radio galaxies
Physical Review D, Volume 89, 06/2014

[57] C. Tschernin et al.
An exploration of hadronic interactions in blazars using IceCube
Astronomy & Astrophysics, Volume 555, 07/2013

[58] R. Schlickeiser & K. Mannheim
Interactions of cosmic ray nuclei
Astronomy and Astrophysics, Volume 286, pp. 983-996, 06/1994

[59] L. Merten
Analyse des $p-e^-$ Leuchtkraftverhältnisses der kosmischen Strahlung bei unterschiedlichen Spektralenindizes
Bachelor thesis, 2013

[60] O. E. Kaleshev, A. Kusenko & W. Essey
PeV Neutrinos from Intergalactic Interactions of Cosmic Rays Emitted by Active Galactic Nuclei
Physical Review Letters, Volume 111, 07/2013

[61] I. Saba, J. Becker Tjus & F. Halzen
Limits on the source properties of FR-I galaxies from high-energy neutrino and gamma observations
Astroparticle Physics, Volume 48, pp. 30-36, 08/2013

[62] I. Saba
Deep inelastic scattering of cosmic rays in active galactic nuclei
Master thesis, 2002

[63] S. Chang, Y. Gao & M. Spannowsky
Enhanced gamma ray signals in cosmic proton-wimp collisions due to hadronization
Journal of Cosmology and Astroparticle Physics, Issue 11, 11/2012

[64] G. Ghisellini, F. Tavecchio & G. Ghirlanda
Jet and accretion power in the most powerful Fermi blazars
Monthly Notices of the Royal Astronomical Society, Volume 399, pp. 2041-2054, 11/2009

[65] F. Tavecchio & G. Ghisellini
The spectrum of the broad-line region and the high-energy emission of powerful blazars
Monthly Notices of the Royal Astronomical Society, Volume 386, pp. 945-952

[66] A. Mücke et al.
BL Lac objects in the synchrotron proton blazar model
Astroparticle Physics, Volume 18, pp. 593-613

[67] R. Vainio, M. Pohl & R. Schlickeiser
Conversion of bulk kinetic energy into radiation in AGNs and GRBs: Particle transport effects
Astronomy and Astrophysics, Volume414, pp. 463-474, 02/2014

[68] A. A. Abdo et al. (The Fermi *LAT* collaboration)
Fermi Large Area Telescope observations of misaligned Active Galactic Nuclei
The Astrophysical Journal, Volume 720, pp. 912-922, 09/2010

[69] E. Charles
The First Fermi Large Area Telescope Catalog of Gamma-ray Pulsars
The Fermi *LAT* Collaboration
The Astrophysical Journal Supplement, Volume 187, pp. 460-494, 04/2010

[70] G. Migliori et al.
Implications for the structure of the relativistic jet from multiwavelength observations of NGC 6251
Astronomy & Astrophysics, Volume 533, 09/2011

[71] P. N. Willkinson et al.
3C380 - A powerful radio source seen end-on?
Monthly Notices of the Royal Astronomical Society, Volume 248, pp. 86-90, 01/1991

[72] G. Brunetti et al.
Chandra discovery of extended non-thermal emission in 3C 207 and the spectrum of the relativistic electrons
Astronomy and Astrophysics, Volume 381, pp.795-809, 01/2002

[73] J. P. Halpern
X-ray spectrum and variability of 3C 120
Astrophysical Journal, Part 1, Volume 290, pp. 130-135, 03/1985

[74] L. Ballo et al.
The high-energy view of the broad-line radio galaxy 3C 111
Monthly Notices of the Royal Astronomical Society, Volume 418, pp. 2367-2380, 12/2011

[75] F. P. Israel
Centaurus A - NGC 5128
The Astronomy and Astrophysics Review, Volume 8, pp. 237-278, 01/1998

[76] N. Sahakyan et al.
Evidence for a Second Component in the High-energy Core Emission from Centaurus A?
The Astrophysical Journal Letters, Volume 770, 2013

[77] A. A. Abdo et al. (Fermi LAT collaboration)
Fermi Large Area Telescope Gamma-Ray Detection of the Radio Galaxy M87
The Astrophysical Journal, Volume 707, pp. 55-60, 12/2009

[78] M. Beilicke et al.
Discovery of fast variability of the TeV gamma-ray flux from the radio galaxy M 87 with H.E.S.S.
Proceedings of the 30th International Cosmic Ray Conference, 2007, Mérida, Yucatán, Mexico, Volume 3, pp. 937-940, 2007

[79] K. Berger
MAGIC observations of the giant radio galaxy M87 in a low emission state between 2005 and 2007
Proceedings of the 32nd International Cosmic Ray Conference 2011 in Beijing, 2011

[80] M. Beilicke et al. (The VERITAS Collaboration)
VERITAS observations of M87 in 2011/2012
5th International Meeting on High Energy Gamma-Ray Astronomy. AIP Conference Proceedings, Volume 1505, pp. 586-589, 12/2012

[81] D. Giannios et al.
Fast TeV variability from misaligned minijets in the jet of M87
Monthly Notices of the Royal Astronomical Society, Volume 402, pp. 1649-1656, 03/2010

[82] M. V. Barkov et al.
Interpretation of the Flares of M87 at TeV Energies in the Cloud-Jet Interaction Scenario
The Astrophysical Journal, Volume 755, 08/2012

[83] A. Levinson & F. Rieger
Variable TeV Emission as a Manifestation of Jet Formation in M87?
The Astrophysical Journal, Volume 730, 04/2011

[84] M. G. Aartsen et al. (The IceCube Collaboration)
Searches for Extended and Point-like Neutrino Sources with Four Years of IceCube Data
arXiv:1406.6757, 06/2014

[85] J. J. Hernandez-Rey
Recent results of the ANTARES Neutrino Telescope
arXiv:1410.7720, 10/2014